

University of Alberta

STM Downmixing Readout of Nanomechanical Motion

by

Meng Kan

A thesis submitted to the Faculty of Graduate Studies and Research

in partial fulfillment of the requirements for the degree of

Master of Science

Physics

©Meng Kan

Fall 2010

Edmonton, Alberta

Permission is hereby granted to the University of Alberta Libraries to reproduce single copies of this thesis and to lend or sell such copies for private, scholarly or scientific research purposes only. Where the thesis is converted to, or otherwise made available in digital form, the University of Alberta will advise potential users of the thesis of these terms.

The author reserves all other publication and other rights in association with the copyright in the thesis and, except as herein before provided, neither the thesis nor any substantial portion thereof may be printed or otherwise reproduced in any material form whatsoever without the author's prior written permission.

Examining Committee

Dr. Mark Freeman (supervisor), Department of Physics

Dr. Wayne Hiebert (Co-supervisor), National Institute for Nanotechnology

Dr. Al Meldrum, Department of Physics

Dr. Mark McDermott, Department of Chemistry

Acknowledgment

I would like to express my deepest appreciation to my supervisors Dr. Wayne Hiebert and Professor Mark Freeman who granted me this opportunity and introduce me to the amazing world of NEMS. As mentors, they provided great help, support and enthusiasm which have made a pretty educational journey. Their vast knowledge of numerous science disciplines, coupled with an unmatched enthusiasm for nanoelectromechanical system will always be remembered.

Thanks to David C. Fortin Kar Mun Cheng and Eric Finley who helped me to set up the STM system and make the system work. Thanks to Vincent Sauer whose helped me to solve the fabrication issue. And thanks to all members in Mark's group, I very much enjoyed learning and discussing with them.

Also thank to David Munoz-Paniagua and Jason Pitters who discuss the issues of the STM system and give useful ideas on the application of STM.

Last but not least, I would like to thank my family for their support and encouragement, and am especially grateful to my wife, for always being with me through the ups and downs. My progress would never have been possible without their dedication.

The work was supported by the National Research Council of Canada, iCORE and University of Alberta.

STM Downmixed Readout of Nanomechanical Motion

MENG KAN

University of Alberta, Department of Physics, 2010

Supervisors: Dr. Wayne Hiebert, National Institute for Nanotechnology

Professor Mark Freeman, Department of Physics, University of Alberta

ABSTRACT

For all the nanotechnology applications of NEMS devices, a key challenge is figuring out a fast, low-noise technique for translating small mechanical motion into detectable electronic signals to measure. The scanning tunneling microscope (STM) based on electron tunneling between a sharp tip and conducting sample is a promising method to measure the small displacements. For electron tunneling, the tunneling current is sensitive to the change in distance between the sharp tip and conducting sample, usually less than 1nm. However a limitation in scanning tunneling microscopy is the low temporal resolution because stray capacitance of readout circuitry between the amplifier and tunneling junction will cutoff the high frequency, usually at a few 10's of kHz. This limitation is far less than the fundamental limit of STM, I_T/e , which is the electron tunneling rate. In a typical STM tunneling current 1nA, the electron tunnels at a rate of 5GHz. In this thesis, an STM-downmixing readout technique, which directly mixes high frequency signals in tunneling junction, is introduced and explored in order to overcome the detection bandwidth limitation of STM. With this technology we measure the high frequency vibrational modes (~ 1 MHz) of MEMS doubly-clamped beams, well above the RC rolloff of our circuitry, and explore the effects of driving force, measuring position and STM parameters, such as DC tunneling current and DC bias voltage on the sensitivity of STM downmixing readout technique and the resonance frequencies of MEMS device. We anticipate that, with this technique, the GHz, - and even higher frequency -, information can be detected.

Contents

Chapter 1 Introduction	1
1.1 Overview of nanoelectromechanical systems	1
1.2 Mathematical description of resonator motion	3
1.3 Fabrication of nanoelectromechanical devices	7
1.4 Displacement detection of NEMS	11
1.5 Motivation of this thesis	18
REFERENCES	20
Chapter 2 Experimental Instrument	24
2.1. Scanning Tunneling Microscopy (STM) system	24
2.2. The adaptations of the STM system	27
2.2.1 Modification of mechanical part of STM	27
2.2.2 The accessories of STM System	31
2.3. The operation of STM	34
REFERENCES	37
Chapter 3 Electron Tunneling Transducer Using Signal Downmixing Readout	38
3.1 The introduction of electron tunneling transducer	38
3.2 Device actuation	42
3.3 Mathematical description of STM Junction downmixing	45
3.4 Configurations of tunneling junction frequency downmixing	47
REFERENCES	52
Chapter 4 Downmixing Data with STM as Electron Tunneling Transducer	
4.1 The MEMS sample setup	53

4.2 The proof of STM tunneling junction downmixing	55
4.3 The result of STM downmixing readout	58
4.4 The Effects of measurement parameters on STM downmixing method	73
4.4.1 Forces between STM tip and MEMS device	73
4.4.2 The effect of changing DC tunneling current	76
4.4.3 The effect of changing DC bias voltage	80
4.4.4 The effect of changing piezo disk actuating power	84
4.4.5 The effect of measuring positions	90
4.5 The displacement sensitivity of the STM downmixing readout method	95
4.6 Conclusion	97
REFERENCES	99
Chapter 5 Future directions	101
5.1 How to measure the nanoscale device	101
5.2 Phase Locked Loop (PLL) with STM downmixing readout	102
5.3 Integrate the whole system into a chip	103
REFERENCES	105
APPENDIX A Labview Program Operation	106
APPENDIX B STM Downmixing Analysis with Normal Mixer	108
APPENDIX C: The Beam Higher Mode Information	111
APPENDIX D: Detail Information about the Different Positions	117
APPENDIX E: Measurement of Barrier Height	123

List of Figures

Figure 1.1	Doubly-clamped beam with length l , width w and thickness h suspended a distance d above the Si substrate.....	3
Figure 1.2	Schematic drawing illustrating contact exposures.....	9
Figure 1.3	The process steps to fabricate suspended doubly clamped beam with photolithography. (a) SOI wafer. (b) The wafer is coated with metal (Au and Cr). (c) The wafer is coated with metal and photoresist. (d) Metal layer is patterned with photolithography and etched. (e) Alloyed layer and Silicon layer are etched away. (f) Silicon dioxide layer is etched through.....	10
Figure 1.4	Topographies of Au film on the sample surface. Images show the surface characterization of the Au film for different areas. The measurement conditions are: DC bias voltage 0.5 V, DC setpoint 0.3 nA, scanning speed 0.5 $\mu\text{m/s}$ and time constant 51.34 ms.....	11
Figure 1.5	Optical displacement detection. (a) The schematic diagram of Fabry-Perot interferometry. (b) The schematic diagram of Michelson interferometry.....	12
Figure 1.6	Magnetomotive displacement detection.....	14
Figure 1.7	Capacitive displacement detection (a) Diagram of capacitive detection for a doubly clamped NEMS beam (b) The circuit of capacitive detection.....	15
Figure 1.8	Electron tunneling transducer for displacement detection.....	17
Figure 2.1	Schematic diagram of a scanning tunneling microscope.....	25
Figure 2.2	The schematic of two operation mode in STM (a) Constant-current mode and (b) Constant –height mode.....	26
Figure 2.3	The schematic of STM mechanical part and STM sample approaching system (Inset) (IBM STM operation manual).....	28

Figure 2.4	The schematic of new adjustment stop.....	29
Figure 2.5	The image of MEMS device and tip in the mirror	29
Figure 2.6	The scheme of sample holder (a) The older sample holder (b) The Schematic of new sample holder and (c) The new sample holder with Attocube System which can move along X and Y Plane (Image a and b modify from IBM STM operation manual).....	30
Figure 2.7	STM Pt-Ir Tip Image. (a) Two tip apexes close each other (b) Two tip apexes with a big gap (preferred) (c) High resolution image for one tip apex of the image (a) (d) High resolution image for one tip apex of the image (b) (preferred).....	32
Figure 2.8	The spectrum of noise in STM system (a) The ion pump noise spectrum (b) Other noise spectrum.....	33
Figure 2.9	The image of STM system on vibration isolation table.....	34
Figure 2.10	Basic element of a Scanning Tunneling Microscopy.....	35
Figure 3.1	Scheme for the detection of displacement through an electron tunneling transducer. The static separation between the NEMS device and the tip is x and the displacement of the NEMS device is $(x-d)$	39
Figure 3.2	Motion of Piezoelectric Material when it is applied bias voltage. (a) Piezoelectric material is not applied bias voltage. (b) Piezoelectric material is applied bias voltage	43
Figure 3.3	Piezoelectric Material Frequency Responses. In usable region, the relationship between the applied voltage and the force is linear. (Imitating graph from Wikimedia Commons).....	44
Figure 3.4	The scheme of downmixing which integrates electron tunneling transducer and piezoelectric actuator.....	46
Figure 3.5	Information of Tunneling Current in Frequency Domain.....	47

Figure 3.6	STM frequency downmixing readout scheme.....	49
Figure 4.1	Schematic of the doubly-clamped beam.....	53
Figure 4.2	The sample of STM downmixing readout. Here MEMS device and the piezo disc which is used to actuating MEMS device are mounted on the PCB together.....	54
Figure 4.3	The downmixing tunneling current information from a spectrum analyzer. (a) Drive frequency far from sample resonance frequency. (b) Drive frequency go close to the sample resonance frequency. (c) Drive frequency closest to the mechanical resonance frequency. (d) Drive frequency go away from the sample resonance frequency.....	56
Figure 4.4	The downmixed tunneling current sideband information. Inset graph (a) Electrical and mechanical noise current FFT (b) Reference frequency with sideband current FFT.....	57
Figure 4.5	COMSOL simulation of beam mode shapes (Color indicates displacement from equilibrium position with minimum displacement at the ends of the beam).....	59
Figure 4.6	Schematic optical interferometry technique.....	60
Figure 4.7	Optical interferometry measured response amplitude square (black line) and phase (cyan line) as a function of drive frequency at actuating power -5dBm. The red line shows the Lorentz fitting for the amplitude of MEMS device. (a) and (e) were measured with spectrum analyzer at actuating power -5 dBm. (b) (c) (d) and (f) were measure with network analyzer at actuating power 0 dBm.....	61
Figure 4.8	The readout Result of STM downmixing technique (a) Downmixed tunneling response prediction with simulation (b) The measured result with phase change from 0 to 180 degree (c) The measured result with phase change from -90 degree to 90 degree. The results	

of STM downmixing technique are measured at the following conditions: DC bias voltage 0.5 V, AC bias voltage is 0.1 V_{rms}, DC tunneling current 0.2 nA and the actuating power of piezo disk is -11 dBm.....65

Figure 4.9 The results of STM downmixed Readout technique at the following conditions: DC tunneling current is 0.2 nA, DC bias voltage is 0.5 V, AC bias voltage is 0.1 V_{rms} and piezo disk actuating power is -11dBm (a) Fundamental flexural vibration mode measured (b) The first torsion vibration mode (c) The third flexural vibration mode (d) The second torsion vibration mode and (e) The forth flexural vibration mode. The first flexural mode is measured close to the edge of MEMS beam, the third flexural mode is measured at three-fifths position and other modes are measured close the center of the MEMS beam.....69

Figure 4.10 The curve shows the downmixed tunneling current of Figure 4.9 (e) in complex plane. The real part and image part of downmixed tunneling current come from the x and the y output of lock-in amplifier, separately.72

Figure 4.11 Information of van der Waals force, Casimir force and Electrostatic force for different distance between the tip and the sample at DC bias voltage 0.5 V and the tip diameter 10 nm.....75

Figure 4.12 The scheme shows force distribution of scanning tunneling microscope with the distance from the tip to the surface of the sample. For a scanning tunneling microscope system, there are two force regimes - repulsive regime and attractive regime – which have different effect on the motion of MEMS devices.....76

Figure 4.13 The influence of DC tunneling current. The results are measured at the four-tenths of the doubly-clamped beam position for the fourth flexural vibration mode and the measurement conditions are: DC

bias voltage 0.5V, AC bias voltage 0.1 V_{rms} and piezo disk actuating power -11dBm. (a) The results and fitting of downmixed tunneling current for different DC tunneling current (b) The effect on downmixed tunneling current peak by DC tunneling current (c) The effect on resonance frequencies by DC tunneling current.....78

Figure 4.14 The effect of DC Bias Voltage in STM Downmixing Technique. The results are measured at the four-tenths of the doubly-clamped beam and the measurement conditions are: DC tunneling current 0.2 nA, AC bias voltage 0.1 V_{rms} and piezo disk actuating power -11dBm. (a) The results and fitting of downmixed tunneling current for different DC bias voltage (b) The effect on downmixed tunneling peaks change by DC bias voltage (c) The effect on resonance frequencies by DC bias voltage.....83

Figure 4.15 The piezo disk frequency response with MEMS device at the top. Inset graph (a) shows the piezo disk frequency response from 400 KHz to 500 KHz (b) shows the piezo disk frequency response from 500 KHz to 600 KHz and (c) shows the piezo disk frequency response from 900 KHz to 1 MHz85

Figure 4.16 The impact of actuating power for STM downmixing technique. These results are measured at the four-tenths of the doubly-clamped beam and the measurement conditions are: DC tunneling current 0.2 nA, DC bias voltage 0.5 V and AC bias voltage 0.1 V_{rms} . (a) The results and fitting of downmixed tunneling current for different actuating power (b) The effect on downmixed tunneling current peak change by piezo disk actuating voltage (c) The effect on the resonance frequencies by the piezo disk actuating voltage.....87

- Figure 4.17 The effect of actuating power with optical interferometry method. (a) The results and fitting curve of response with frequency (b) Resonance frequency are modified by actuating power.....89
- Figure 4.18 Effects of the measured point along MEMS beam length direction. The measurement conditions are: DC tunneling current 0.2 nA, DC bias voltage 0.5 V, AC bias voltage 0.1 V_{rms} and piezo disk actuating power -11dBm. (a) The results and fitting curves of different measuring positions (b) The vibration amplitude of each point. The points on the red line have similar vibration amplitude and the points on the blue line also have similar vibration amplitude. (c) Resonance frequencies of each points which response the change of the vibration amplitude of each point. The points on the red line have similar resonance frequencies and the points on the blue line have similar resonance frequencies.....92
- Figure 4.19 The information of the position 1, 4, 6, 9 in complex plane. X is the real part of downmixed tunneling current and Y is the image part of downmixed tunneling current.....93
- Figure 4.20 Effect of resonance frequency for different measured point along the length direction of the MEMS beam (small resonance frequency shift). The measurement conditions are: DC tunneling current 0.2 nA, DC bias voltage 0.5 V, AC bias voltage 0.1 V_{rms} and piezo disk actuating power -11dBm.....94
- Figure 4.21 Effects of the measured point along MEMS along the width direction of the MEMS beam. The measurement conditions are: DC tunneling current 0.2 nA and DC bias voltage 0.5 V, AC bias voltage 0.1 V_{rms} and the piezo disk actuating power -11 dBm. (a) The information at the center of the beam and the letters in brackets responding the position shown in graph (c). (b) The information at 1415 of 1700 of beam and the letters in the bracket responding the position shown in graph (c). (c) The scheme of the first torsion mode and measurement

	points across wide direction. (d) Show the resonance frequency across the wide direction for two position along the long direction.....	95
Figure 4.22	The Current noise of STM downmixing method for different point when the actuating power for piezo disk is zero. Here the spikes of the graph are some mechanical or electrical noise.....	97
Figure5.1	The Scheme of FESEM and STM. For the FESEM, the distance between the tip and the surface of sample is more than 1 nm and the DC bias voltage is higher than the work function of the sample material. But for the STM system, the distance from the tip to the surface of the sample usually is less than 1 nm (around several angstroms) and the DC bias voltage is lower than the work function of the sample material.....	102
Figure5.2	The Scheme of Phase-locked Loop with STM Downmixing Method. Here RF generator is a signal generator with frequency modulation function, phase shift can shift two signals with 90 degree phase difference and adder can amplifier the two input signals and does not cause the phase shift.....	103
Figure A.1.	STM downmixing readout circuit control panel.....	107
Figure A.2.	STM downmixing readout Labview Program.....	108
FigureB.1	Schematic of STM downmixing with normal mixer.....	109
Figure C.1.	The piezo disk frequency response with MEMS device at the top.....	112
Figure C.2.	The resonance frequencies and phase information for higher mode of a long 500 μm , wide 100 μm and thick 5 μm silicon doubly-clamped beam with Au and Cr metal layer at DC tunneling current 0.2 nA, DC bias voltage 0.5 V, AC bias voltage 0.1 V_{rms} and the piezo disk actuating power -11dBm.....	113

Figure D.1. The detail resonance frequency and phase shift information for different measuring position along length at DC tunneling current 0.2 nA, DC bias voltage 0.5 V, AC bias voltage 0.1 Vrms and piezo disk actuating power -11dBm	118
--	-----

List of Tables

Table 1.1 Numerical solutions for a doubly clamped beam.....	6
Table 4.1 COMSOL Simulation Result for a long 500 μm , wide 100 μm and thick 5 μm Silicon Doubly-clamped Beam with Au and Cr Metal Layers.....	58
Table 4.2 Optical Interferometry Measurement Results for a long 500 μm , wide 100 μm and thick 5 μm Silicon Doubly-clamped Beam with Au and Cr Metal Layers.....	60
Table 4.3 STM Downmixing Measurement Result for a long 500 μm , wide 100 μm and thick 5 μm Silicon Doubly-clamped Beam with Au and Cr Metal Layers.....	68
Table 4.4 The resonance frequency information using different techniques for a 500 μm long, 100 μm wide and 5 μm thick Silicon Doubly-clamped Beam with Au and Cr Metal Layers.....	68
Table C.1 The higher vibration mode information for a long 500 μm , wide 100 μm and thick 5 μm Silicon Doubly-clamped Beam with Au and Cr Metal Layers.....	117
Table D.1 The resonance frequencies and phase information for the different position along the length of a long 500 μm , wide 100 μm and thick 5 μm Silicon Doubly-clamped Beam with Au and Cr Metal Layers.....	123

List of symbols

A	the cross sectional area of doubly-clamped beam
a_n	the vibration amplitude of MEMS beam with the driving force
B	the magnetic field strength
BOE	buffered oxide etch
C_p	the parasitic capacitance between the tip and the I/V preamplifier
d	the distance between the tip and the sample surface
D	the electric charge density displacement of piezo disk
E	Young's modulus of MEMS beam
ξ	a geometric factor of MEMS or NEMS device
F	actuating force
$F(t)$	the harmonic driving force
f_0	fundamental resonance frequency of free MEMS beam
f_r	resonance frequency with external force
F_c	Casimir Force _s
F_{vaW}	van der Waals force
F_{el}	electrostatic force
h	the thickness of the doubly-clamped beam
H	the Hamaker constant
I	the momentum of inertia
i	the tunneling current
$i_{downmixed}$	the downmixed tunneling current
J	the tunneling current density
K	spring constant of the MEMS device

K_c	the capacitance expansion coefficient given by the geometry
K_i	the force gradient between the tip and the surface of MEMS beam
K_n	eigenvector of the MEMS device motion function
κ	the decay constant of electron wave-function within the gap
l	the length of the doubly-clamped beam
m_{eff}	the effective mass of MEMS device
ϕ_n	the n th mode vector of MEMS device motion function
ρ	the mass density of per unit length
PPL	phase lock loop
R	the radius of the STM tip
RF	radio frequency (the range about 300 kHz to 300 GHz)
R_T	the resistance of the tunneling junction
STM	scanning tunneling microscope
$u(x,t)$	the displacement of the doubly-clamped beam along Z direction
UHF	ultrahigh Frequency
VHF	very high frequency
$V_{emf}(t)$	an introduced electromotive force voltage by the magnetic field
V_s	the voltage of RF generator output
V_r	the voltage of Lock-in amplifier reference output
w	the width of the doubly-clamped beam
ω	vibration angular frequency

ω_n the nth mode resonance frequency of the doubly-clamped beam

ω_c the carrier angular frequency of actuating power

1.1. Chapter 1 Introduction

1.1 Overview of nanoelectromechanical systems

Micro or nano-electromechanical systems (MEMS or NEMS) are small integrated systems which incorporate micro- or nano-scale mechanical elements, sensors, actuators, and electronics on a substrate through microfabrication or nanofabrication [1, 2]. They have a host of exciting attributes including ultrahigh frequency operation, ultrasensitivity, ultralow power, high responsivity, and small size scale making them potentially useful in a wide range of applications. They have played and will continue to play a very important role for a fundamental study of mechanical motion in the quantum limit [3] [4] [5]. MEMS and NEMS have been a tool in the research in physics, biology and engineering. Many scientists share a great interest in miniaturization technologies and in studying the behavior of materials and structures in the micro- and nanometer range. The investigation of the small world of matter is crucial to understanding how things work and this knowledge can be used to create novel microstructures and devices, thus offering the necessary tools and components to realize applications of great societal importance.

Micro and Nano-electromechanical systems are a fascinating field. Here one mechanical resonator owns a simple geometry, such as a cantilever (a beam clamped at one end) or a bridge (a beam clamped at both ends), and is fabricated based on the material such as silicon using similar techniques employed for semiconductor chip manufacturing. In the submicron size regime, these mechanical resonators can vibrate at frequencies up to and beyond a gigahertz and preserve very high mechanical responsiveness (small force constant). This powerful combination of attributes translates directly into high force sensitivity, and operability with quite modest control force.

The minuscule mass and high quality factor of MEMS and NEMS show promise for foundationally different forms of mass sensing, where the mass of a small

particle attaching itself to a nanomechanical resonator can be determined from the resulting vibrational frequency-shift of the resonator. For example, extraordinary mass sensitivity levels in the zeptogram ($1\text{zg} = 10^{-21}\text{g}$) range have been exhibited [6]. With the use of suitably-engineered high frequency NEMS, a new paradigm of mass spectrometry is now conceivable in which the detection of individual molecules should be possible at single-Dalton sensitivities (1 Dalton= $1.66 \times 10^{-27}\text{kg}$, 1/12 the mass of a C^{12} atom) [7] [8]. This extreme sensitivity to mass combined with selective binding sites is enabling next-generation detection methods of hazardous chemicals and biological agents [9].

Another application is force microscopy, where a cantilever tip is scanned over a surface and the cantilever displacement measured as the tip interacts with the surface used to build up a force topography map. Of particular interest is the magnetic resonance force microscope (MRFM) which employs a ferromagnetic cantilever tip, enabling the mapping of unpaired electron and nuclear spin densities at and below the surface [10]. Recently, single electron spin detection sensitivities were achieved [11] [12] [13]; the potential applications of being able to determine chemical identity at the single molecular or atom level are numerous. And with the use of smaller, suitably-engineering NEMS MRFM devices, the higher mechanical frequencies might result in faster read-out times at equivalent or better sensitivities.

MEMS and NEMS also have the potential impact on the field of information and communications technology in chip-level signal processing, for instance, MEMS and NEMS could replace filters, antennas, and oscillator clocks in mobile phone [14]. Otherwise, in life science MEMS and NEMS may play an important role through ultrasensitive devices for chip-level bio-sensing and gas detection.

For all the nanotechnology applications of NEMS and MEMS devices, a key challenge is to figure out a fast, low-noise technique for translating small mechanical motion into reasonable electric signals to measure. Solving this problem will one day make it possible to build electric signal processing devices

that are much more compact than their purely electric counterparts. In this thesis we will briefly discuss the resonator motion and motion detection, and then we will focus on the displacement detection method of STM downmixing readout of nanomechanical motion.

1.2 Mathematical Description of Resonator Motion

Various geometric NEMS devices have been fabricated and investigated, such as doubly-clamped beams, paddles, cantilevers and nanowire. In this work, we will focus specifically on doubly-clamped beams whose geometry is given in Fig. 1.1.

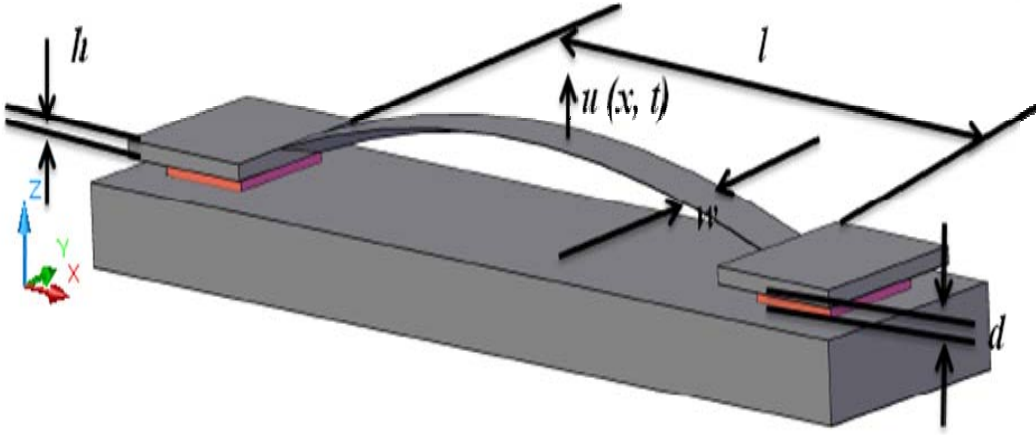


Figure 1.1 Doubly-clamped beam with length l , width w and thickness h suspended a distance d above the Si substrate.

The equation of motion for this device geometry with force $F(x, t)$ can be derived from Euler-Bernoulli beam theory [2] and can be written as:

$$EI \frac{\partial^4 u(x, t)}{\partial x^4} + \rho A \frac{\partial^2 u(x, t)}{\partial t^2} = F(x, t) \quad (1.1)$$

where E is Young's modulus, I is the moment of inertia ($I = hw^3/12$), ρ is the mass density per unit length, and A is the cross sectional area ($A = wh$). The time

varying displacement $u(x, t)$ varies along the length of the resonator and will have a maximum displacement at the midpoint. To estimate the resonant frequencies of this structure, we must consider free vibration and let $F(x, t) = 0$. Eqn. 1.1 can be solved by the separation of variables method where the real displacement $u(x)$ is expressed as a product of space and time, namely

$$u(x, t) = \text{Re}[u(x)e^{i\omega t}] = \hat{u}(x) \cos(\omega t) \quad (1.2)$$

For a natural mode of vibration ($\omega = \omega_n$), we can obtain a modal solution where ϕ_n corresponds to the n th mode vector.

$$u(x, t) = \phi_n(x) \cos(\omega_n t) \quad (1.3)$$

All structures fabricated for this study had cross sections and material properties that did not vary along the length of the beam. Incorporating that the products

EI and ρA are constant; the derivatives of Eqn. 1.3 are substituted into Eqn. 1.1 to provide a homogeneous ordinary differential equation

$$\frac{d^4 \phi_n(x)}{dx^4} - K_n^4 \phi_n(x) = 0 \quad (1.4)$$

$$K_n = \left(\frac{\rho A}{EI}\right)^{1/4} \omega_n^{1/2} \quad (1.5)$$

Here K_n is the wavenumber and is a constant for each mode with resonant frequency ω_n . From Eqn. 1.4, we see that the spatial dependence depends on a fourth order equation and therefore four boundary conditions are required for an exact solution. For a beam clamped at both ends, the displacements $\phi_l(x)$ and slopes $d\phi_l/dx$ must be zero at both ends of the beam (e.g., at $x = 0$ and at $x = l$). The solution to Eqn. 1.4 provides the beam deformation shape for each mode and can be expressed in terms of real functions.

$$\phi_n(x) = C_{1n}(\cos(K_n x) - \cosh(K_n x)) + C_{2n}(\sin(K_n x) - \sinh(K_n x)) \quad (1.6)$$

with eigenvectors K_n meeting the condition:

$$\cos(K_n l) \cosh(K_n l) - 1 = 0 \quad (1.7)$$

where the zeroes of this equation are found numerically to be $K_n l = 0, 4.73004, 7.8532, 10.9956, 14.1372 \dots$. The corresponding resonant frequencies can be found by rearranging Eqn. 1.5

$$\omega_n = \left(\frac{EI}{\rho A}\right)^{1/2} K_n^2 \quad (1.8)$$

The fundamental resonance for a doubly clamped beam can then be expressed as [2]

$$f_0 = 3.56 \sqrt{\frac{EI}{\rho A}} \frac{1}{l^2} \quad (1.9)$$

or alternatively by substituting $I = \frac{hw^3}{12}$ and $A = wh$ as

$$f_0 = 1.028 \sqrt{\frac{E}{\rho}} \frac{h}{l^2} \quad (1.10)$$

And the higher modes are $f_n/f_0 = 2.756, 5.404, \text{ and } 8.933$ for $n = 2, 3, \text{ and } 4$.

The eigenfunction $\phi(x)$ in equation (1.4) are mutually orthogonal, and we normalize them to the beam length, so that

$$\int_0^{\ell} \phi_n(x) \phi_m(x) dx = l^3 \delta_{mn} \quad (1.11)$$

The corresponding coefficient C_{1n} and C_{2n} are listed in Table 1.1[15]. An arbitrary solution $u(x, t)$ which is undriven or driven motion can be written as:

$$u(x, t) = \sum_{n=1}^{\infty} a_n(t) u_n(x) \quad (1.12)$$

where the amplitudes, a_n , are dimensionless.

Table 1.1 Numerical solutions for a doubly clamped beam

	n=1	2	3	4
$K_n l$	4.73004	7.8532	10.9956	14.1372
f_n/f_1	1	2.756	5.404	8.933
C_{1n}/l	-1.0000	-1.0000	-0.9988	-1.0000
C_{2n}/l	0.9825	1.008	0.9988	1.0000

Now let us go back to equation (1.1) and add a harmonic driving force with the expression, $F(t) = F \exp(i\omega_c t)$, where F is the position-independent force per unit length. The force is uniform across the beam cross section and directed along Z , and the carrier frequency ω_c is close to ω_0 . The equation of motion can be written as:

$$EI \frac{\partial^4}{\partial x^4} u(x, t) + \rho A \frac{\partial^2 u(x, t)}{\partial t^2} = F e^{i\omega_c t} \quad (1.13)$$

The solution of this equation has the form $u(x, t) = u(x) \exp(i\omega_c t)$. The amplitude $u(x)$ may be complex, so that the motion is not necessary in phase with the force F . Expanding the displacement in terms of the eigenfunction u_n ,

$$-\omega_c^2 \rho A \sum_{n=1}^{\infty} a_n u_n(x) + EI \sum_{n=1}^{\infty} a_n \frac{\partial^4 u(x)}{\partial x^4} = F \quad (1.14)$$

From this equation we can express the amplitude as:

$$a_n = \frac{1}{\rho A \ell^3} \frac{1}{\omega_n^2 - \omega_c^2 + i\omega_n^2 / Q} \int_0^l u_n(x) F dx \quad (1.15)$$

Here Q is the quality factor of the doubly-clamped beam. Equation (1.15) gives the correlation between the driving force and the vibration amplitude of mechanical element.

1.3 Fabrication of micro- and nano-electromechanical devices

The fabrication processes of MEMS and NEMS devices can be classified into two approaches. Top-down approaches, which developed from the semiconductor fabrication technology, utilize micro or nano fabrication techniques, such as electron-beam lithography, thin-film growth techniques and etching techniques to fabricate structures from bulk material, either membranes or bulk substrate. Bottom-up approaches fabricate the nanoscale devices by sequential assembly of atoms and molecules as building blocks, and then connect them to the outside world.

The devices which are used in this project are fabricated on silicon-on-insulator (SOI) wafers, as showed in Figure 1.3 (a), with top-down approaches. SOI is a sandwich structure with one silicon dioxide layer located in the middle between the device silicon layer and the substrate silicon. In our experiment, we choose the SOI wafers whose thickness of the structural Si is $5\mu\text{m}$ and sacrificial SiO_2 layer is $4\mu\text{m}$. The wafers are fabricated with a bonding and etch-back technique, which can result in smooth interfaces.

Before the fabrication, the SOI wafer is required to be cleaned. The process is that the SOI wafer is etched with BOE for 30 seconds to avoid thin silicon dioxide at the surface and then the DI water is used to rinse the wafer to make sure no BOE on the surface of the wafer. After that the wafer is put into piranha solution (H_2SO_4 : $\text{H}_2\text{O}_2=3:1$) to clean organic residues off the substrate for 20 minutes because piranha solution is a strong oxidizer and it will remove most organic matter. Thus after rinsing and drying, the cleaned wafer can be used for MEMS fabrication.

The first fabrication process of our MEMS devices is sputtering which will deposit metal layers to the surface of the wafer. The layers will act as the bonding pad and the tunneling surface. Since tunneling takes place between the atoms on the surfaces of the tunneling electrode, it is critically important that electrode material would be conductive to tunneling such as metallic layers. Au film is a nearly ideal metal layer for this purpose because it does not undergo chemical reactions to form insulating surface layers when exposed to air. Based on our experimental requirement, the layers are chosen to be the double layers - gold and chromium. Chromium is selected due to its ideal adhesion properties to Si surface and Au surface. Au has a good tunneling surface for STM and bonding wire. Thus a thickness of 20 nm chromium layer will be deposited at the surface of silicon and a thickness of 200 nm gold layer is coated on the chromium layer, as shown in Figure 1.3 (b). Because the electron tunneling is just happened in angstrom scale, the rough characterization of the sample surface will impact the measurement result. In order to see the situation of the Au surface of the sample, small measured area is scanned with the STM and the images of the topography for Au surface are shown in Figure 1.4. The images show the change of the sample surface. Due to lack of standard correction of the piezo driver motion, the images do not show the detailed values for the change of the topography of the scanning area and just show some compared change.

After sputtering, photolithography process is used to define MEMS device patterns. Photolithography process is an important step to decide the future size of

devices. In the photolithography process, one starts the fabrication by spin-coating photosensitive organic film, namely the photoresist, upon the wafer where the structures will be fabricated, shown in Figure 1.3 (c). The coated wafer is soft-baked for a few minutes to dry out the solvent, hardening the coating layer. The photoresist is then exposed to ultraviolet (UV) light through the patterned photo-mask, thereby transferring the pattern on the mask onto the photoresist. The common exposure process is contact exposure and is shown as Figure 1.2. In our experiment we choose contact exposure, because the MEMS are fabricated. The exposed wafer is put into developing solution to remove the part out of the devices. Thus the patterns are defined.

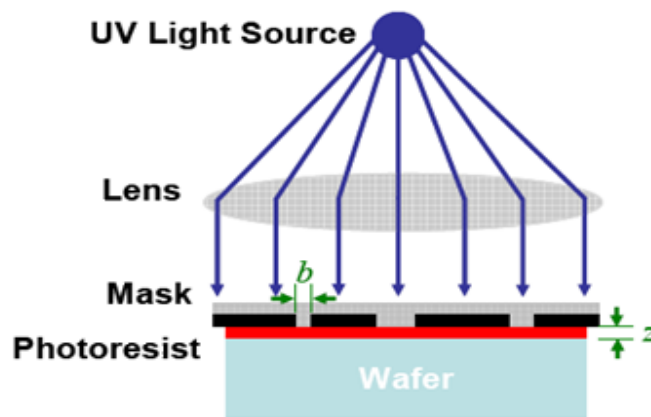


Figure 1.2 Schematic drawing illustrating contact exposures of photolithography.

The patterns of MEMS devices are transferred to the wafer through it.

Following the photolithography, the wafer with device patterns is sent to etch away the extra bilayers and silicon. The wet etch is used to remove the bilayers, Au and Cr. After that, photoresist of wafer surface is lifted with acetone and the metal shown in Figure 1.3(d) can be served as a robust mask protecting the thin Si which will become the device. The unprotected silicon area is etched through into the SiO_2 layer with reactive ion etching (RIE), as shown in Figure 1.3(e). Based on big selective ration between Si and Silicon dioxide, during the RIE over-

etching is required and this can avoid leaving a thin silicon layer at the surface which will block to remove the sacrificial SiO_2 layer.

The last step of fabrication is to etch the sacrificial layer of SOI and release the devices. The wafer is put into the BOE solvent and the silicon dioxide is etched. The time is controlled in order to get the suspended NEMS structures as shown in Figure 1.3(f). After the wafer is taken out of the BOE etchant, it is rinsed in multiple DI water baths to make sure no BOE solvent is left. Thus the devices are done. We will dice the wafer into single device die for measurement.

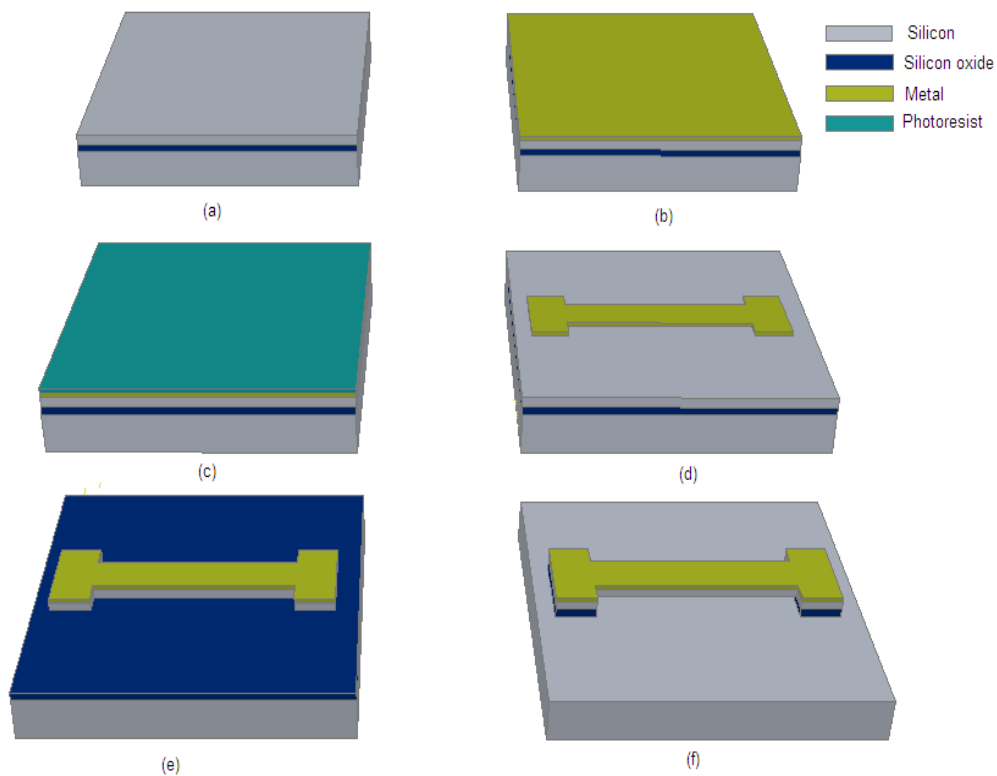


Figure 1.3 The process steps to fabricate suspended doubly clamped beam with photolithography. (a) SOI wafer. (b) The wafer is coated with metal layers (Au and Cr). (c) The wafer is coated with metal layers and photoresist. (d) Metal layers are patterned with photolithography and etched. (e) Bilayers and Silicon layer are etched away. (f) Silicon dioxide layer is etched through and a suspended doubly clamped beam is done.

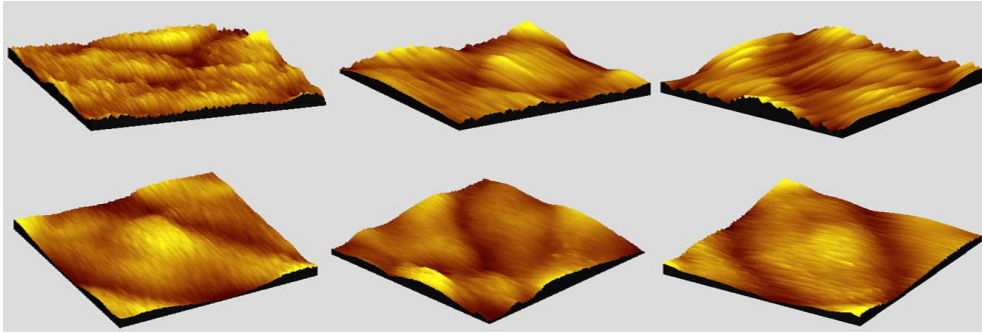


Figure 1.4 Topographies of Au film on the sample surface. Images show the surface rough characterization of the Au film for different scanning areas. The measurement conditions are: DC bias voltage 0.5 V, DC setpoint 0.3 nA, scanning speed 0.5 $\mu\text{m/s}$ and time constant 51.34 ms.

One important problem for the devices using this fabrication process is stiction. When the devices are removed from solution, the surface tension in the liquid pulls the suspended structures down to the surface. Once this occurs, the structures remain stuck and are effectively damaged (unusable). Though careful fabrication is done, these problems can't always be avoided and this impacts the yield. The doubly-clamped and stiffer nature of the devices is chosen to help to avoid this issue to a degree while at the same time helping to allay snap-to-contact issues with the STM tip.

1.4 Displacement detection of NEMS

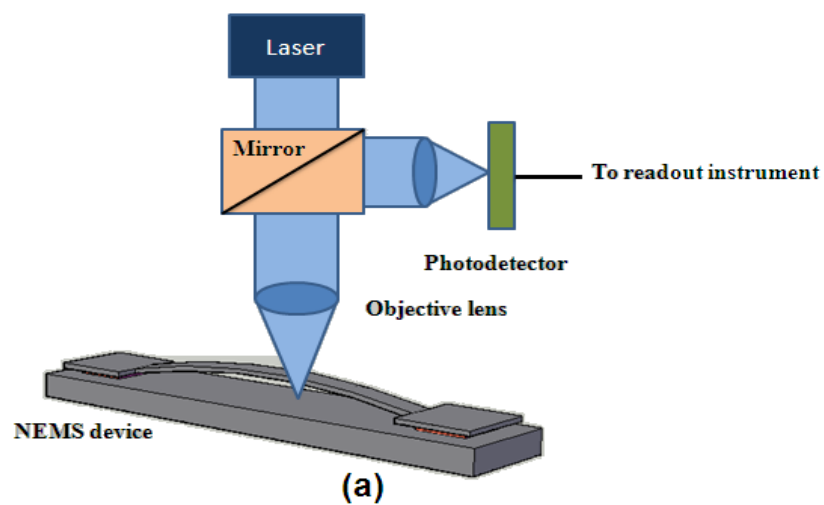
The miniscule MEMS and NEMS own high sensitivities and tiny displacement when they are driven. Thus the detection of tiny displacement for MEMS and NEMS is an important problem. Before we introduce our project and technique, I will simply introduce some techniques which are available for displacement detection.

1.4.1 Optical Technique

Optical interferometry which combines two or more light waves in an optical instrument in such a way that interference occurs between them has been used in

the NEMS domain [16] [17] [18] to detect the motion. There are two popular methods: path-stabilized Michelson interferometry and Fabry-Perot interferometry. In the case of Fabry-Perot interferometry, the optical cavity which is formed between the NEMS device and the silicon substrate can modulate the optical signal on a photodetector as the NEMS device moves along with the optical beam direction. Figure 1.5(a) displays schematic diagrams of Fabry-Perot interferometry. In path-stabilized Michelson interferometry, a focused laser beam reflects from the surface of a vibrating NEMS device and interferes with a stable reference beam, as shown in Figure 1.5(b).

Optical methods provide a non-contact means for displacement detection and are desirable because of their demonstrated sensitivity and broadband operation. However, in both of the above-described techniques, strong diffraction effects emerge as the NEMS dimensions are reduced beyond the optical wavelength used. The light collected by the probing lens is reduced to a small fraction of the incoming light due to strong scattering. This strong scattering, accompanied with the requirement that low optical power levels must be used for probing NEMS due to the heating effect, make optical displacement detection difficult for the smaller devices.



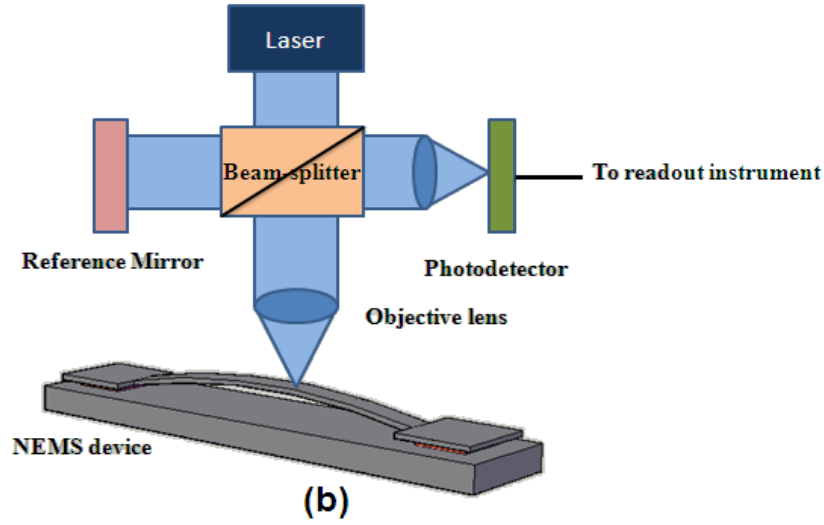


Figure 1.5 Optical displacement detection technique (a) The schematic diagram of Fabry-Perot interferometry (b) The schematic diagram of Michelson interferometry

1.4.2 Magnetomotive Techniques

Magnetomotive displacement detection technique has been employed into the NEMS domain by Cleland and Roukes in 1996 [19]. A uniform magnetic field is applied to a conducting nanomechanical element. When the nanomechanical element is moving, the time-varying flux generates an induced electromotive force (emf) in the loop, which, in turn, can be picked up by the detection circuit. For a doubly clamped beam, the Magnetomotive technique generates an emf voltage given by

$$V_{emf}(t) = \xi l B \dot{u}(t) \quad (1.11)$$

Here B is the magnetic field strength, l is the length of the beam, ξ is a geometric factor ($\xi \approx 0.885$ for a doubly clamped beam) [20], $u(t)$ is the displacement of the midpoint of the beam and the beam is assumed to exhibit constant amplitude harmonic oscillations at a frequency ω . For extremely small displacement, the emf which is generated due to the motion of NEMS will be small. Thus a low-noise

amplifier is required to amplify the signal. Figure 1.6 shows the magnetomotive displacement detection. This method has been efficient for VHF and ultrahigh frequency (UHF) NEMS [21] [22].

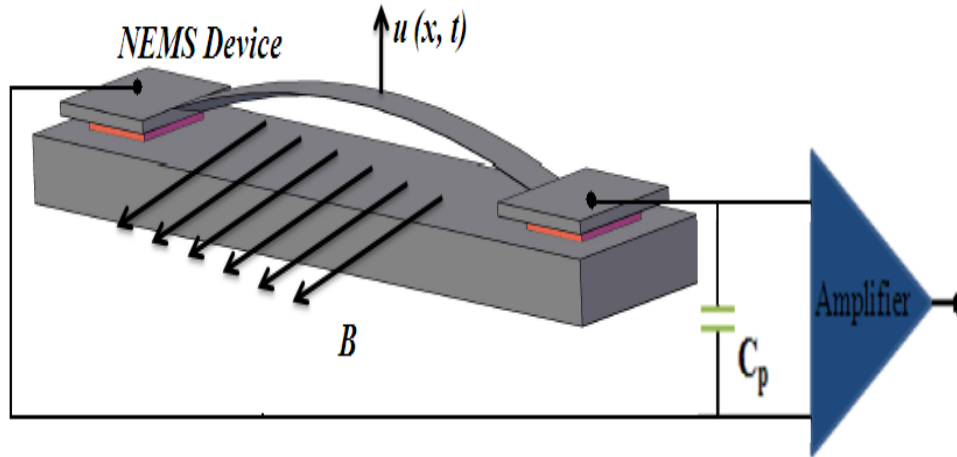


Figure 1.6 The schematic diagram of magnetomotive displacement detection Technique. Here B is magnetic field strength and C_p is the parasitic capacitance

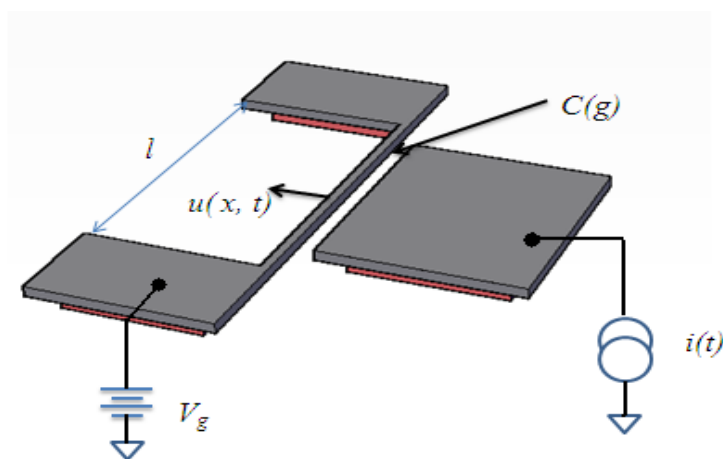
Due to the parasitic capacitances in the detection circuit, the detection bandwidth of the magnetomotive technique is limited. In order to detect high frequency NEMS motion, small parasitic capacitance and resistance are required and these limit the development of this technique. Also there are difficulties associated with implementing the magnetomotive detection scheme when the device is being actuated by electrical or magnetomotive actuation. Because the degree of orthogonality of the actuation and detection is reduced by the parasitic capacitance between the input and the output, this makes the implementing of magnetomotive detection difficult [23]. Some methods are investigated to solve this problem, such as a reflection measurement scheme.

1.4.3 Capacitive Displacement Detection

In capacitive displacement detection, the electrical capacitance between the mechanical device and a fixed gate is varied with the motion of mechanical device.

The basic configuration is shown in Figure 1.7(a). A DC bias voltage is applied on the capacitor and a change in the voltage (current flow) across the capacitor is detected. It can be understood from the definition of capacitance, $Q=CV$ and $dQ = VdC + CdV$. Consequently, a capacitance change at constant current (voltage) will generate a voltage (current flow) across the capacitor. Here, Q is the charge on the capacitor and V is the voltage across capacitor. Figure 1.7(b) shows an implementation along with a conceptual detection circuit. The parasitic capacitance in this measurement scheme will be extremely important. The parasitic capacitance determines the detection bandwidth and the limits of capacitive detection of motion.

Some ways can be used to eliminate the effect of the parasitic impedance. Balanced bridge techniques may help readout the small dynamic capacitance changes efficiently by negating the capacitive background. Impedance matching technique by using an LC impedance transformation network is developed to measure the small motion of NEMS [24]. One could also use the mixing techniques to measure the mixing signal [25]. Otherwise, a single-electron transistor (SET) has been used to measure a NEMS resonator with the NEMS electrode serving a dual function as both the motion sensor for the NEMS, and as the gate electrode of the SET readout [26] [3].



(a)

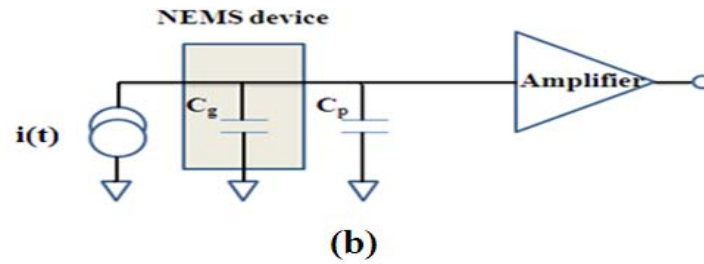


Figure 1.7 Capacitive displacement detection technique (a) Schematic diagram of capacitive detection in plane motion of a doubly clamped NEMS beam (b) The circuit of capacitive detection. The capacitance C_g is related to the motion of NEMS device and C_p is parasitic capacitance.

1.4.4 Piezoresistive and Piezoelectric Detection

A piezoresistive material is one that exhibits a changing electrical resistance due to applied mechanical stress. Similarly, a piezoelectric material can generate an electrical polarization change in response to applied mechanical stress. Both the effects are sensitive to the stress generated inside a material during the motion. One can use it to do displacement detection.

Piezoresistive sensing can be realized by detecting the resistance changes through a piezoresistive NEMS device as it is actuated. Compared with other detection methods, piezoresistive NEMS have the advantages of being easily integrated sensors that can operate from room temperature down to at least 4 K and do not require magnetic field. The shortcoming of this sensing technique, however, is the intrinsically high resistances (5-500 k Ω) of these devices which lead to frequency-dependent signal attenuation at MHz frequency if direct-current (dc) biasing is used. In order to use this method for the high frequency, one investigates some ways, such as piezoresistive signal downmixing [27].

In the piezoelectric method, one exploits the polarization fields created by the stress field within the piezoelectric nanomechanical element as it moves. This method also has problems at high frequency. Some people have intended

piezoelectric detection in NEMS using a single-electron transistor [28] to improve this method.

1.4.5 Electron Tunneling Detection

Displacement transducers based on electron tunneling have been proposed for a variety of physical sensors, because of the high position sensitivity of electron tunneling. Advantages of electron tunneling displacement transducers include high sensitivity, small transducer size, and compatibility with silicon micromachining technology. The tunneling transducer is generally realized in the form of a sharp tip placed within a fraction of a nanometer of the moving mechanical element. The tip can convert the motion of the mechanical element into an electron signal by the change of tunneling current. The tunneling current is very sensitive to the distance change between the tip and the surface of the sample due to the exponential correlation with the distance. An electron tunneling transducer followed by an amplifier (current-to-voltage converter) is displayed in Figure 1.8.

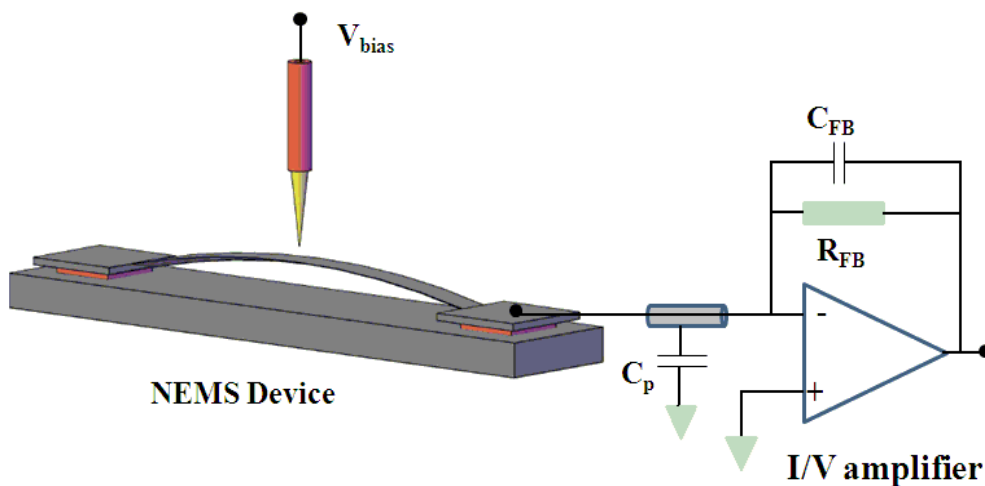


Figure 1.8 Schematic diagram of electron tunneling displacement detection technique. Here C_{FB} is feedback capacitance, R_{FB} is the feedback resistance and C_p is the parasitic capacitance which limits the output frequency.

Electron tunneling transduction as shown in Figure 1.7 has a limit for high frequency application due to the parasitic capacitance C_p coming from macro wiring and high impedance of the tunneling junction resistance. Usually the limit of frequency is about 10 KHz and this obstructs the development of electron tunneling transducers at high frequency. In our thesis we will focus on the improvement of electron tunneling transducer as displacement detection, particularly for frequencies above the traditional STM bandwidth.

1.5 Motivation of This Thesis

The capabilities of the scanning tunneling microscope (STM) as an imaging tool are well known and appreciated. Also the capabilities of the tunneling probe of the scanning tunneling microscope as a displacement sensor attract attention. Tunneling of electrons through the space separating two electrical conductors is a special event of the quantum nature of matter. One observes that the tunneling current between two conductors separated by vacuum is exponentially dependent on the gap with a scale of a few angstroms, so the small displacement of NEMS can be captured with the electron tunneling sensor.

Although electron tunneling detection has its advantages, some factors limit its development. As we know, in normal STM operation, there is a constant resistance R_T from $1M\Omega$ to $1G\Omega$ which is located between the tip and the sample. This resistance will form a RC circuit with the stray capacitance C_p coming from macroscopic wiring to limit the bandwidth to $1/2\pi R_T C_p \sim 10kHz$, as shown in Figure 1.8. This frequency limit is far from the fundamental limit of electron tunneling, I_T/e , which is the tunneling rate of a single electron determined by its tunneling current and elementary charge e . For a STM system, the tunneling current I_T is around 1nA and this mean the available bandwidth of STM is around 1GHz.

Some methods have been demonstrated to achieving higher frequency resolution with the STM. Direct RF measurements on the tunneling current have shown signatures of electron spin resonance (ESR) at high frequencies [29] [30].

Employing several amplifier stages instead of a single trans-impedance amplifier [31] [32] improves the time resolution, but with an undesirable problem in the signal-to-noise ratio. By inserting a LC impedance transformation network [33] one can transfer the impedance of the tunneling junction resistance R_T down to 50-ohm, but this is difficult if the impedance mismatch ratio is greater than 100 and impractical if the same detection setup is to be used with many devices of different frequencies.

In our project, we will focus on the electron tunneling displacement detection technique and use the intrinsic properties of the NEMS and the exponential relationship between the tunneling current and the distance from the tip to the surface of sample to perform frequency downmixing of the signals. Thus a lower downmixed frequency signal which retains the high frequency motion information of NEMS can be detected by standard STM circuits without significant signal loss, because this output frequency is lower the cut-off frequency of the whole detection loop. With this method we can improve the detecting frequency to GHz and improve the sensitivity of motion.

REFERENCE

1. Roukes, M. L., Nanomechanical systems face the future, *Phys. World* 14, 25, (2001).
2. Cleland, A. N., *Foundations of Nanomechanics* (Heidelberg: Springer), (2002).
3. Naik, A., Buu, O., LaHaye, M. D., and Schwab, K. C., Cooling a nanomechanical resonator with quantum back-action, *Nature*, 443, 193, (2006)
4. O'Connell, A. D., Hofheinz, M., Ansmann, M, Bialczak, R. C., Lenander, M., Lucero, E., Neely, M., Sank, D., Wang, H., Weides, M., Wenner, J., Matinis, J. M., Quantum ground state and single-phonon control of a mechanical resonator, *Nature*, 464, 697, (2010)
5. Rocheleau, T., Ndukum, T., Maclin, C., Hertzberg, J. B., Clerk, A. A., Schwab, K. C., Preparation and detection of a mechanical resonator near the ground state of motion, *Nature*, 463, 72, (2010)
6. Yang Y. T., Callegar C., and Ekinci K. L., Zeptogram-Scale Nanomechanical Mass Sensing, *Nano Letters*, 6, 583, (2006).
7. Ekinci, K. L., Yang, Y. T., and Roukes, M. L., Ultimate limits to inertial mass sensing based upon nanoelectromechanical systems, *J. Appl. Phys.*, 95, 2682, (2004).
8. Naik, A. K., Hanay, M. S., Hiebert, W. K., Feng, X. L., and Roukes, M. L., Towards single-molecule nanomechanical mass spectrometry, *Nat. Nanotechnol.*, 4, 445, (2009)
9. Chiu, H. Y., Hung, P., Postma, H. W. C., and Bockrath, M., Atomic-scale mass sensing using carbon nanotube resonators, *Nano Lett.*, 8, 4342, (2008)

10. Sidles, J. A., Garbini, J. L., Bruland, K. J., Rugar, D., Züger, O., Hoen, S., and Yannoni, C. S., Magnetic resonance force microscopy, *Rev. Mod. Phys.*, 67, 249, (1995)
11. Rugar, D., Budakian, R., Mamin, H. J., and Chui, B. W., Single spin detection by magnetic resonance force microscopy, *Nature*, 430, 329, (2004).
12. Hammel, P. C., Seeing single spins, *Nature*, 430, 300, (2004).
13. Degen, C. L., Poggio, M., Mamin, H. J., and Rugar, D., Nanoscale magnetic resonance imaging, *PNAS*, 106, 1313, (2009)
14. Nguyen, C. T.-C., MEMS technology for timing and frequency control, *IEEE Trans. Ultrason. Ferroelectr. Freq. Control*, 54, 251, (2007)
15. Cleland, A. N., Roukes, M. L., Noise process in nanomechanical resonator, *J. Appl. Phys.*, 92, 2758, (2002)
16. Carr, D. W., Sekaric, L., and Craighead, H.G., Measurement of nanomechanical resonant structures in single-crystal silicon, *J. Vac. Sci. Technol. B*, 16, 3821, (1998)
17. Meyer, C., Lorenz, H., and Karrai, K. Optical detection of quasi-static actuation of nanoelectromechanical system, *Appl. Phys. Lett.*, 83, 2420, (2003)
18. Kouh, T., Karabacak, D., Kim, D. H., and Ekinci, K. L., Diffraction effects in optical interferometric displacement detection in nanoelectromechanical systems, *Appl. Phys. Lett.*, 86, 13106, (2005)
19. Cleland, A. N., and Roukes, M. L., Fabrication of high frequency nanometer scale mechanical resonators from bulk Si crystals, *Appl. Phys. Lett.*, 69, 2653, (1996)

20. Cleland, A. N., and Roukes, M. L., External control of dissipation in a nanometer-scale radiofrequency mechanical resonator, *Sensors and Actuators*, 72, 256, (1999)
21. Feng, X. L., White, C. J., Hajimiri, A., and Roukes, M. L., A self-sustaining ultrahigh-frequency nanoelectromechanical oscillator, *Nature Nanotech.*, 3 342, (2008)
22. Karabalin, R. B., Feng, X. L. and Roukes, M. L., Parametric Nanomechanical Amplification at very high frequency, *Nano Lett.*, 9, 3116, (2009)
23. Ekinici, K. L., Electromechanical transducers at the nanoscale: actuation and sensing of motion in nanoelectromechanical systems (NEMS), *Small*, 1, 786, (2005)
24. Truitt, P. A., Hertzberg, J. B., Huang, C. C., Ekinici, K. L. and Schwab, K. C., Efficient and sensitive capacitive readout of nanomechanical resonator arrays, *Nano Lett.*, 7, 120, (2007)
25. Sazonova, V., Yaish, Y., Ustunel, H., Roundy, D., Arias, T. A., and McEuen, P. L., A tunable carbon nanotube electromechanical oscillator, *Nature*, 431, 284, (2004)
26. Blencowe, P. M., Wybourne, N. M., Sensitivity of a micromechanical displacement detector based on the radio-frequency single-electron transistor, *Appl. Phys. Lett.*, 77, 3845, (2000)
27. Bargatin, I., Myers, E. B., and Roukes, M. L., Sensitive detection of nanomechanical motion using piezoresistive signal downmixing *Appl. Phys. Lett.*, 86, 133109, (2005)
28. Knobel, R., Cleland, A. N., Piezoelectric displacement sensing with a single-electron transistor, *Appl. Phys. Lett.*, 81, 2258, (2002)

29. Manassen, Y., Hamers, R. J., and Castellano, Jr., Direct Observation of the Precession of Individual Paramagnetic Spins on Oxidized Silicon Surfaces, *Phys. Rev. Lett.*, 62, 2531, (1989)
30. Durkan, C., and Welland, C. E., Electronic spin detection in molecules using scanning-tunneling-microscopy-assisted electron-spin resonance, *Phys. Rev. Lett.*, 80, 458, (2002)
31. Mamin, H. J., Birk, H., and Rugar, D., High-speed scanning tunneling microscopy: principles and applications, *J. Appl. Phys.*, 75, 161, (1994)
32. Rost, M. J., Crama, L., and Han, H. et al., Scanning probe microscopes go video rate and beyond, *Rev. Sci. Instrum.*, 76, 053710, (2005)
33. Kemiktarak, U., Ndukum, T., Schwab, K. C., and Ekinci, K. L., Radio-frequency scanning tunneling microscopy, *Nature*, 450, 85, (2007)

Chapter 2 Experimental Instrument

We first present the experimental instrument scanning tunneling microscope (STM) [1] which will be used in downmixing readout of nanomechanical motion. The basic STM system is simply introduced and two operation modes of STM are described. We will talk about some modifications which are done in our system in order to adapt to our project and the general set-up. Simple operation of STM is described in the last section.

2.1 Scanning Tunneling Microscopy (STM) system

As a tool to investigate the surface of conductive sample Scanning Tunneling microscopy (STM) is a type of electron microscope and was invented by Binnig and Rohrer in 1981. It is only one year later when the same group achieved an atomically resolved real space image of Si (111)-7x7 structure using STM [2]. Because STM work theory which is based on the concept of quantum tunneling and is sensitive to the small distance change, STM become a powerful instrument that can obtain atomic resolution on a metal, semiconductor or other conductive sample surface. When a conducting tip is brought very near, approximately 1nm, to a metallic or semiconducting surface, a bias between the two electrodes can allow electrons to tunnel through the gap between them because the electron wave functions of the tip and the sample slightly overlap in this distance. Both this overlap and the current exponentially decrease with the distance between the tip and the sample [3]. The schematic diagram of a scanning tunneling microscope is shown in Figure 2.1.

Usually, for STM system it can be operated in two modes which are called constant height mode and constant current mode respectively. For constant current mode, a feedback network changes the height of the tip at z direction to keep the current constant. The displacement of the tip given by the voltage applied to the piezoelectric driver then yields a topographic map of the surface. Figure 2.2(a) show a typical current mode operation and the change of current and position

during scanning. Alternatively, in constant height mode, the voltage applied to the piezoelectric driver and the height are both held constant while the current change to keep the voltage from change; this leads to an image made of current changes over the surface, which can be related to charge density, as displayed in Figure 2.2(b). This mode is practical for very small scan range or even for large scans at a flat surface which parallel the plane of the tip moving. Compared two modes, constant height mode is faster, because the piezoelectric movements require more time to response the change in constant current mode than the current response in constant height mode. When STM is used to as displacement transducer, it can be operated in either mode depended the vibration amplitude of devices. But for constant height mode, we should carefully use to avoid damaging the devices and tip.

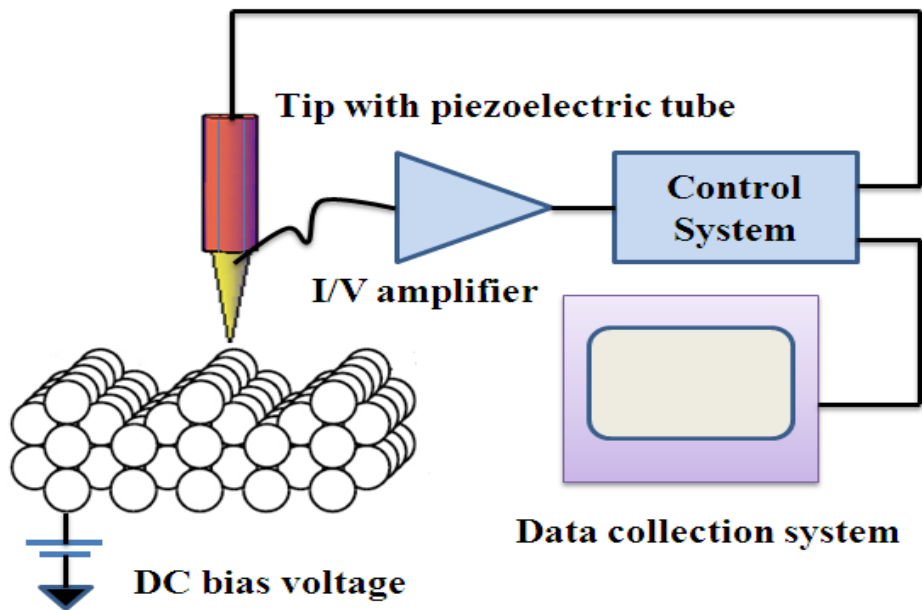


Figure 2.1 Schematic diagram of a scanning tunneling microscope. The tip of the STM is mounted on piezo driver assembly and can move along X, Y and Z direction, separately. During scanning, due to the change of the distance from tip to the surface of sample, the tunneling current change. This change can be amplified by I/V amplifier and recorded by data collection system.

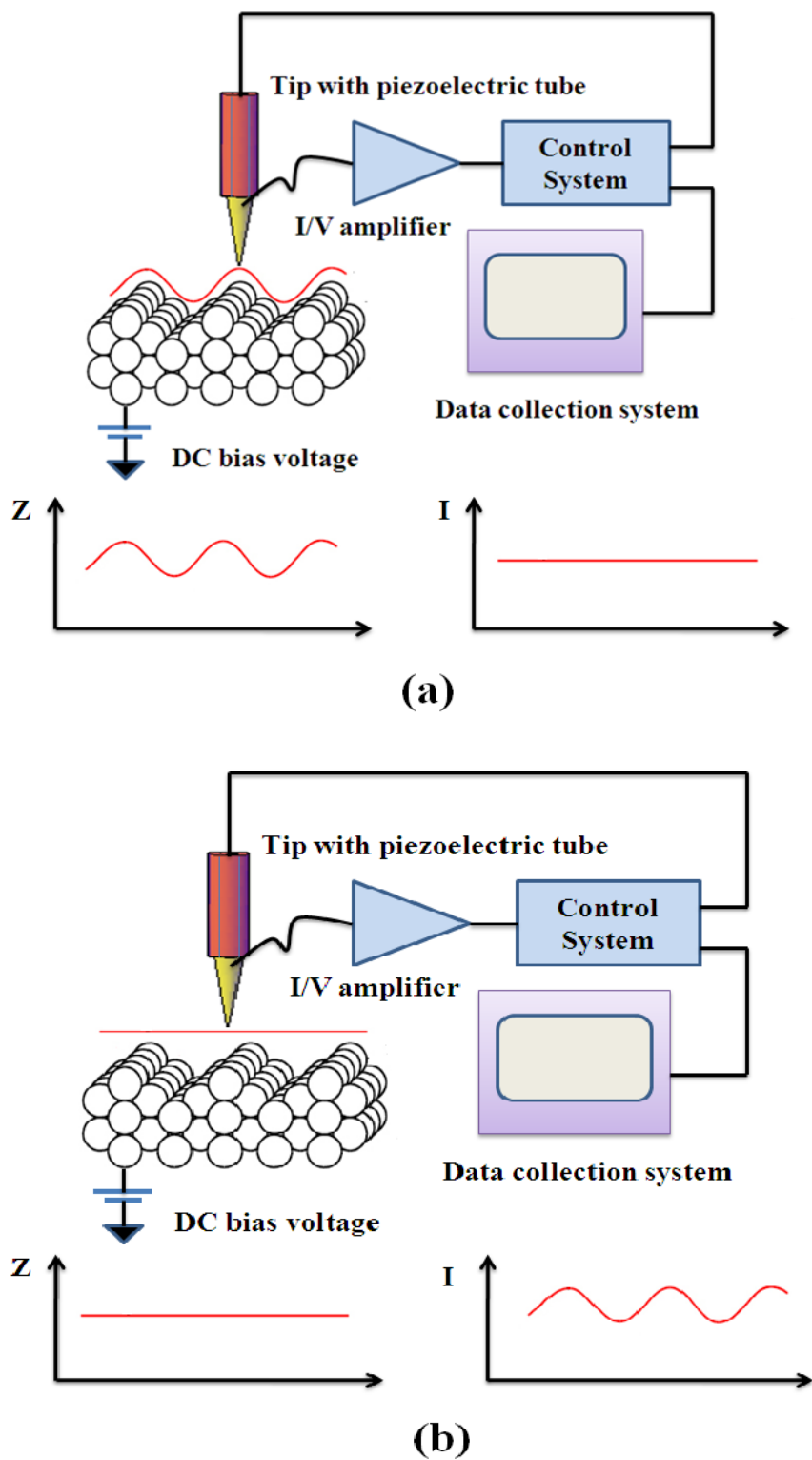


Figure 2.2 The schematic of two operation modes in STM (a) Constant-current mode. (b) Constant-height mode.

2.2 The adaptations of the STM system

In our experiment, the STM system is the 1988 IBM model shown in the Figure 2.3. In order to make this STM an electron tunneling transducer for frequency downmixing readout, some updates and modifications were required. The approach system mechanical lever advantage was moved to either side to avoid direct contact with the device under test. The sample holder was correspondingly changed as well as updated for large range X and Y motion. A vacuum chamber was built around the STM system with multiple optical and electrical entry port options. An optical telescope for sample visual positioning while in vacuum was added. Finally, the electrical control system and software was updated

2.2.1 Modification of Mechanical Part of STM

For the STM mechanical parts, some adaptations are required to meet the measurement requirement of STM downmixing readout. These mainly include the approaching system and the sample holder.

For the approaching system of STM, the adjustment stop is redesigned. The old adjustment stop is too close to the tip as shown in Figure 2.3 inset which leave very little room for the sample to fit in. This will cause some problems. Firstly, the sample will be damaged due to the crash by the adjustment stop if the sample can't fit in the small space. It is not convenient for moving the sample large distance over X and Y with response to the tip, it also makes aligning the tip on top of the sample difficult. Secondly, it is tedious to align the adjustment stop to the tip. Based on these problems, a new adjustment stop is designed and shown in Figure 2.4. These new support arms can avoid the above problems, but they require that the arms must be level in order to avoid the shift of chip due to unbalanced force in the two arms. This approaching system has the disadvantage that it is difficult to set the length of arms in order to ensure the sample is vertical to the tip.

The second problem is how to align the probe tip on the top of NEMS device. The optical telescope is about 10cm from the sample (see Figure 2.9) and thus limited to a numerical aperture around 0.2. Combined with a glancing viewing angle, NEMS devices are too small to be accurately landed on with aid of the telescope. With a mirror in improving the view angle rough alignment of NEMS devices with the probe tip become possible, however, fine alignment will still be necessary to successfully land the tip on a NEMS. For the fine alignment, some new techniques will be required. Electron field emission from the tip, as one example, may be a good method to find the NEMS devices. Our initial attempts to implement field emission fine alignment were unsuccessful due to dull and double tip shapes (see Figure 2.7). Based on this reason, in our experiment we measure MEMS-sized-devices. With the mirror, the MEMS devices can be aligned well, that is, the tip can be reliably placed onto the MEMS beams. The image of sample and tip is shown in Figure 2.5.

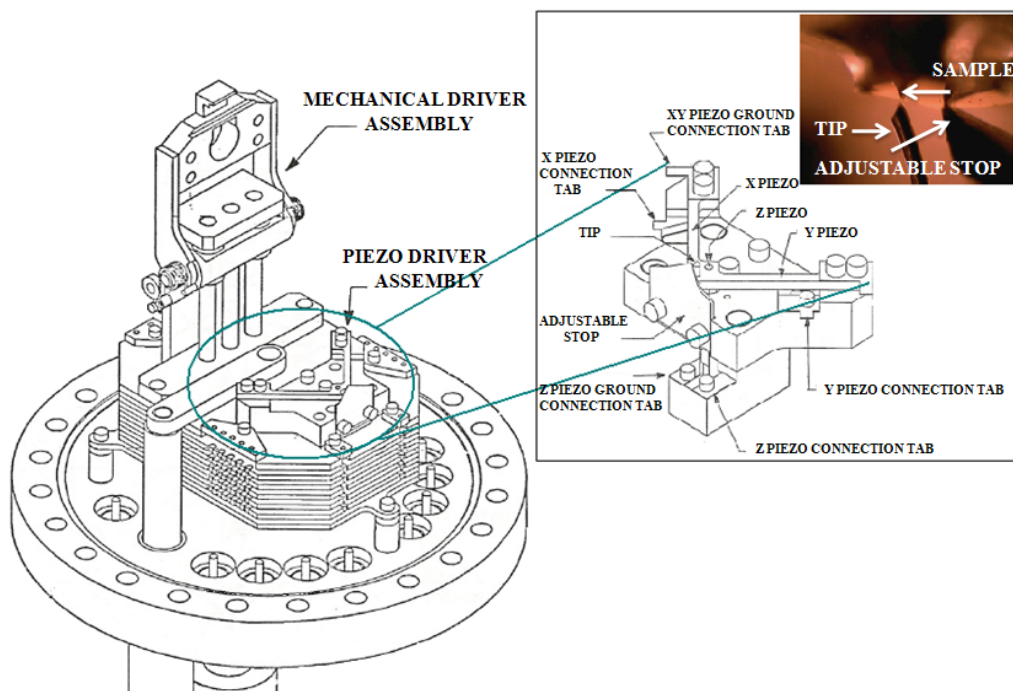


Figure 2.3 STM mechanical parts and old adjustable stop assembly (Inset). The image (Inset) shows a small room between the tip and the adjustable stop for sample fit in. (IBM STM operation manual)

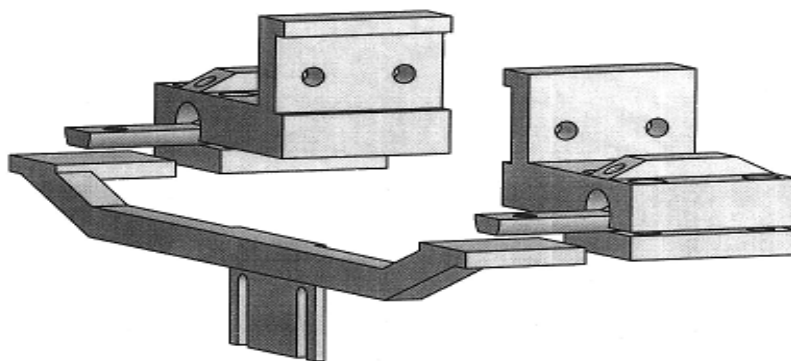


Figure 2.4 The schematic of new adjustable stop of STM which is used to replace the old adjustable stop of STM to provide big room to fit sample into STM system

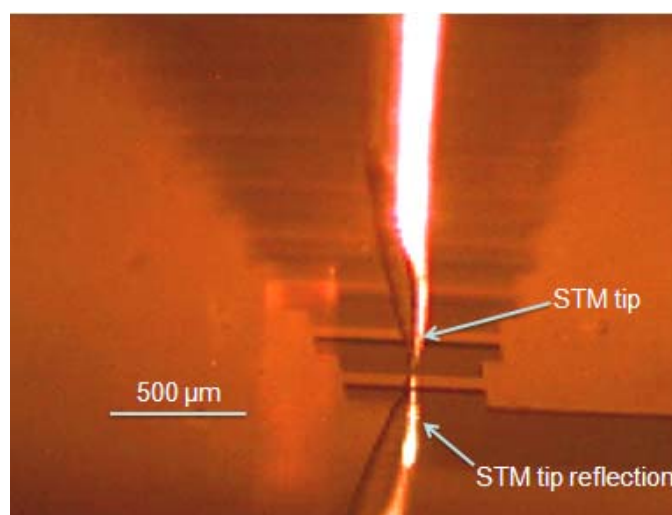


Figure 2.5 The image comes from the mirror which shows the tip aligned on the top of MEMS device with the telescope

One problem introduced by the alignment mirror, which is attached to the new mechanical advantage holder, is that it seems to cause significant additional mechanical noise of the measurement system and negatively impacts the sensitivity of the STM system. Additional work is needed in the future in order to overcome this mechanical noise. Similarly, field emission fine alignment will require future work in improved tip profiles.

We need to have a sample holder which can move along the XY plane in order to align on-chip features under the STM. The older sample holder is shown in Figure 2.6 (a) and it cannot move. This is not convenient to the alignment of sample and probe tip. In order to overcome this problem, a new sample holder is made like Figure 2.6(b). This new sample holder integrates an attocube system, as shown in Figure 2.6 (c). The new sample holder allows the sample to move large distance along X and Y directions with nm step resolution and it is convenient to align the probe tip on the top of MEMS devices.

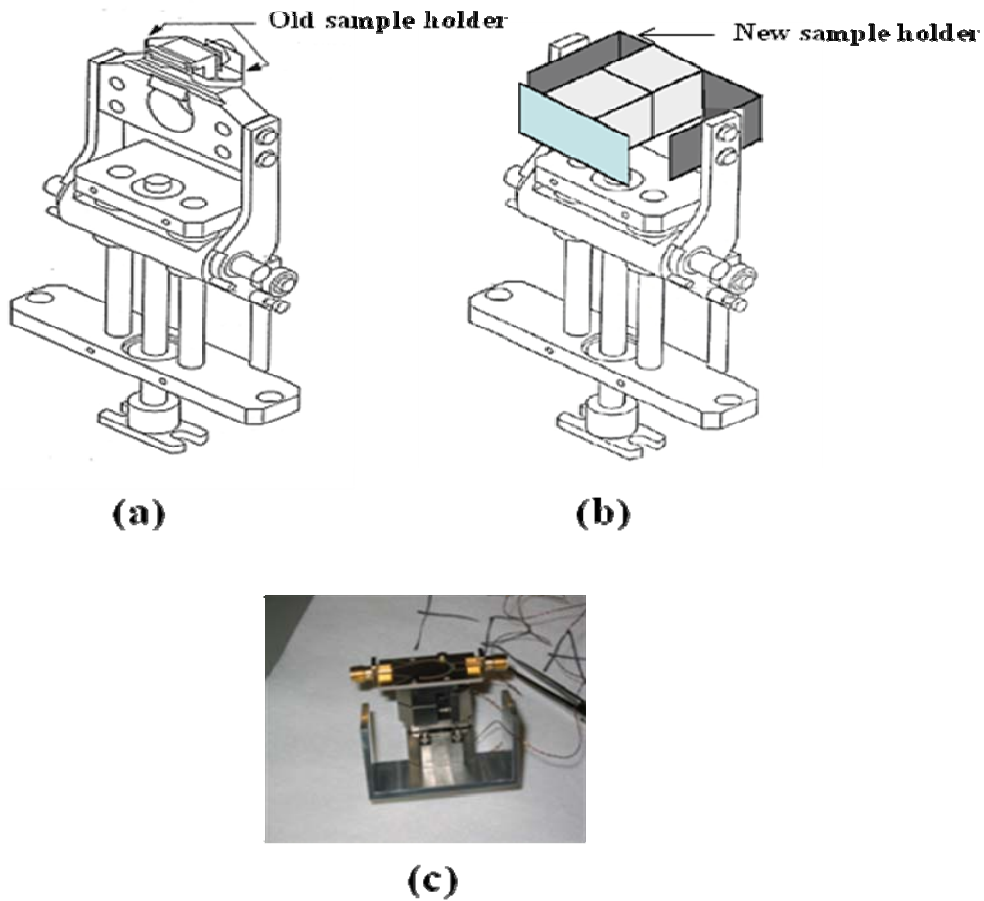


Figure 2.6 The schematic diagram for modification of sample holder (a) The old sample holder (b) The scheme of new sample holder and (c) The picture of the new sample holder with Attocube System which can move along X and Y Plane. (Image a and b modify from IBM STM operation manual)

These adaptations make our STM mechanical part convenient for our measurement, although this system still has some problem which will require improving for finer feature measurement. Now it basically meets our measurement requirement for MEMS.

2.2.2 The Accessories of STM System

The accessories of STM system include an electrical control box, software, optical telescope, tip, vibration isolation table and vacuum chamber. We will simply present them here.

The electrical control system is commercial SPM 100 control system and control software XPM 2.0. Both of them are from RHK Technology Company. For this system, we choose high sensitive IVP-300 I/V Pre-amplifier which has 1×10^9 gain, 5 KHz bandwidth, RMS noise 0.65 pA at 1.5 KHz and 100pF input capacitance and the minimum tunneling current 1pA [4]. This system is controlled by the RHK software XPM 2.0 and is connected to the chamber of STM.

For the STM tip the noble metals are chosen. A very common tip material is Pt-Ir, which is used in all of the experiments described in this thesis. Pt is a noble metal so it does not oxide when it is exposed to oxygen/air and Ir is added to Pt to increase the stiffness of the tip and create a more stable tip. For most application, a Pt-Ir wire is cut with a wire cutter to form a tip. The tip which is cut with a wire cutter often has two tips on the top, as shown in Figure 2.7 (a). The Pt-Ir wire could also be etched to form a sharp tip or cut by focused ion beam (FIB), but we have not yet implemented these strategies for this experiment. Another metal which is usually used as STM tip is W which can be created as a sharp tip with an etch process. However, W oxidizes in air and requires in situ treatment to remove the oxide layer in the vacuum chamber. In our experiment, we use wire cutters to cut Pt-Ir wire to form STM tips and carefully choose, via SEM inspection, in order to avoid the double tips which can greatly complicate the measurement data. Figure 2.7(b) shows the tip which is used in our measurement.

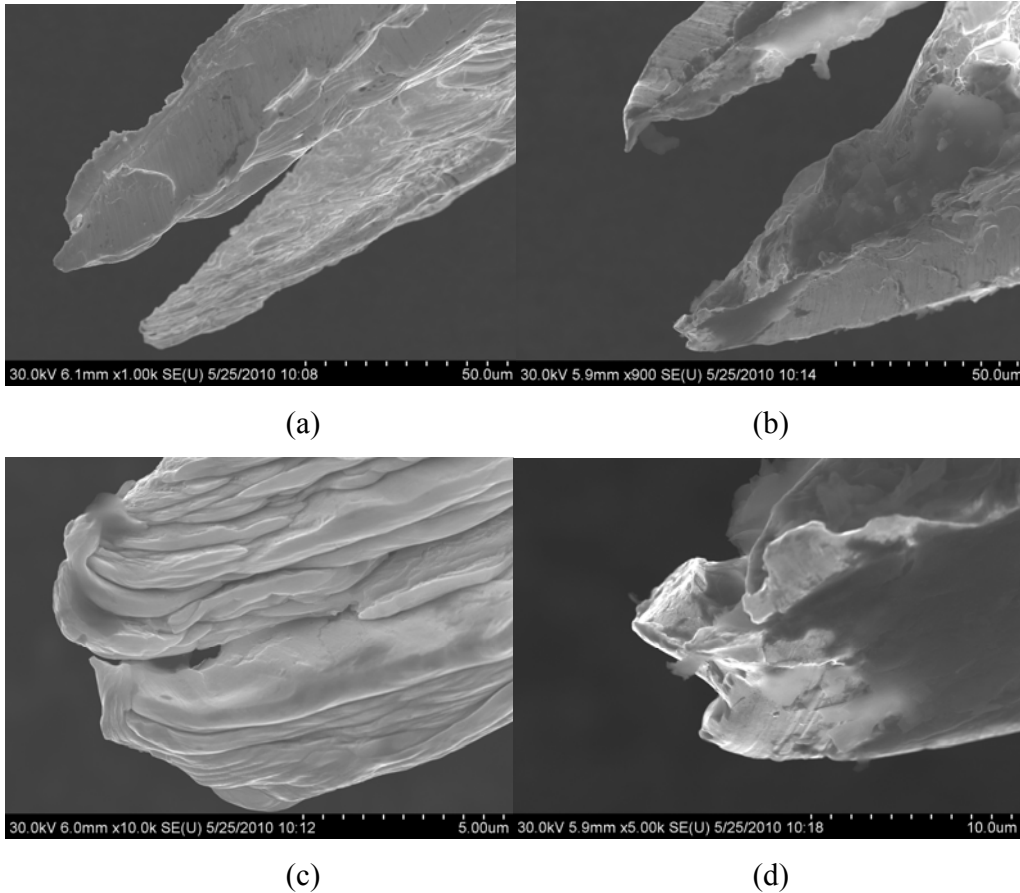


Figure 2.7 STM Pt-Ir tip SEM Image fabricated with wire cutter. (a) Two tip apices close each other (b) Two tip apices with a big gap (preferred) (c) High resolution image for one tip apex of the image (a) (d) High resolution image for one tip apex of the image (b) (preferred).

In order to avoid the air damping for MEMS device motion, the measurement is done in a high vacuum chamber whose pressure is lower than 10^{-6} torr. For this STM vacuum chamber, the turbopump and ion pump are used together in order to decrease the mechanical vibration noise. The turbo pump is used to pump roughly the chamber for high vacuum to about 10^{-5} torr, where the ion pump can start to work, and then ion pump is turned on to pump higher vacuum and to sustain the vacuum for measurement. A gate valve can then be closed and the turbo pump turned off, even removing the turbo pump connection to best mechanically isolate the chamber from the outside world. As we know the ion pump works quietly and does not make mechanical vibration noise like turbopump does. But the principle

of the ion pump is that an ion pump ionizes gases and employs a strong electrical potential, typically 3 kV to 7 kV, to accelerate them into a solid electrode. Thus when the ion pump is working, unfortunately, it creates electrical noise. In our STM system, the ion pump makes a 70 KHz electrical noise in the tunneling current and this noise can be found from FFT current information of RHK system spectrum analyzer, as shown in Figure 2.8 (a). This noise can impact the sensitivity of the measurements. Actually, in our measurement it has a small impact, because there are other noises, as shown in Figure 2.8 (b), which are dominant and will have the main impact on the sensitivity of the measurement

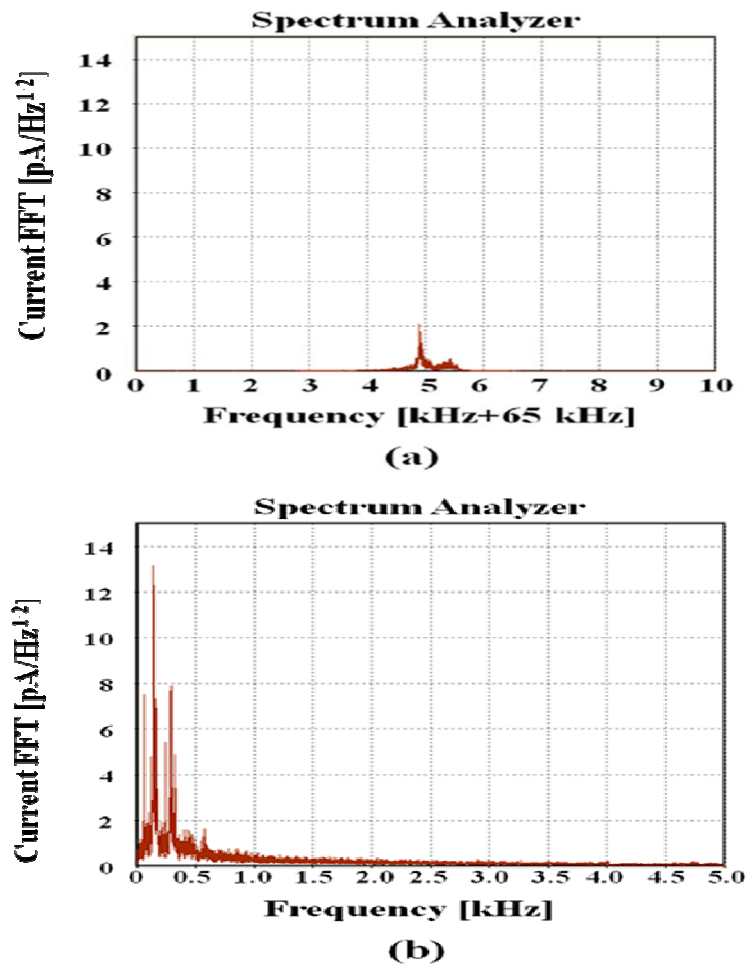


Figure 2.8 The spectrum of noise of tunneling current in STM system (a) The ion pump noise spectrum (b) Other noise spectrum coming from electrical and mechanical source

The mechanical noise will badly impact the sensitivity of STM system, because electron tunneling is sensitive to small distance changes. In order to further reduce the noise in the STM system, the STM vacuum chamber is put on a vibration isolation table (see Figure 2.10). This table will decrease the mechanical vibration effect from building and so on.

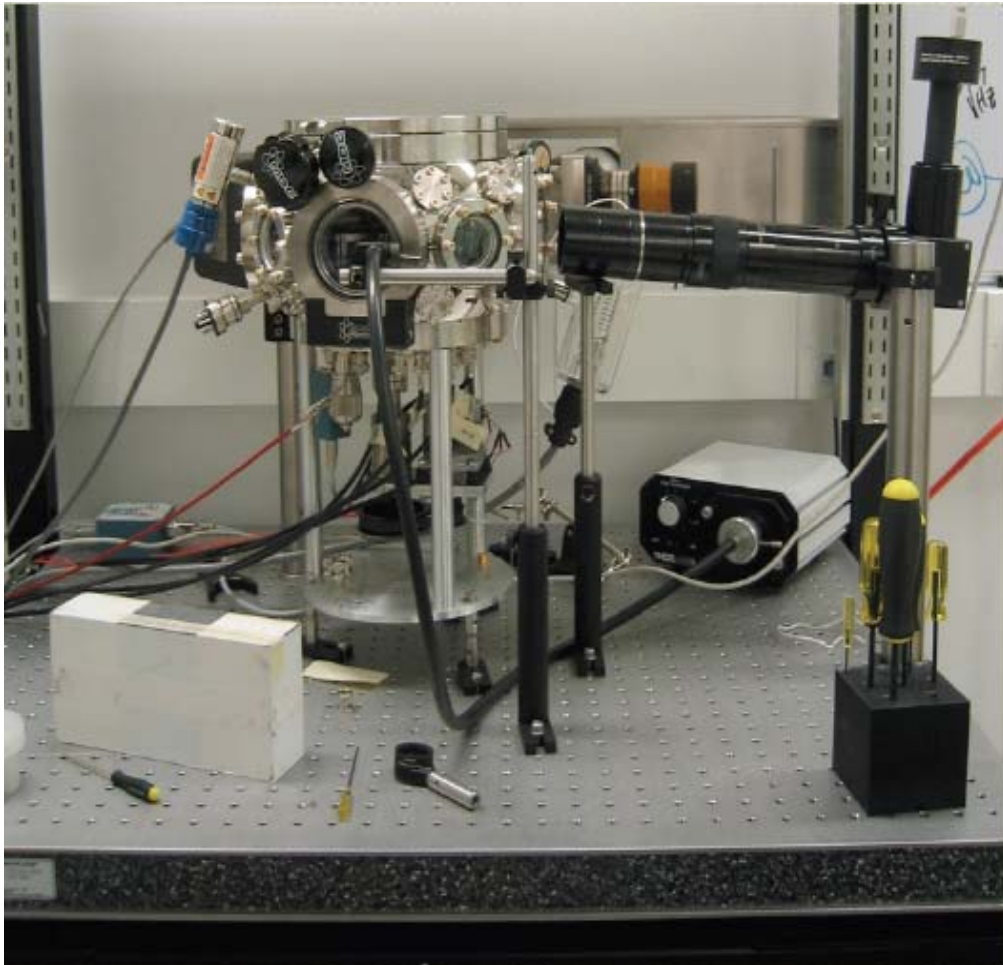


Figure 2.9 The image of STM system on vibration isolation table.

2.3 The Operation of STM

The electron tunneling only occurs when the tip is within about 10 \AA from the counterelectrode, so the gap between the electrodes must be controlled during the operation. This is usually accomplished by STM electronics, the control box SPM

100, which consist of three parts: the preamplifier, the feedback controller and the triple high voltage amplifier, as shown in Figure 2.10.

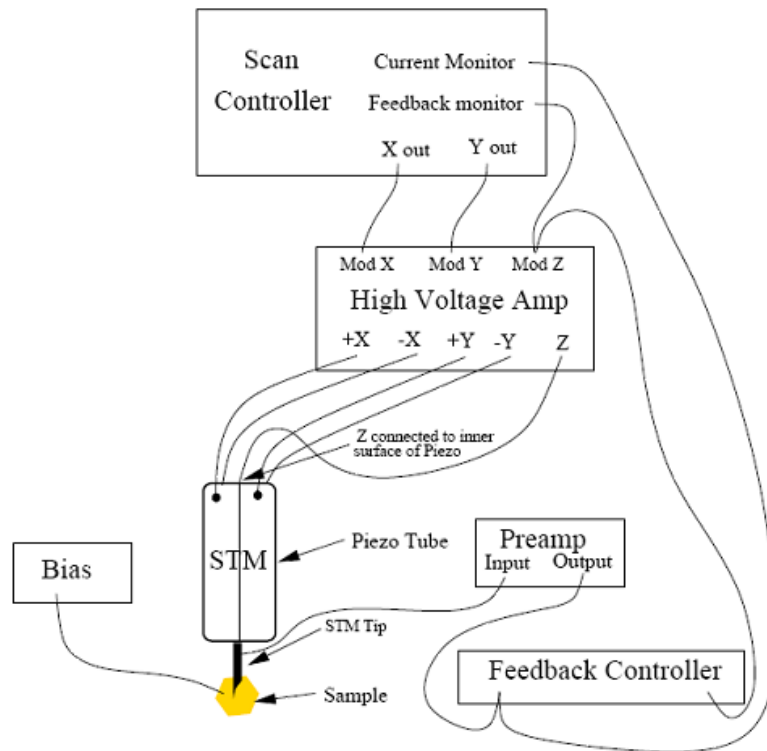


Figure 2.10 Basic element of a Scanning Tunneling Microscopy

Converting the tunneling current into a voltage to drive the feedback controller is the function of the preamplifier. The feedback loop compares the tunneling current to a setpoint and produces an error voltage proportional to the difference between these two signals. This error signal is amplified by the high voltage amplifier to drive the Z axis piezo to keep a constant average current. Thus the tip will stay a constant height over the sample. This error voltage also provides the topography information.

There are four adjustments on the feedback controller. These are the gain, time constant, DC tunneling current setpoint and DC bias voltage. The GAIN control adjusts the gain of the feedback loop and should be set as high as possible without causing oscillation in the system. The time constant adjust changes the cutoff

point of one pole lowpass filter that serves as the dominant pole of the feedback loop. DC tunneling current setpoint dial is used to set the compared tunneling current value. And DC bias voltage of the feedback controller provides the bias for the tunneling junction.

The triple amplifier is a high voltage ($\pm 130\text{V}$) amplifier used to amplify the signals from the STM electronics to a level that can drive the piezo assembly to move. The X Y and Z outputs drive the X Y and Z piezo of STM respectively. For the X and Y channel, the gain can be set in software according to the size scan desired. Also the X and Y offset dials on RHK control panel allow repositioning the scan area. For the Z channel the gain setting affects the feedback loop gain and should be set in conjugation with the feedback control gain and time constant to provide the maximum gain while maintaining loop stability.

Thus when STM is used as electron tunneling transducer for downmixing readout, these parameters, DC tunneling current, bias voltage, gain and time constant, should be carefully chosen to make the STM work stably. We will explore the impact of these parameters on STM downmixing readout in detail.

REFERENCE

1. G. Binning, H. Rohrer, C. Gerber, and E. Weiber, Surface studies by scanning tunneling microscopy, *Phys. Rev. Lett.* 49, 57, (1982)
2. G. Binning, H. Rohrer, C. Gerber, and E. Weiber, 7x7 Reconstruction on Si(111) resolved in real space, *Phys. Rev. Lett.* 50, 120, (1983)
3. Bardeen, J., Tunneling from a many-particle point of view, *Phys. Rev. Lett.*, 1961, 6, 57
4. Technical brief published at <http://www.rhk-tech.com/preamps.php>, Retrieved July, 2007.

Chapter 3 Electron Tunneling Transducer Using Signal Downmixing Readout

In this chapter, we present the configuration which we use to measure the motion of NEMS. First, we introduce the transducer based on electron tunneling. Secondly, the piezoelectric actuation which we use in our experiment will be simply explained. Then we focus on the mathematical description of tunneling junction downmixing and the details of the downmixing scheme.

3.1 The introduction of electron tunneling transducer

The investigation of the ultimate quantum limits for the detection of weak forces was originally explored in connection to the search for gravitational wave and more results have been stimulated by the development of nanoelectromechanical systems (NEMS). But for all the nanotechnology applications of NEMS devices, a significant challenge is figuring out a fast, low-noise technique for transferring small mechanical motion into reasonable electronic signals to measure. Electron tunneling is a promising method to measure the minute motion of NEMS, because the tunneling current is so sensitive to the change in distance and the fundamental limit, I_T/e , can reach the GHz. Also the transducer using electron tunneling is a nonreciprocity electromechanical transducer which has greatly reduced back action on the mechanical element being monitored and may reach the quantum limit for a measurement of the position of a mechanical oscillator even with use of a non-quantum-limited amplifier [1, 2].

Simply put the tunneling transducer is a variable resistance transducer, such as a scanning tunneling microscope (STM) tip, held close to the sample to monitor the fluctuation. The motion of a NEMS device modulates the gap of a tunnel junction between the tip and the NEMS device and thus will modulate the tunneling probability. When the junction is biased with a constant voltage, the current measured by an amplifier which follows the tunnel probe provides a sensitive

measure of the tunneling gap and therefore of the displacement of the NEMS device, as shown in Figure 1.8.

When the gap between the probe tip and NEMS device is small enough, the tunnel junction is formed and an electron can tunnel through the energy barrier from one side to the other with a finite probability based on the tunneling quantum mechanical effect. As shown in Figure 3.1 the tunneling current I through the junction is related to the dc bias voltage, V , and the tunnel gap, x , and can be written as [3]:

$$i = \rho_s(E_F) V e^{-2\kappa d} \quad (3.1)$$

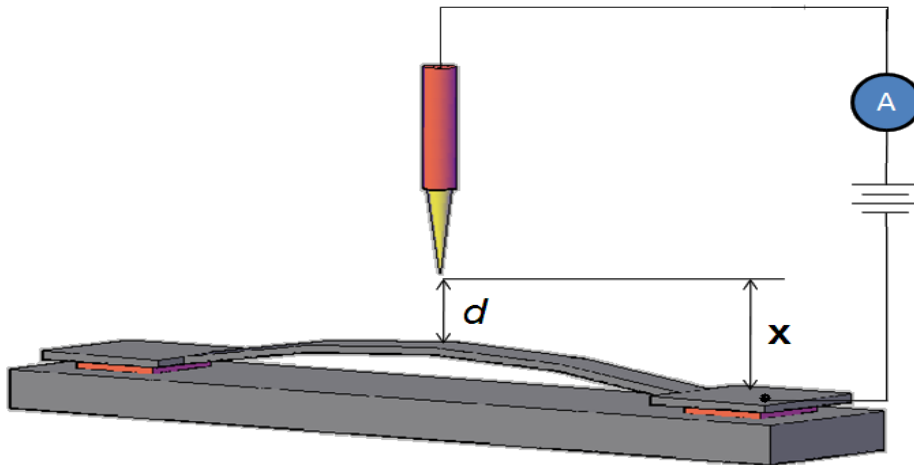


Figure 3.1 Scheme for the detection of displacement through an electron tunneling transducer. The static separation between the NEMS device and the tip is d and the displacement of the NEMS device is $(x-d)$.

Here $\rho_s(E_F)$ is the local density of electronic states in the NEMS device which can be assumed to be voltage-independent and κ is the decay constant for electron wave-function within the gap, $\kappa = \sqrt{2m_e\Phi} / \hbar$, here m_e is the mass of electron, Φ is the work function of the metal and \hbar is Planck's constant divided by 2π . The

typical value of κ is about 1.15\AA^{-1} for gold where the work function for clean gold is about 5.4eV .

Based on the exponential dependence of tunneling current on the electron tunneling gap and the decay constant $\kappa \approx 1.15\text{\AA}^{-1}$, it is clear that the tunneling transducer will be very sensitive to the motion of the sample. Let us suppose that an electronic circuit is capable of detecting 1% variation in a 1 nA current, then the distance can be calculated as following:

$$\partial d = \frac{\partial i}{2\kappa i} \approx 0.004 \text{ \AA}$$

To represent the tunneling transducer easily, we convert the various noises in the measurement into a limiting displacement floor [4]:

$$[S_x(\omega)]^{1/2} = \left(\frac{S_i^{(A)}(\omega)}{4\kappa^2 i^2} + \frac{e}{2\kappa^2 i} + \frac{S_F^{(BA)}}{m_{eff}^2 ((\omega_0^2 - \omega^2)^2 + \frac{\omega^2 \omega_0^2}{Q^2})} \right)^{1/2} \quad (3.2)$$

the first term on the right hand side represent the equivalent current noise of the current amplifier – usually in the range $S_i^{1/2} \approx 10^{-13} \text{ A Hz}^{-1/2}$ and this current noise of the current amplifier can be decreased by the design of current amplifier. The second term arises from current noise. The spectral density of the current noise is the usual expression for shot noise plus the Johnson-Nyquist noise of the tunneling current,

$$S_i = 2ei + 4k_b T / R \quad (3.3)$$

For a clean surface, the shot noise dominates the Johnson-Nyquist noise when DC bias voltage between the tip and sample $V > 2k_b T / e = 51 \text{ mV}$ at 300K. So here the John-Nyquist noise is omitted. For a typical tunneling current of 1 nA, the spectral density of shot noise is $[S_i^{(s)}]^{1/2} \approx 10^{-14} \text{ A Hz}^{-1/2}$.

The character of the backaction force noise in a tunneling transducer has been researched. The spectrum of the force fluctuations is the white noise with a spectral density given by

$$S_F^{(BA)} \approx \left(\frac{p}{e}\right)^2 2ei + (\hbar\kappa)^2 \frac{i}{e} \quad (3.4)$$

The first term is that an electron which tunnels from the probe to the mechanical oscillator carries momentum and this creates a force, $f = pi/e$, where p is the momentum of tunneling electron and i/e is the tunneling rate, on mechanical oscillator. This term is completely correlated with the shot noise current fluctuations of the transducer and the spectral density can be written as $(p/e)^2 2ei$. The second term which is independent of the shot noise is the fluctuation of the momentum current from the tip to the test mass. This arises from the intrinsic uncertainty of the momentum of each electron which tunnels. For the tunneling electron the position uncertainty is $\Delta x \approx d \approx 1/\kappa$. Then the momentum uncertainty can be written as $\Delta p \approx \hbar/\Delta x \approx \hbar\kappa$. The variance (or the fluctuation in the force) is $\Delta f \approx (\hbar\kappa) i/e$ – given that force is the temporal rate of change of impulse. The spectral density of this noise can be gotten by $(\Delta f)^2$ dividing the effective bandwidth $\Delta\omega \approx I/e$ and can be written as $(\hbar\kappa)^2 i/e$. Thus for a tunnel current about 1 nA and $\kappa \approx 1.15\text{\AA}^{-1}$, $[S_F^{(BA)}] \approx 10^{-18}\text{N}\cdot\text{Hz}^{-1/2}$.

Thus we can calculate the displacement measurement sensitivity of electron transduction based on the above the discussion. The force noise is small and here we can omit it. In our experiment the IVP-300 preamplifier is used and the current noise of the amplifier is about $10^{-14}\text{AHZ}^{-1/2}$ according to RHK preamplifier specifications. The noises come mainly come from noise current of the amplifier and the shot noise. Assuming the tunneling current 1nA and $\kappa \approx 1.15\text{\AA}^{-1}$, the displacement measurement sensitivity is about $0.43\text{fm}/\text{Hz}^{1/2}$ which is more sensitive than other displacement transductions which is introduced in Chapter 1.

From these we know that tunneling transducers can have an exquisitely low noise floor on clean surface and be sensitive to the minute motion of NEMS devices.

In addition, it is especially important to note that the displacement responsivity of the tunneling transducer is not directly dependent on the dimensions of the transducer. As a result, the tunneling transducer can be miniaturized without loss of displacement resolution. This development creates an opportunity for a broad class of sensor without loss of performance and can be used for ever smaller NEMS device detection.

3.2 Device Actuation

Inducing motion of very small structures has been demonstrated with a variety of techniques, including magnetomotive technique [5], electrostatic (capacitive) actuation technique [6], photothermal technique [7], and piezoelectric actuation technique [8]. There are also other techniques which will be used for NEMS actuation.

In our project, piezoelectric actuation was chosen to drive the resonators in their resonant mode. As we know, some materials have the ability to generate an electric potential in response to applied mechanical stress. This is called the piezoelectric effect. The piezoelectric effect is reversible and this means a piezoelectric material can convert electrical energy into a mechanical displacement or stress. One can use this effect to make piezoelectric actuator, as shown in Figure 3.2.

When the piezoelectric materials are used for actuator, the flat region of the frequency response plot, as shown the yellow area of Figure 3.3 is typically used. In this region, the relationship of the applied voltage and force is linear and can be written as:

$$F = DV \tag{3.5}$$

Here D is the electric charge density displacement which is related to the material properties and direction. In ideal situation, this region is used to actuate NEMS device. But for real piezo disc, there are several resonance frequencies. When we use the piezo disc to drive MEMS device, the flat region is chosen. Thus the actuation force coming from piezo disc is related to the voltage which is applied to the piezo disc. When an ac voltage, $V = V_{ac} \cos(\omega t)$, is applied to the piezo disc, the actuation force coming from the piezo disc can be written as:

$$F(t) = D V_{ac} \cos(\omega t) = F \cos(\omega t) \quad (3.6)$$

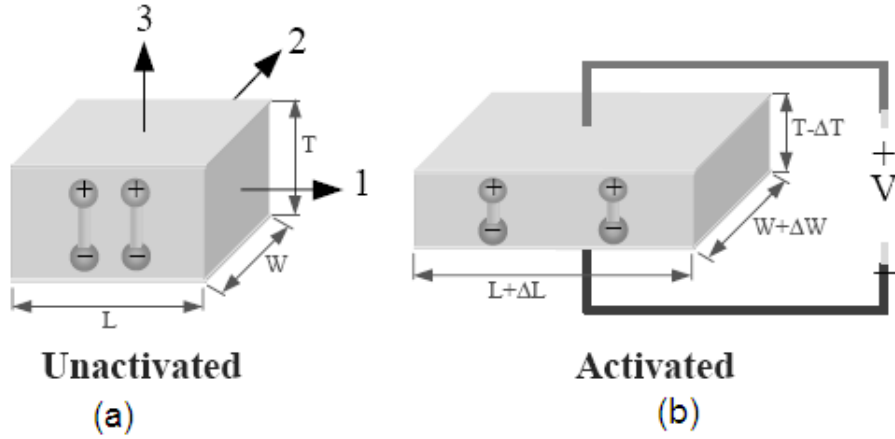


Figure 3.2 Motion of Piezoelectric Material when it is applied bias voltage. (a) Piezoelectric material is not applied bias voltage. (b) Piezoelectric material is applied bias voltage

When this force is applied to the NEMS device, it will induce the vibration of NEMS. The vibration amplitude of NEMS device can be written as:

$$a_n = \frac{1}{\rho A l^3} \frac{F(t)}{\omega_n^2 - \omega_c^2 - i\omega_n / Q} \int_0^l u_n(x) dx \quad (3.7)$$

And then we put Equation (3.6) into Equation (3.7) and get:

$$a_n = \left[\frac{1}{\rho A l^3} \frac{F}{\omega_n^2 - \omega_c^2 - i\omega_n^2 / Q} \int_0^l u_n(x) dx \right] \cos(\omega_c t) \quad (3.8)$$

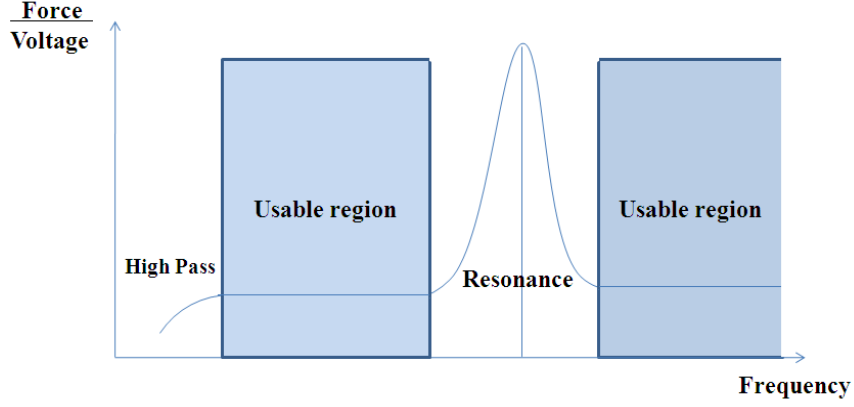


Figure 3.3 Piezoelectric material frequency responses. In usable region, the relationship between the applied voltage and the force is linear. (Imitating graph from Wikimedia Commons)

And then we put Equation (3.6) into Equation (3.7) and get:

$$a_n = \left[\frac{1}{\rho A l^3} \frac{F}{\omega_n^2 - \omega_c^2 - i\omega_n^2 / Q} \int_0^l u_n(x) dx \right] \cos(\omega_c t) \quad (3.8)$$

Here we let $a_0 = \frac{1}{\rho A l^3} \frac{F}{\omega_n^2 - \omega_c^2 - i\omega_n^2 / Q} \int_0^l u_n(x) dx$ and it depends on the material, resonance frequency and actuating force coming from piezo disc. It should be constant for one resonance mode at the constant force. Thus in order to be convenient for the following deduction, the vibration amplitude of NEMS can be written as:

$$a_n = a_0 \cos(\omega_c t) \quad (3.9)$$

This equation for the vibration amplitude of NEMS will be used in the following discussion. Its value depends on the resonant mode, material properties, actuating force and actuating force frequency.

3.3 Mathematical Description of STM Tunneling Junction Downmixing

We have presented some advantages of the electron tunneling transducer, but the useful bandwidth of tunneling transduction is limited by the stray capacitance in macroscopic wiring (discussed in an earlier chapter). In order to overcome this obstacle, a NEMS system with the electron tunneling transducer and piezoelectric actuator can be setup, as shown in the Figure 3.4. Combining the tunneling current equation (3.1) and the vibration of the piezo disc equation (3.9), the tunneling current of Figure 3.4 can be written as:

$$\begin{aligned} i &= \rho_s(E_F) V_{ac1} \cos(\omega_1 t) e^{-2\kappa(d - a_0 \cos(\omega_2 t + \Phi))} \\ \Rightarrow i &= \rho_s(E_F) V_{ac1} \cos(\omega_1 t) e^{-2\kappa d} e^{2\kappa a_0 \cos(\omega_2 t + \Phi)} \end{aligned} \quad (3.10)$$

The Taylor series for the exponential function e^x at 0 can be written as:

$$e^x = 1 + \frac{x^1}{1!} + \frac{x^2}{2!} + \frac{x^3}{3!} + \dots = 1 + x + \frac{x^2}{2} + \frac{x^3}{6} + \dots \quad (3.11)$$

Using the Taylor series to replace the exponential item of equation (3.10), we can rewrite the tunneling current as the following:

$$i = \rho_s(E_F) V_{ac1} \cos(\omega_1 t) e^{-2\kappa d} \left[1 + (2\kappa a_0 \cos(\omega_2 t + \Phi)) + \frac{(2\kappa a_0 \cos(\omega_2 t + \Phi))^2}{2} + \dots \right] \quad (3.12)$$

Because the higher power items have higher frequency information and are unuseful for our experiment, we can omit the quadratic and higher power items of equation (3.12) and get:

$$i = \rho_s(E_F) e^{-2\kappa d} V_{ac1} \cos(\omega_1 t) (1 + 2\kappa a_0 \cos(\omega_2 t + \Phi)) \quad (3.13)$$

Here one needs to use the sum and difference formulas of trigonometric functions.

$$\begin{aligned}\cos(x+y) &= \cos x \cos y - \sin x \sin y \\ \cos(x-y) &= \cos x \cos y + \sin x \sin y\end{aligned}\quad (3.14)$$

According to the equation (3.14), we can get the relationship:

$$\cos x \cos y = \frac{1}{2}(\cos(x+y) + \cos(x-y))\quad (3.15)$$

Based on the equation (3.15), the equation (3.13) can be rewritten as:

$$i = \rho_s(E_F)e^{-2\kappa d}V_{ac1}[\cos(\omega_1 t) + \kappa a_0 \cos((\omega_1 + \omega_2)t + \Phi) + \kappa a_0 \cos((\omega_1 - \omega_2)t + \Phi)]\quad (3.16)$$

From equation (3.16), one can see that the tunneling current includes three different frequency signals when we omit the quadratic or higher order terms of the equation. The frequency information of tunneling current is displayed in Figure 3.5.

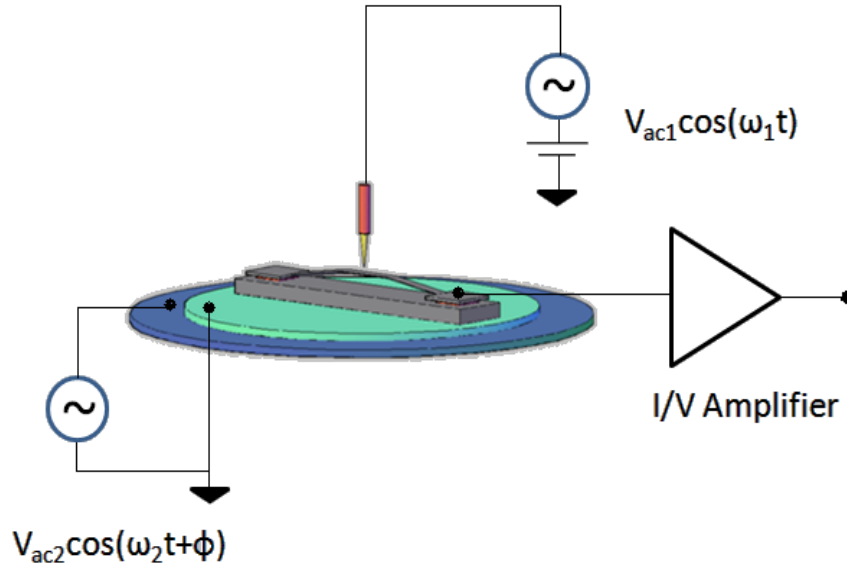


Figure 3.4 The scheme diagram of downmixing technique which integrates electron tunneling transducer and piezoelectric actuator

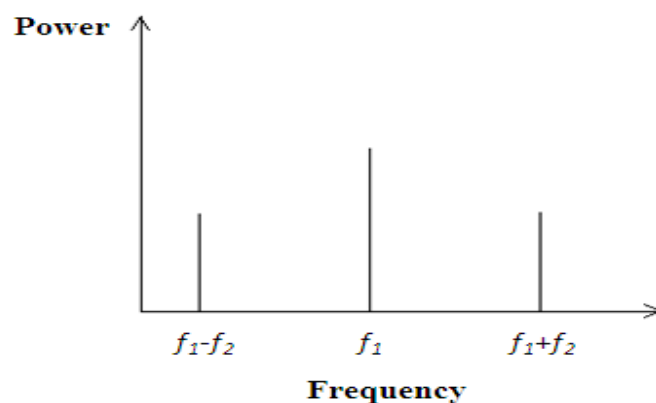


Figure 3.5 Information of the output of tunneling current in frequency domain

Thus when we have two high frequencies which are close to each other, these two high frequencies are mixed when they pass through the STM tunneling junction. As the result the difference of two high frequencies can be seen at the tunneling current output. One can easily readout the information with normal STM and improve the ability to readout high frequency information with STM. This allows an electron tunneling transducer to detect the motion of high frequency NEMS devices.

3.4 Configurations of Tunneling Junction Frequency Downmixing

In order to transfer the high frequency to low frequency to detect, we design the STM downmixing electric circuit as shown in Figure 3.6 based on the derivation of the above discussion. We will analyze this scheme in detail in this section.

In the scheme, the ac power supply is the signal generator, Agilent N9310A, which has a sweep frequency function. A sweeping frequency signal which is generated by the signal generator is sent to the power splitter to divide into two equal power and frequency signals.

One of signals is directly sent to the piezo disc. Due to reversible piezoelectric effect, a mechanical force will be created and this force will drive the NEMS device into motion. The amplitude of NEMS device vibration can be expressed as

equation (3.9). But the motion of NEMS is not necessarily in phase with the force which is created by the piezo disc due to response time and other complex factors.

The other signal is sent to the STM tip through a single sideband mixer, SSB 05-15-3K-6K, and Bias Tee. At the single sideband mixer this signal will mix with a low frequency signal which comes from the Lock-in amplifier reference output and which frequency is located within the STM bandwidth. This low frequency can be chosen as long as it retains within the STM bandwidth. Here we can choose a frequency based on the noise floor in order to improve the sensitivity of detection. At the output of the mixer, two signals are produced with 10dB power difference - one higher sideband frequency and the other lower sideband frequency, which one is the higher power be chosen. For purposes of this argument, the lower power signal can be assumed to be negligible. Then this signal will pass a bias tee to combine with a DC voltage. Here the function of bias tee is to combine the high frequency and DC without the high frequency signal reaching the DC electronic output or the DC signal loading mixer, lock-in, or ac source output. After that this combined signal is applied to the STM tip. At the tunneling junction, the two signals which are divided by the power splitter meet together. Due to the mixing function of tunneling junction, these two signals are mixed and follow the downmixing rule which is described in Equation (3.16) to create three different frequencies. And then this downmixing signal will be amplified by I/V amplifier, RHK IVP-300, and sent to the Lock in amplifier, SR 810. As we mentioned in Chapter 1, due to the stray capacitance in macroscopic wiring between the NEMS device and I/V amplifier and the high capacitance of the amplifier itself, the high frequencies will be cutoff. Thus at the output of I/V amplifier, all that remains is the low frequency information which consist of a signal precisely at the reference frequency of the Lock-in amplifier, a DC tunneling current signal, and noise. In the Lock-in Amplifier the downmixing signal will be picked out since its frequency is same as the reference signal frequency. This signal carries the information about the high frequency dynamical MEMS motion. At the same time, the feedback system maintains in constant current mode, with respect to time-averaged position of the resonator.

Now let us explore the phase information of the downmixed result in this electric scheme.

Assume that the signal from the signal generator is:

$$V = V_s \sin(\omega_s t + \theta_1) \quad (3.17)$$

and the signal from the Lock-in amplifier is:

$$V_{downmixing} = V_r \sin(\omega_r t) \quad (3.18)$$

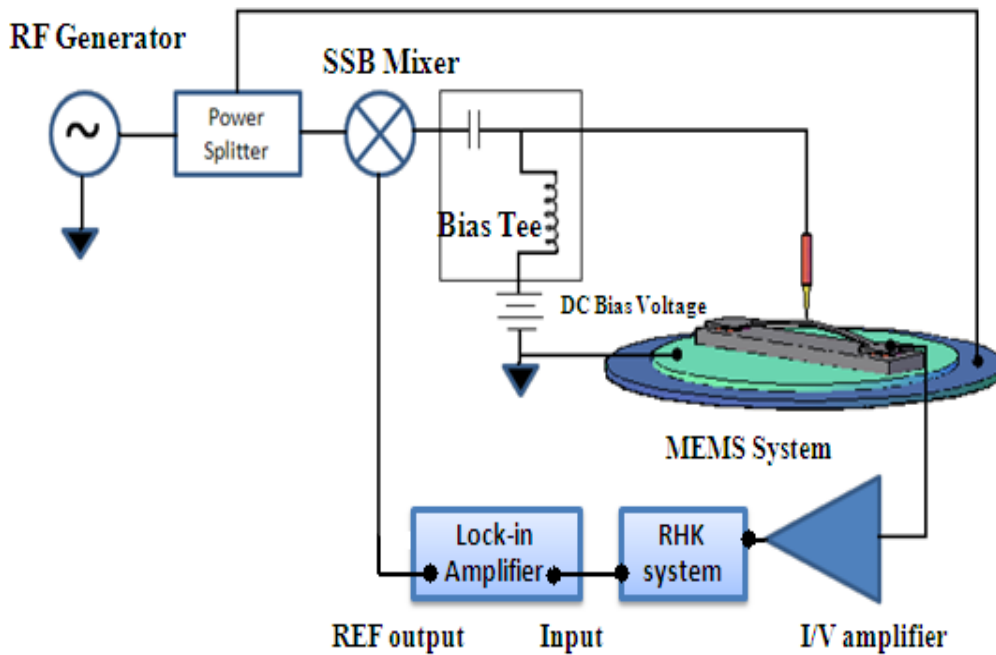


Figure 3.6 STM frequency downmixing readout scheme. The MEMS device is mounted on the piezo disk and put on the holder of the STM. Here the lock-in amplifier is SR 810 and has two functions – reference signal generator and data collection. SSB mixer is a commercial single sideband mixer which can output either higher sideband or lower sideband. I/V amplifier is a low noise IVP 300 of RHK.

Here the phase difference shown in Equation (3.17) and (3.18) is based on the lock-in amplifier, the phase difference between the signal from signal generator and the signal from lock-in amplifier is assumed θ_1 . When the single sideband mixer is used and we choose the higher sideband, the output of the mixer can be written as:

$$V_{output} = -\frac{1}{2}V_s * V_r \cos[(\omega_r + \omega_s)t + \theta_1] \quad (3.19)$$

When the piezo disc actuates the MEMS, the motion of NEMS is not necessarily in phase with the force due to response time and other complex factors. We can set this phase difference to be θ_2 . Thus based on Equation (3.9), the vibration of MEMS can be written as:

$$d_{MEMS} = a_n = a_0 \sin(\omega_s t + \theta_1 + \theta_2) \quad (3.20)$$

Here $a_0 = \frac{1}{\rho A l^3} \frac{F_{ext}}{\omega_n^2 - \omega_c^2 - i\omega_n^2 / Q} \int_0^l u_n(x) dx$ is the amplitude of

NEMS at actuating force F_{ext} and F_{ext} is related to the voltage applied to piezo disc.

For STM, when the bias voltage is far less than the tunnel barrier height of the metal the tunneling current can be written as:

$$\begin{aligned} I &\propto (V_{bias} + V(\omega)) e^{-2\kappa(d+d_{MEMS})} \\ \Rightarrow I &\propto (V_{bias} + V(\omega)) e^{-2\kappa d} e^{-2\kappa d_{MEMS}} \\ \Rightarrow I &\propto (V_{bias} - \frac{1}{2}V_s * V_r \cos[(\omega_r + \omega_s)t + \theta_1]) e^{-2\kappa(d+d_{MEMS})} \end{aligned} \quad (3.21)$$

Here the decay constant of electron wave-function $\kappa = 0.51 * \sqrt{\phi(eV)} \text{ \AA}^{-1}$. For clean gold surface $\kappa_{Au} = 1.185 \text{ \AA}^{-1}$.

Use Taylor:

$$e^x = 1 + x + \frac{1}{2!}x^2 + \frac{1}{3!}x^3 + \dots$$

$$\sin \alpha \cos \beta = \frac{1}{2}[\sin(\alpha + \beta) + \sin(\alpha - \beta)]$$

$$\sin \alpha \sin \beta = -\frac{1}{2}[\cos(\alpha + \beta) - \cos(\alpha - \beta)]$$

$$I \propto (V_{bias} - \frac{1}{2}V_s V_r \cos[(\omega_s + \omega_r)t + \theta_1])e^{-2\kappa d} [1 - 2\kappa a_m \sin(\omega_s t + \theta_1 + \theta_2) + \dots] \quad (3.22)$$

When we omit high frequency terms and just keep reference frequency items, we obtain:

$$I \propto V_{bias} e^{-2\kappa d} + V_s V_r e^{-2\kappa d} \kappa a_m \sin(\omega_r t - \theta_2) \quad (3.23)$$

Thus, when we use lock-in amplifier to measure tunneling current of STM, we can get the amplitude of NEMS motion and the phase information of NEMS motion which is related to initial condition θ_2 . For harmonic vibrations, the phase sweeps through 180 degree across the resonance. This phase change can also be measured with the STM downmixing readout method.

REFERENCES

1. Bocko, M. F., and Stephenson K. A., Vacuum Tunneling Probe: A Nonreciprocal, Reduced-Back-Action Transducer, *Phys. Rev. Lett.*, 61, 726, (1988)
2. Bocko, M. F., and Stephenson K. A., Tunneling transducers: Quantum limited displacement monitors at the nanometer scale, *J. Vac. Sci. B*, 9, 1363, (1990)
3. Tersoff, J., Scanning Probe Microscopy and Spectroscopy (Ed.: Bonnell, D.), Wiley, New York, 2000
4. Ekinici, K. L., Electromechanical Transducers at the Nanoscale: Actuation and Sensing of Motion in Nanoelectromechanical Systems (NEMS), *Small*, 8, 786, (2005)
5. Cleland, A. N., and Roukes, M. L., Fabrication of high frequency nanometer scale mechanical resonators from bulk Si crystal, *Appl. Phys. Lett.*, 69, 2653, (1996)
6. Tilmans, H. A., and Legtenberg, R., Electrostatically driven vacuum-encapsulated polysilicon resonators, *Sens. Actuators A*, 45, 67, (1994)
7. Koenig, D. R., Metzger, C., Camerer, S. and Kotthaus, J. P., Non-linear operation of nanomechanical systems combining photothermal excitation and magneto-motive detection, *Nanotechnology*, 17, 5260, (2006)
8. Masmanidis, S. C., Karabalin, R. B., Valminck, I. D., Borghs, G., Freeman, M. R and Roukes, M. L., Multifunctional Nanomechanical Systems via Tunably Coupled Piezoelectric Actuation, *Science*, 317, 780, (2007)

Chapter 4 STM Downmixing Readout of MEMS Motions

We measure the motion of a MEMS device with tunneling junction downmixing which is described in chapter 3. In order to make sure that the method of tunneling junction downmixing works well, we compare the results that we measured using STM downmixing with the simulation using COMSOL and the result using optical interferometry [1] for the same device. At the last part of this chapter, we explore some parameters that impact STM downmixing result and the displacement measurement sensitivity with STM downmixing method.

4.1. The MEMS Sample Setup

In our experiment MEMS size devices were chosen solely for ease of telescopic optical alignment of the tunneling tip on the top of individual device structures. The individual structures are silicon doubly-clamped beam and are fabricated with the top-down approach process flow which is described in Chapter 1.5. These doubly-clamped beams have same width, $100\ \mu\text{m}$, the thickness, $5\ \mu\text{m}$ and different length from $500\ \mu\text{m}$ to $2000\ \mu\text{m}$ with $150\ \mu\text{m}$ steps. The schematic of the device is shown in Figure 4.1.

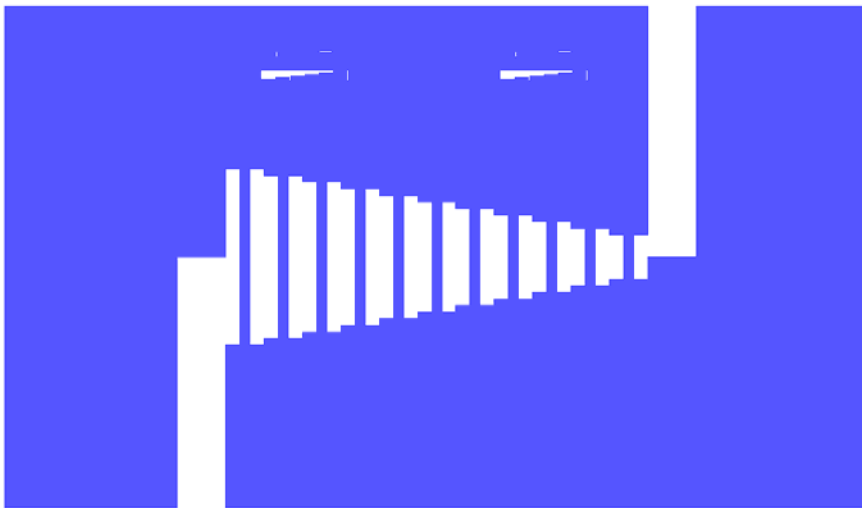


Figure 4.1 Schematic diagram of the doubly-clamped beams whose length from $500\ \mu\text{m}$ to $2000\ \mu\text{m}$, width $100\ \mu\text{m}$ and thickness $5\ \mu\text{m}$

This doubly-clamped beam chip is mounted on a commercial piezo disc which is used as an actuator to drive the doubly-clamped beam during the measurement. The piezo disc and chip are bonded to a special designed printed circuit board (PCB). After these some wire bonding and soldering are required to connect different components together. In particular, the top surface of the piezo disc is grounded to try to minimize electrical cross-talk reaching the chip, while the bottom surface is excited with RF. The tunneling current that leaves the STM tip will travel through the Au surface on the MEMS beams, down the parallel wire bonds to the PCB trace, and be controlled as the tunneling signal. The final sample is shown in Figure 4.2.

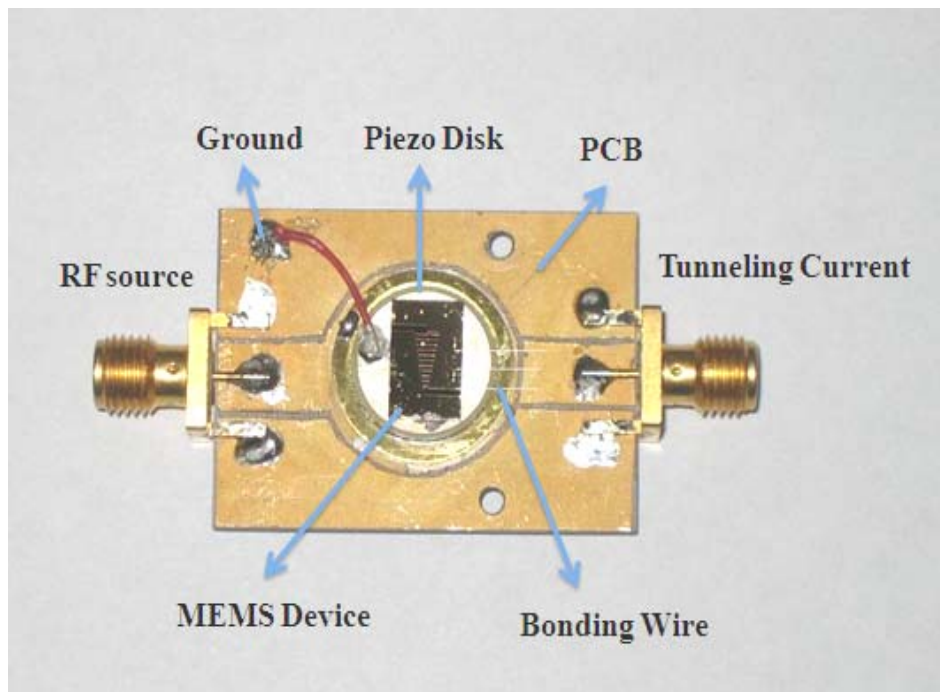


Figure 4.2 The sample of STM downmixing readout technique. Here the MEMS device and the piezo disk which is used to actuate the MEMS device are mounted on the PCB together. The PCB has four mounting holes which are used to mount the PCB to the sample holder and two terminals – RF source terminal which is used to apply voltage to piezo disk and the output terminal which output the tunneling current to the I/V amplifier

This sample is mounted to the sample holder of the STM and put into the vacuum chamber which was introduced in Chapter 2. During measurement the chamber is pumped down to less than 10^{-6} torr.

4.2. The Proof of STM Tunneling Junction Downmixing

Since it is a new method that uses STM as a transducer and frequency downmixing in tunneling junction to readout the motion of MEMS, it requires validation. In order to validate that the STM downmixing is working well, we set up the electric circuits as shown in Figure 3.6 to measure a 500 μm long, 100 μm wide, and 5 μm thick doubly-clamped beam.

The signal generator sends a sine function signal at +13dBm power which sweeps the frequency around the doubly-clamped beam resonance frequency. From the reference output of the lock-in amplifier a 4.5 kHz sin function signal is sent with 0.35 V_{rms} . Here we choose the 4.5 kHz signal based on two reasons: one is that the bandwidth of the I/V amplifier, IVP-300, is 5 kHz. Another reason is that this frequency area has a lower noise compared to other areas as shown from Figure 2.7 (b). And then we use the spectrum analyzer feature of RHK system software to observe spectral content of the output tunneling current of the STM in order to identify frequency downmixed information.

Figure 4.3 shows the information of downmixed tunneling current of the STM using the electric scheme of Figure 3.6. From RHK system software spectrum analyzer output figures, we can see that the reference frequency amplitude changes as the MEMS device actuating frequency changes. Figure 4.3 (a) shows the downmixed tunneling current FFT far from the resonance frequency of the MEMS device. The downmixed tunneling current amplitude at the reference frequency (4.5 kHz) is very small and is close to the noise floor, so we hardly see it. When we make the frequency of signal generator close to the resonance frequency of the MEMS device, the downmixed tunneling current FFT is shown in Figure 4.3 (b), (c) and (d). From these figures we can see that the amplitude at the reference frequency increases substantially with the sweep frequency close to

the resonance frequency. In particular, Figure 4.3 (c) shows the FFT when the drive frequency is closest to the MEMS mechanical resonance frequency. Here, the vibration amplitude is maximum and this causes the downmixed tunneling current to be maximum and largest amplitude at the reference frequency. This shows that the STM downmixing is working well and coinciding with the theory prediction, because the vibration amplitude becomes largest at the resonance frequency of the NEMS device and this causes the gap between the tip of the STM and the surface of NEMS to decrease and the tunneling current to increase.

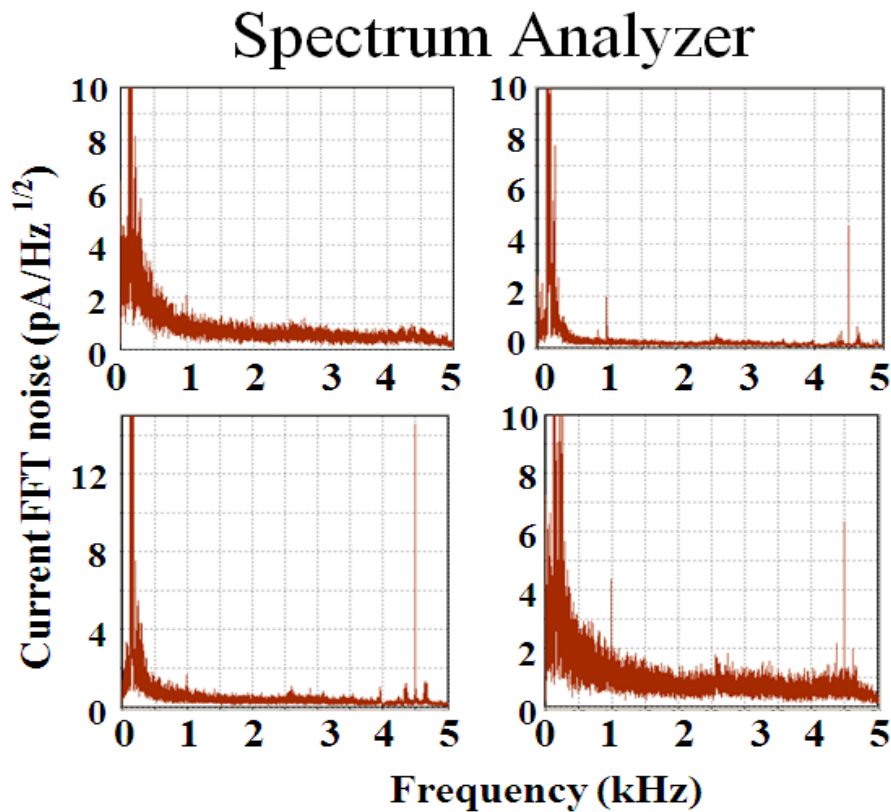


Figure 4.3 The downmixing tunneling current information for different actuating frequencies. (a) Drive frequencies are far from sample resonance frequency. (b) Drive frequencies go close to the sample resonance frequency. (c) Drive frequencies closest to the mechanical resonance frequency. (d) Drive frequencies go away from the sample resonance frequency

Figure 4.4 shows the current FFT information of spectrum analyzer when the drive frequency is close to the mechanical resonance frequency. Here we can see that there are some sidebands around the reference frequency, as shown in Figure 4.4 (b). These sidebands are the results that electrical and mechanical noises (as shown in Figure 4.4 (b)) mix with the reference frequency in tunneling junction. These also prove the mixing function of tunneling junction.

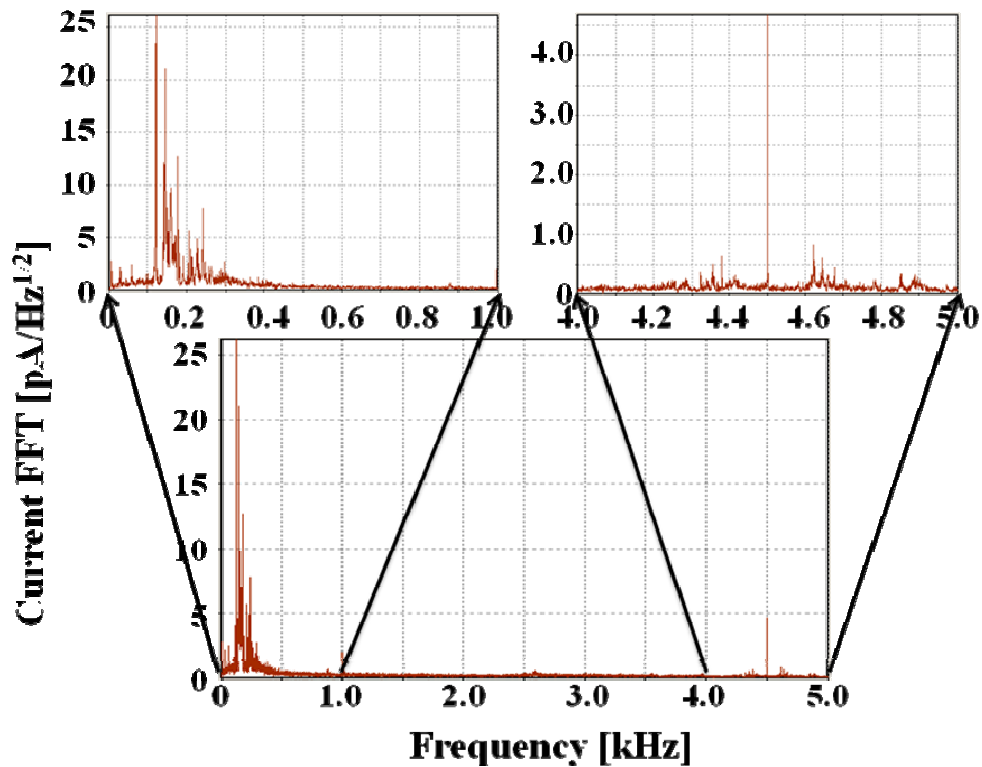


Figure 4.4 The downmixed tunneling current sideband information.
 Inset graph: Electrical and mechanical noise current FFT (left)
 Reference frequency with sidebands current FFT (right)

Thus we can utilize this method to measure the downmixed tunneling current of reference frequency and get the high frequency information about NEMS vibration. The limit of STM bandwidth is overcome and this makes possible electron tunneling transduction as the detection of MEMS motion, even NEMS motion.

4.3. The Result of STM Downmixing Readout

In order to further validate the STM downmixing readout of electron tunneling transduction, we use the COMSOL software to simulate the eigenfrequency of the doubly-clamped beam and utilize optical interferometry to prove these eigenfrequencies. We then measure the same device with STM downmixing method and compare the results with the simulation and optical interferometry measurement.

4.3.1 Simulation Result of the Doubly-clamped Beam

COMSOL as a finite element simulation software can be used to simulate well the MEMS device. Here we use COMSOL to simulate the eigenfrequency of our double layer doubly-clamped beam. During our simulation the double layers and undercut which is caused by the wet etching are taken into account. The results of eigenfrequency simulation for a 500 μm long, 100 μm wide and 5 μm thick doubly-clamped beam with double layers - Cr 20 nm and Au 200 nm - and undercut is shown in Table 4.1 and the Figure 4.5 shows the mode shape of COMSOL simulation.

Table 4.1 COMSOL Simulation Result for a long 500 μm , wide 100 μm and thick 5 μm Silicon Doubly-clamped Beam with Au and Cr Metal Layers

Vibration Mode	First Flexural Mode	Second Flexural Mode	First Torsion Mode	Third Flexural Mode	Second Torsion Mode	Forth Flexural Mode
Resonance Frequency (kHz)	112.801	305.867	447.971	589.216	909.188	954.073
Error (kHz)	1.128	3.059	2.240	1.630	4.546	2.385

* Errors come from the estimate of undercut of the beam with 0.5% error at the length and width.

The simulation results in Table 4.1 and Figure 4.5 basically show the motion of the sample which will be measured with STM downmixing technique. The vibration of our MEMS devices includes normal flexural vibration and torsional vibration.

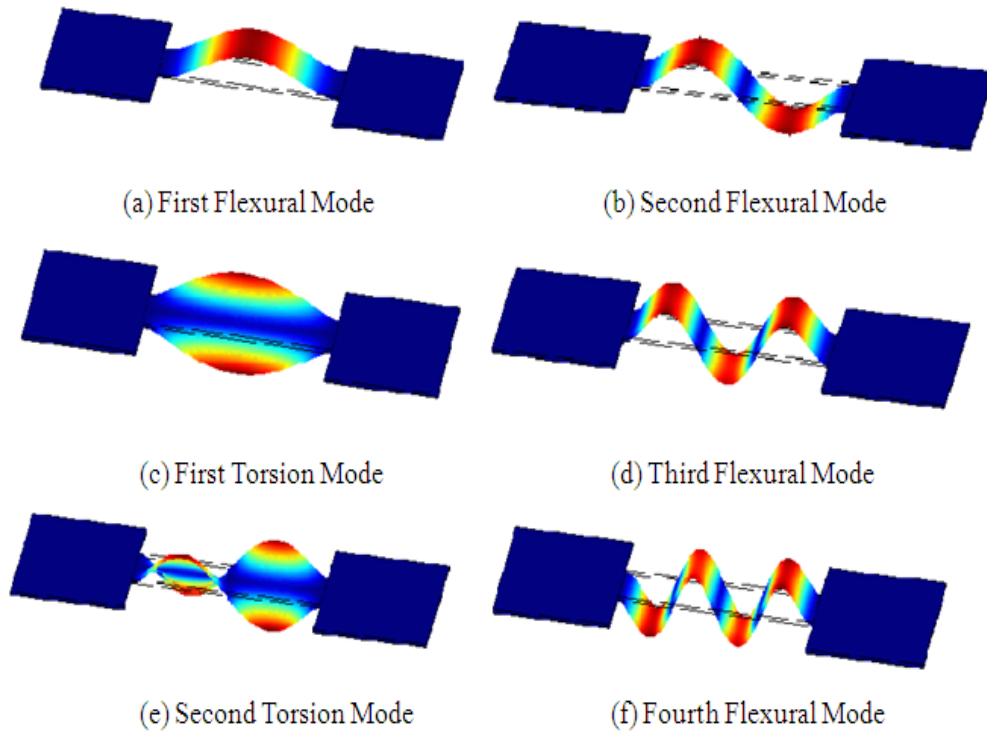


Figure 4.5 COMSOL simulation of beam mode shapes (Color indicates displacement from equilibrium position with minimum displacement at the ends of the beam)

4.3.2 Measurement Result of Optical Interferometry

Through the COMSOL simulation, we have acquired the motion information of our MEMS sample. In order to prove that these eigenfrequencies are measurable, we use optical interferometry technique [1], as shown in Figure 4.6 to measure the vibration information of a nominally identical MEMS device which was measured with STM downmixing technique. The measured response amplitude and phase as a function of drive frequency for the first six modes of COMSOL simulation are

shown in Figure 4.7 and the results are listed in Table 4.2. These measurements are done at -5dBm actuating power.

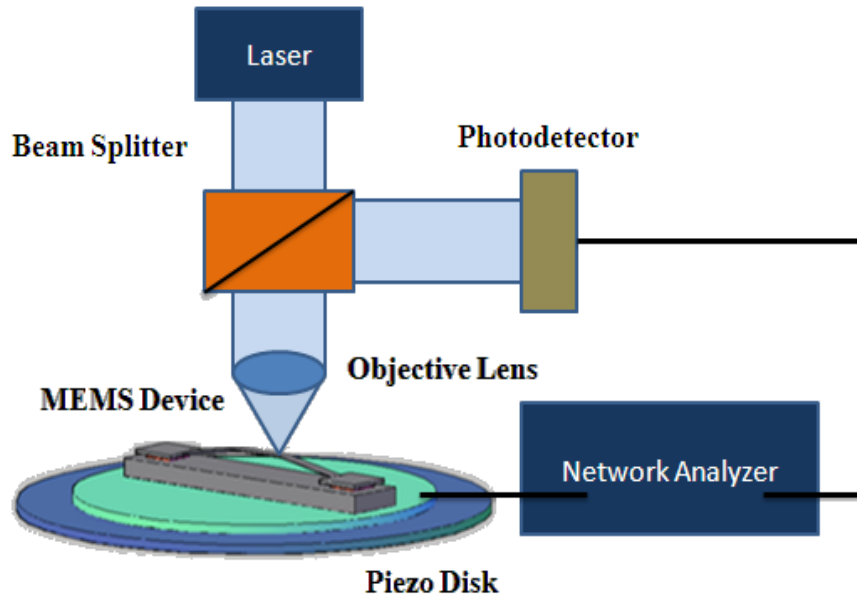
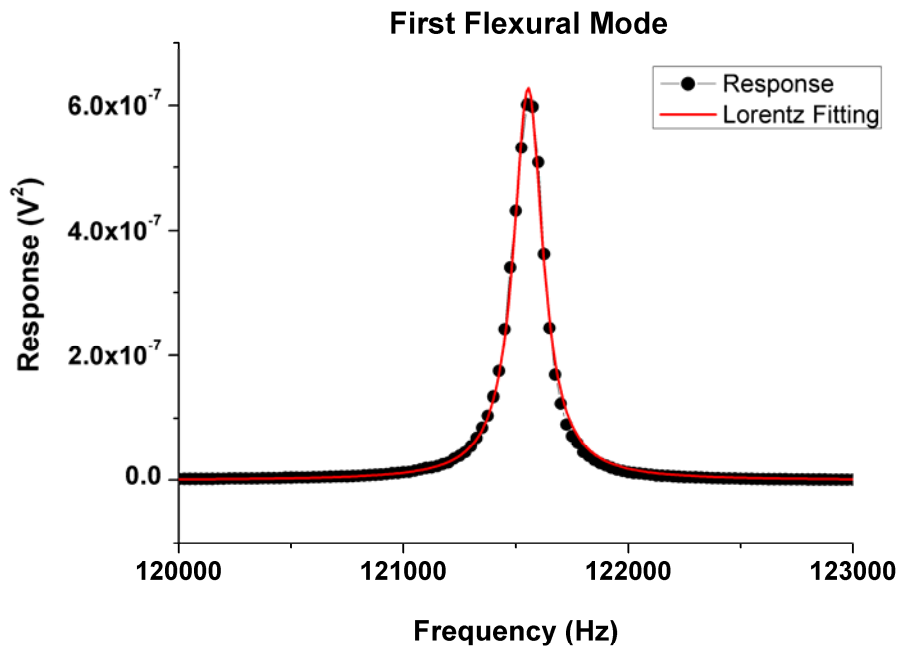


Figure 4.6 Schematic diagram of optical interferometry techniques

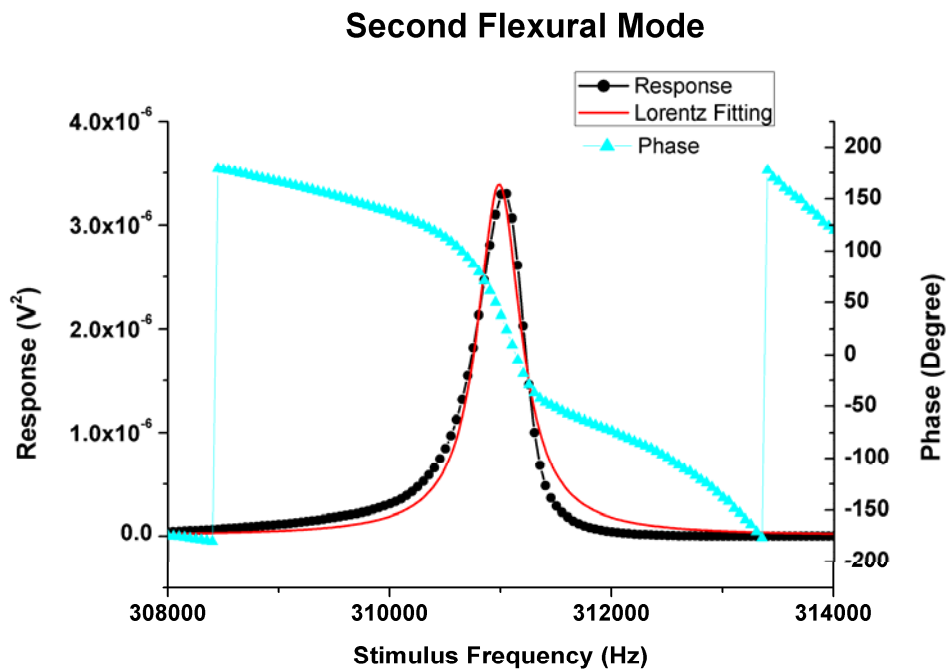
Table 4.2 Optical interferometry measurement results for a 500 μm long, 100 μm wide and 5 μm thick Silicon Doubly-clamped Beam with Au and Cr Metal Layers

Vibration Mode	First Flexural Mode	Second Flexural Mode	First Torsion Mode	Third Flexural Mode	Second Torsion Mode	Fourth Flexural Mode
Resonance Frequency (kHz)	121.554	310.982	425.921	587.658	832.837	958.476
Error (Hz)	1	3	3	3	1	1
Q factor	769	655	1571	750	8766	610

* Errors in the table come from the Lorentz fitting of measured data

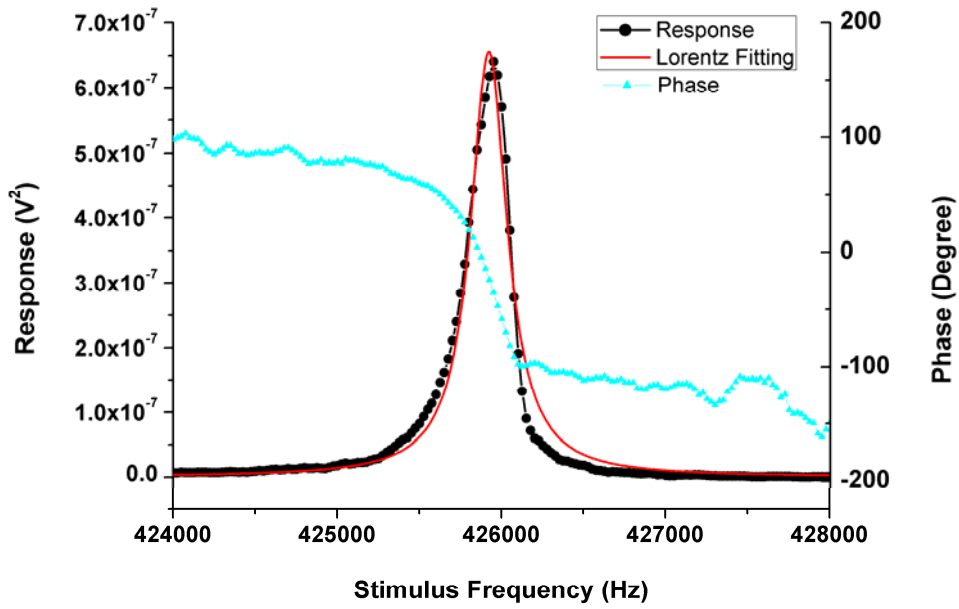


(a)



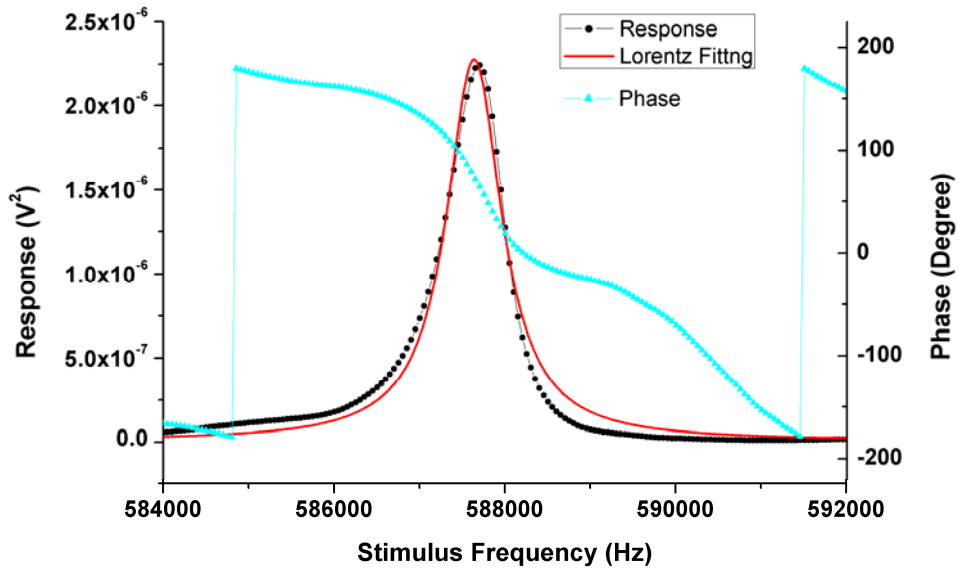
(b)

First Torsion Mode



(c)

Third Flexural Mode



(d)

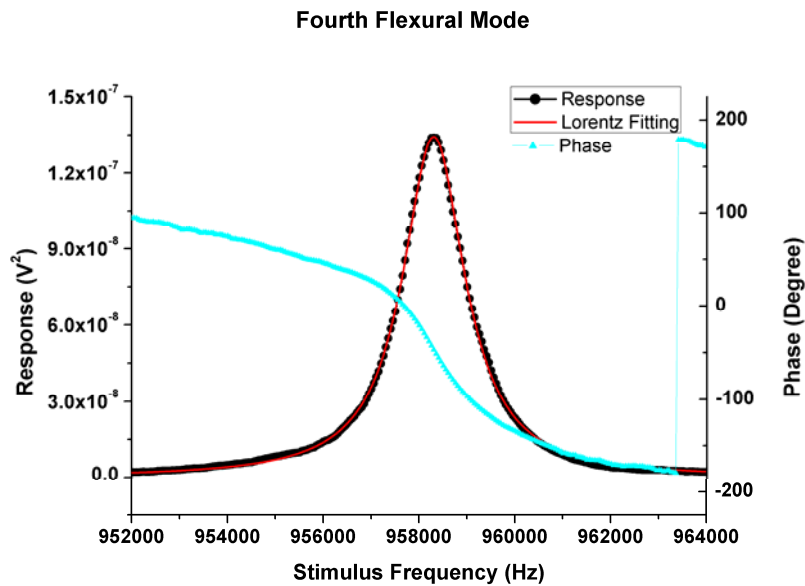
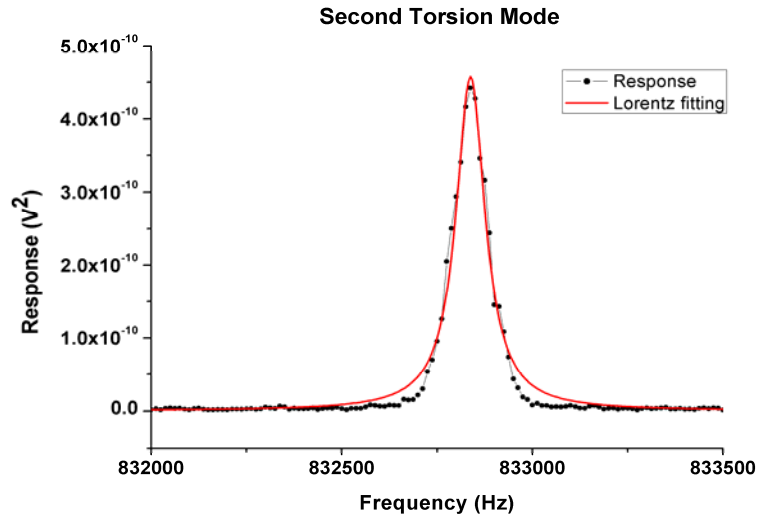


Figure 4.7 Optical interferometry measured results. The graphs show amplitude square (black line) and phase (cyan line) as a function of drive frequency. The red line shows the Lorentz fitting for the amplitude of MEMS device. Here (a) and (e) were measured with spectrum analyzer at actuating power -5 dBm. (b) (c) (d) and (f) were measure with network analyzer at actuating power 0 dBm.

The results which are measured with optical interferometry technique are similar to the COMSOL simulation results. For Figure 4.7 (a) and (e), there is no phase information about the resonance frequency, because we use spectrum analyzer to measure them. This proves that the COMSOL simulation motion of MEMS device is measurable.

4.3.3 The Result of Scanning Tunneling Microscopy Downmixing Readout

In chapter 3, we have talked in detail about the downmixing theory and derived the result of downmixing using math methods. Also in section 4.1, we used RHK software spectrum analyzer to prove scanning tunneling microscopy (STM) downmixing works well. Now we take advantage of this technique to measure the MEMS sample which we have simulated with COMSOL and measured with optical interferometry.

The electric circuit is shown in Figure 3.6. We use a Labview program, described in Appendix A, to control the signal generator providing the frequency sweep and readout the downmixed result from a lock-in amplifier. Here when two sine function signals are separately sent from the signal generator and lock-in amplifier reference output, the prediction of X readout in lock-in amplifier should be similar to the Figure 4.8 (a). The vibration amplitude may be complex, so that the motion is not necessarily in phase with the actuating force. The Figure 4.8 (b) and (c) display two results we measured in our experiment. These results are measured at the following conditions: the DC bias voltage is 0.5V, the AC bias voltage is $0.1V_{\text{rms}}$, the DC tunneling current is 0.2nA, and the actuating power of piezo disk is -11dBm. From the results we can see the output curves are different due the initial point phase difference. In order to avoid this problem and make the result convenient to process, we choose the R readout of the lock-in amplifier as the result of STM downmixing method. From the equation (3.23),

$$i \propto V_{bias} e^{-2\kappa d} + V_s V_r e^{-2\kappa d} \kappa a_n \sin(\omega_r t - \theta_2) \quad (4.1)$$

The R output of lock-in amplifier response is the part $V_s V_r e^{-2\kappa d} \kappa a_n$ which is directly related to the vibration amplitude of MEMS devices (a_n) and is determined by the initial condition of STM. Thus we can use R of Lock-in amplifier to measure the vibration information of MEMS devices and the θ of Lock-in amplifier to measure phase information, respectively.

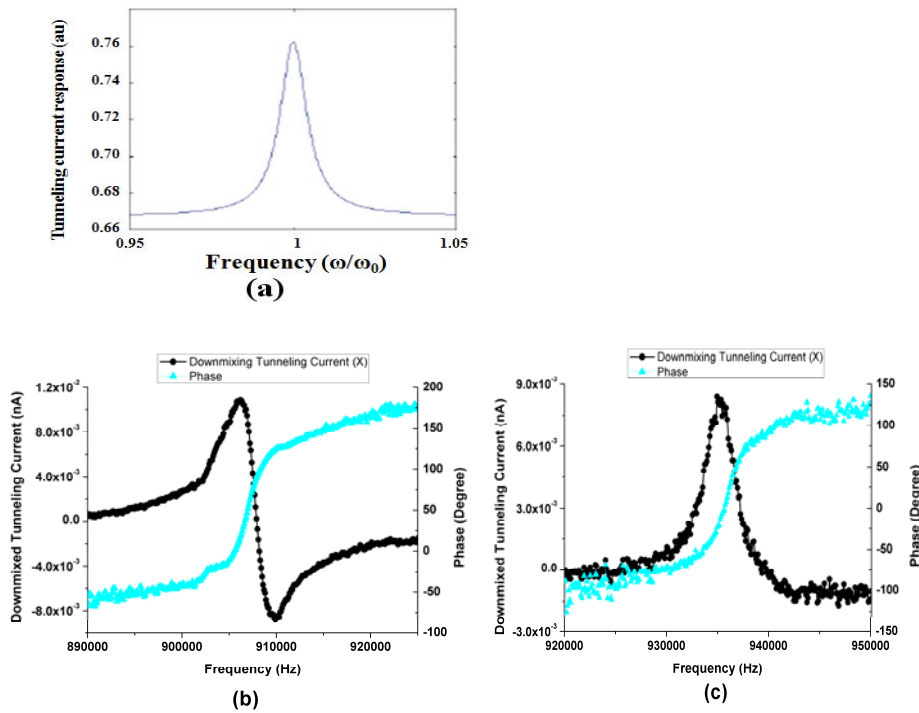


Figure 4.8 The readout Result of STM downmixing technique. (a) Downmixed tunneling response prediction with simulation. (b) The measured result with phase change from 0 to 180 degree (c) The measured result with phase change from -90 degree to 90 degree. The results of STM downmixing technique are measured at the following conditions: DC bias voltage 0.5 V, AC bias voltage is 0.1 V_{rms}, DC tunneling current 0.2 nA and the actuating power of piezo disk is -11 dBm.

Due to the limitation of our single sideband mixer whose frequency range operates from 0.5 MHz to 15MHz, it is difficult to measure lower order MEMS modes below 0.5MHz in frequency. Although there is some attenuation for

frequency which is lower 0.5MHz, we try to measure the first torsion mode whose resonance frequency is around 450 kHz and get a nice result. When we use single sideband mixer, the initial experimental condition is set as: the piezo disk actuating power -11 dBm (22 dBm attenuator is connected between the power splitter and piezo disk), DC tunneling current on the tunneling junction of 0.2nA, DC bias voltage on the tunneling junction of 0.5 V which directly comes from RHK control system and AC bias voltage on the tunneling junction of 0.1 V_{rms} which is provided by the single-side band mixer.

With this condition we measure the vibration information for the various modes around the center area except for the third flexural mode which we measure at position 1000 (where the entire MEMS length runs from position zero to position 1700). For the lower frequency fundamental flexural vibration, we are forced to use a different electronic circuit which is similar to the STM downmixing circuits shown in Figure 3.6. In this diagram, the single-side band mixer is replaced with a normal mixer whose output gives the higher side band and lower side-band with the same amplitude at the same time. This means that we can't properly monitor the phase information of the downmixed tunneling current. Appendix B contains the detailed derivation of the output with a normal mixer. Additionally for the fundamental mode, we position the tip very close to the end of the beam (near the clamping point). This is necessary both to have a small enough displacement such that the tunneling regime is not overwhelmed and since the tip-sample forces have much less of an effect at this position. The experimental condition is set as: the piezo disk actuating power -20dBm, DC tunneling current on the tunneling junction of 0.2nA, DC bias voltage on the tunneling junction of 0.4V and AC bias voltage on the tunneling junction of 0.1V_{rms}. With this condition, we measure the fundamental vibration of the MEMS beam.

When the Lock-in amplifier is used to measure the downmixed tunneling current, the first term of the tunneling current which is expressed in Equation (4.1) is ignored due to the function of the Lock-in amplifier. Thus the downmixed tunneling current can be written as:

$$i_{downmixed} \propto \frac{1}{2} V_s V_r e^{-2\kappa d} \kappa a_n \sin(\omega_r t - \theta_2) \quad (4.2)$$

As stated above, we measure the R output of the Lock-in amplifier as motion information and which can be expressed as:

$$i_{downmixed} \propto V_s V_r e^{-2\kappa d} \kappa a_n$$

$$i_{downmixed} \propto \frac{V_s V_r \kappa F_0}{\rho A l^3} \int_0^l u_n(x) dx \frac{1}{\omega_n^2 - \omega_c^2 - i\omega_n^2 / Q} \quad (4.3)$$

Let $A = \frac{-\rho_s(E_F) V_{ac1} \kappa F_0}{\rho A l^3} \int_0^l u_n(x) dx$, these factors are decided by the beam characteristics, vibration mode of the beam, the piezo disc characteristics and the STM initial condition. For a MEMS device, the A is constant versus frequency change. Therefore:

$$i_{downmixed} \propto \frac{A}{\omega_n^2 - \omega_c^2 - i\omega_n^2 / Q}$$

$$|i_{downmixed}| \propto \frac{|A|}{4\pi^2 \sqrt{(f_n^2 - f_c^2)^2 + (f_n^2 / Q)^2}} \quad (4.4)$$

To extract the resonance frequency f_n , we fit the measured downmixed tunneling current with the equation (4.4). The detected results of STM downmixing method are listed in Table 4.3. In Figure 4.9, we show the data from the STM downmixed readout method for the first six vibration modes. Even higher vibration modes are also measured and are shown in Appendix C.

In table 4.4, we listed the results using three methods: COMSOL simulation, optical interferometry measurement and STM downmixing technique. From this table, we can see that the resonance frequencies measured with STM downmixing are slightly different than those measured with optical interferometry or simulated with COMSOL. The reason is because an interaction potential between the Pt-Ir tip and gold surface modifies the resonance frequencies [2, 3]. We will talk about this interaction more in the following section where the parameters which impact the results of STM downmixing readout are discussed.

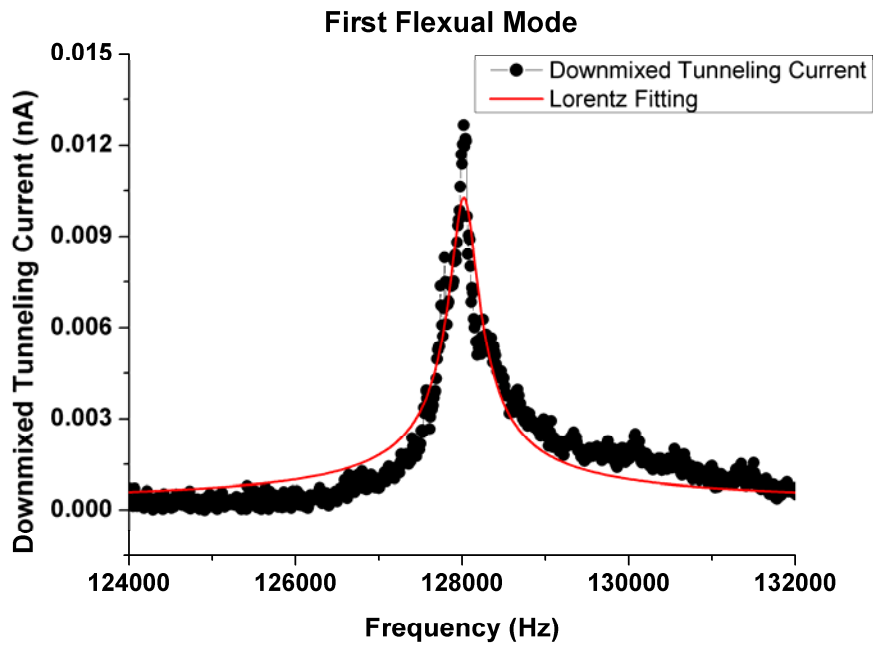
Table 4.3 STM Downmixing Measurement Result for a 500 μm long, 100 μm wide and 5 μm thick Silicon Doubly-clamped Beam with Au and Cr Metal Layers at DC tunneling current 0.2 nA, DC bias voltage 0.5 V, AC bias voltage 0.1 V_{rms} and piezo disk actuating power -11 dBm

Vibration Mode	First Flexural Mode	First Torsion Mode	Third Flexural Mode	Second Torsion Mode	Fourth Flexural Mode
Resonance Frequency (KHz)	128.021	442.465	558.481	881.521	985.461
Error (Hz)	8	22	17	103	16
Q-factor	381	892	400	1413	332

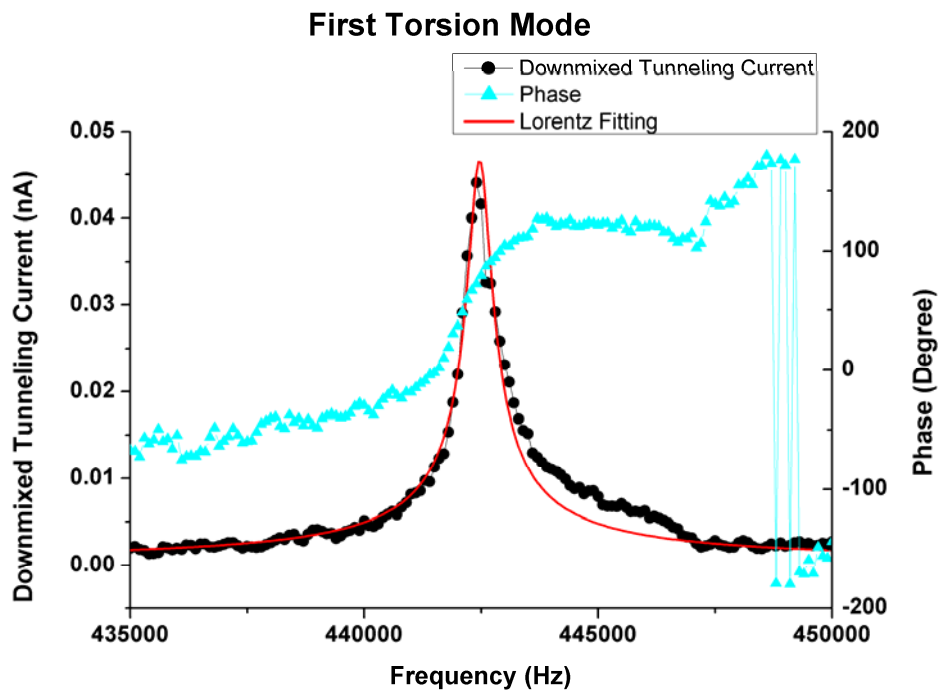
* Errors in the table come from the Lorentz fitting of measurement data

Table 4.4: The resonance frequency information using different techniques for a 500 μm long, 100 μm wide and 5 μm thick Silicon Doubly-clamped Beam with Au and Cr Metal Layers

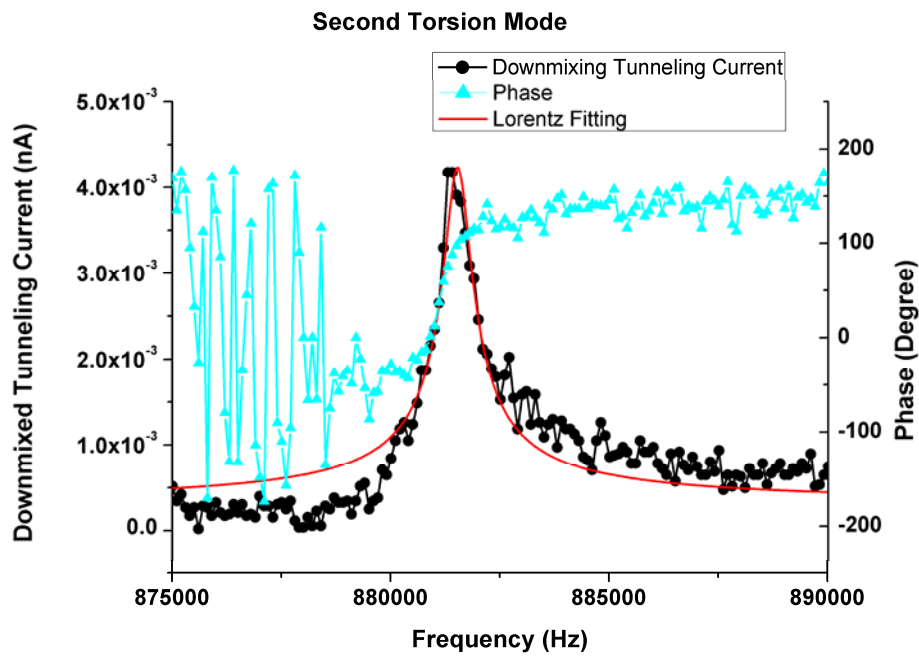
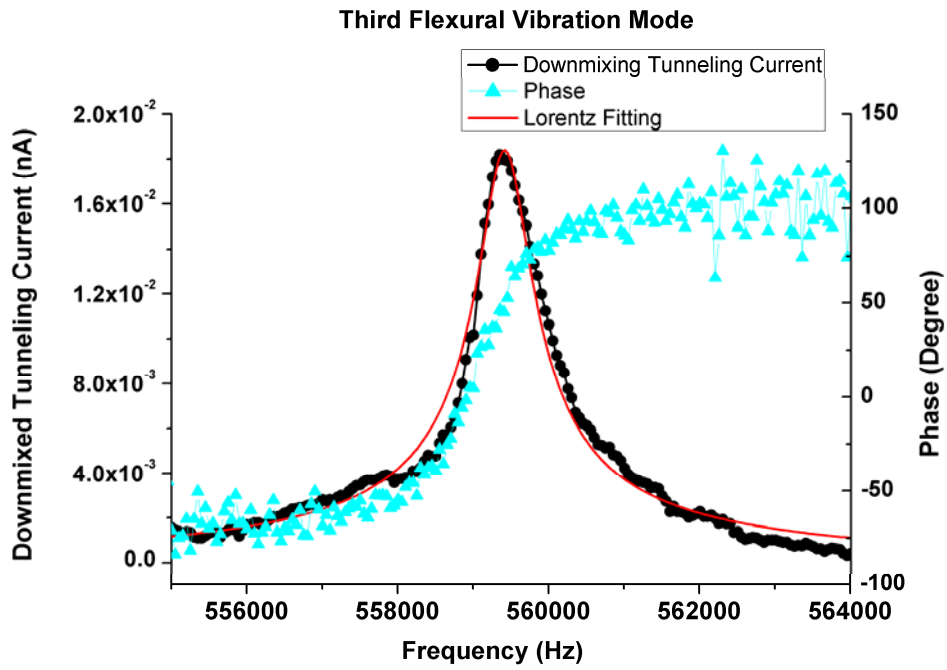
Vibration Mode Methods	First Flexural Mode	Second Flexural Mode	First Torsion Mode	Third Flexural Mode	Second Torsion Mode	Fourth Flexural Mode
COMSOL Simulation (Hz)	112801 ± 1128	305867 ± 3059	447971 ± 2240	589216 ± 1630	909188 ± 4546	954073 ± 2385
Optical Interferometry(Hz)	121554 ± 1	310982 ± 3	425921 ± 3	587658 ± 3	832837 ± 1	958476 ± 1
STM downmixing (Hz)	128021 ± 8	-	442465 ± 22	558481 ± 17	881521 ± 103	985461 ± 16



(a)



(b)



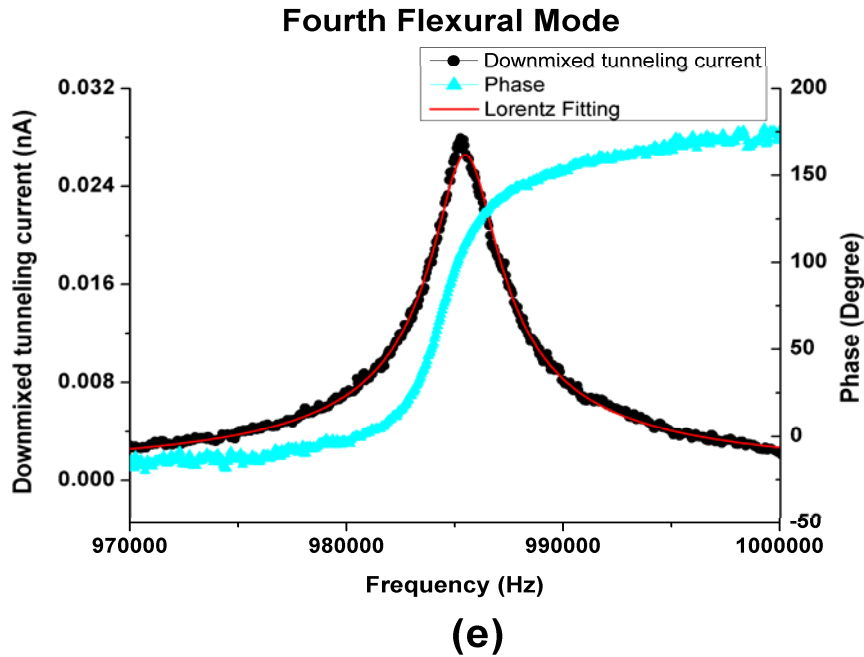


Figure 4.9 The results of STM downmixed Readout technique. The measurement conditions: DC tunneling current 0.2 nA, DC bias voltage 0.5 V, AC bias voltage 0.1 V_{rms} and piezo disk actuating power -11dBm (a) Fundamental flexural vibration mode (b) The first torsional vibration mode (c) The third flexural vibration mode (d) The second torsional vibration mode and (e) The forth flexural vibration mode. The first flexural mode is measured close to the MEMS beam edge, the third flexural mode is measured at three-fifths position and other modes are measured close the center of the MEMS beam

From the results in Figure 4.9, we can see the centre of the phase shift is different from the centre of amplitude response. In order to explore the reason, we plot the downmixed tunneling current in the complex plane, as shown in Figure 4.10. Figure 4.10 shows the downmixed tunneling current of Figure 4.9 (e) in the complex plane. The real part of the downmixed tunneling current comes from the X output of the lock-in amplifier which responses $R \cdot \cos(\theta)$ and the imaginary part of the downmixed tunneling current comes from the Y output of the lock-in amplifier which responses $R \cdot \sin(\theta)$. Thus the vibration amplitude and phase

information of MEMS devices can be clearly seen in the complex plane of the downmixed tunneling current. From Figure 4.10, we can see that the origin point of downmixed tunneling current deflects the origin of axis and the curve of downmixed tunneling current turns some degrees from the origin axis. For deflection of the origin point of downmixed tunneling current, the reasons are that some noises and the intrinsic forces of STM downmixing technique make the origin point of downmixed tunneling current deflect the origin of axis during the measure. About the rotation of the curve of the downmixed tunneling current, the main source is that the piezo disk causes an arbitrary starting phase and this can be seen in Figure 4.14 (note the piezo actuation phase drifts by 90 degrees over the 700 kHz span). Also in Figure 4.14, it shows the response of piezo disk has a phase different from the actuating force and this difference should be transferred to the motion of the MEMS device. Otherwise, the response of the MEMS device also is a reason which can cause the phase change with the actuating force. Thus, when we use STM downmixing technique to measure the nanomechanical motion, the phase information is complex. But phase information clearly responds to the motion of MEMS device which has a 180 degree phase shift at resonance frequency, although the results have some phase shift.

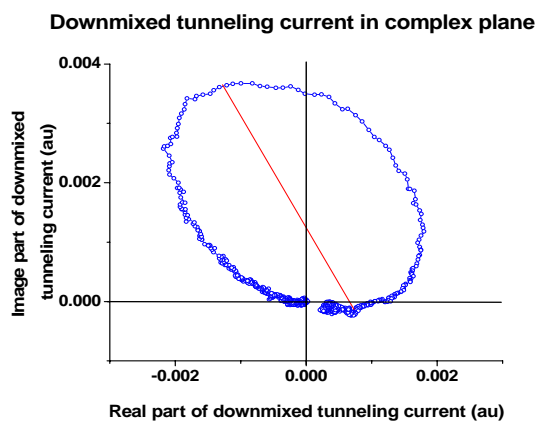


Figure 4.10 The curve shows the downmixed tunneling current of Figure 4.9 (e) in complex plane. The real part and image part of downmixed tunneling current come from the x and the y output of lock-in amplifier, separately.

In general, based on the above results, we have demonstrated that scanning tunneling microscopy can be used to measure high frequency motion information of MEMS devices with STM downmixing readout method.

4.4. The effects of measurement parameters on STM Downmixing readout Method

We further explore Scanning Tunneling Microscopy (STM) downmixing readout methods and investigate the parameters which affect the downmixing results. These parameters include the actuating power of piezo disk, the DC tunneling current between the sample and the tip, the DC bias voltage between the sample and the tip, and the measuring position along the MEMS beam.

4.4.1 Forces between STM tip and MEMS Device

In order to exploit the effect of some parameters on the STM downmixing technique, the forces between the STM tip and MEMS device should be known. In the present case, where a small distance for tunneling is required, some physical forces arising from quantized field have to be considered in addition to the electrostatic force; namely, the van der Waals force, Casimir force and short range chemical force become relevant.

The van der Waals force, named after Dutch scientist Johannes Diderik van der Waals, is the attractive or repulsive force between atoms, molecules, and surfaces. They differ from covalent bonds and the electrostatic interaction of ions in that they are caused by correlations in the fluctuating polarizations of nearby particles (a consequence of quantum dynamics). In the present case, the van der Waals force can be approximated by using the model of a sphere in front of a plane [4],

$$F_{vdW} = -\frac{HR}{6d^2} \quad (4.5)$$

where R is the radius, d is the distance between the sphere and the plane and the interaction constant H is called the Hamaker constant, defined as $H=\pi^2C\rho_1\rho_2$

where C is the attractive interaction strength and ρ_i , $i = 1, 2$, is the number density of the molecules in the solid (1 or 2).

The Casimir force is a force between uncharged metallic surfaces as a result of quantum vacuum fluctuations of the electromagnetic field [5] with a large impact in micro- and nanotechnology [6] [7]. According to the proximity force theorem [8] [9], the Casimir force using the geometry of a sphere in front of a plane can be written as:

$$F_{cs} = - \frac{\pi^3 \hbar c}{360} \frac{R}{d^3} \quad (4.6)$$

where R is the radius, d is the distance between the sphere and the plane, \hbar is the Planck constant/ 2π , and c is the speed of light. When the separation between the STM tip and MEMS device decreases, the Casimir force rapidly increases.

Also with the sphere model, the capacity of tip and MEMS device is deduced from the expression of the force between a sphere and a plane [10].

$$F = 2\pi\epsilon_0 V_{bias}^2 \sum_{n=1}^{\infty} \left(\frac{\coth \alpha - n \coth(n\alpha)}{sh(n\alpha)} \right)$$

with

$$\alpha = \arg ch\left(\frac{d+R}{R}\right) \quad (4.7)$$

Where d is the distance between the STM tip and the surface of the sample, R is the radius of the STM tip and ϵ_0 is vacuum permittivity. In this case $d \ll R$, the force in Equation (4.6) reduces to:

$$F_{el} \cong -\pi\epsilon_0 V_{bias}^2 \frac{R}{d} \quad (4.8)$$

Figure 4.11 gives an overview of the distance of the various forces. The parameters used for various forces are $H=4 \times 10^{-20} \text{J}$, $\hbar=1.05459 \times 10^{-34} \text{J}\cdot\text{s}$,

$\epsilon_0=8.85 \times 10^{-12} \text{F/m}$, $V_{\text{bias}}=0.5 \text{ V}$, and $R=10 \text{ nm}$. In the case of distance $d < 1 \text{ nm}$ the Casimir force is far larger than van der Waals force and electrostatic force, even the total of van der Waals force and electrostatic force.

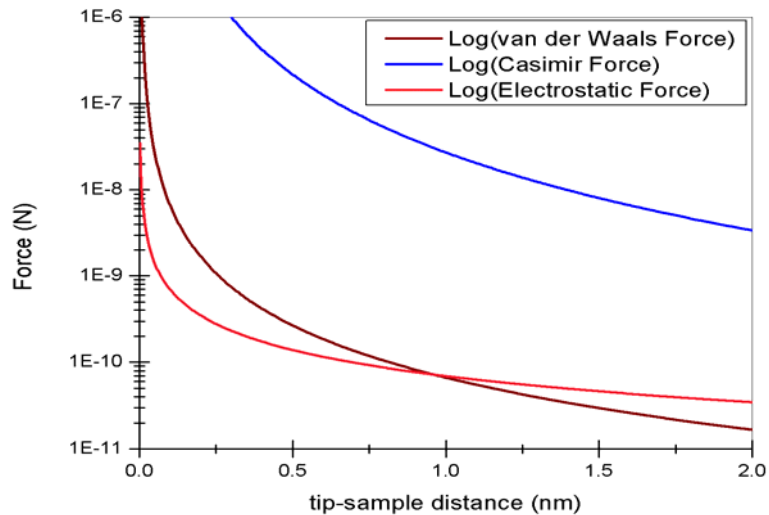


Figure 4.11 Information of van der Waals force, Casimir force and Electrostatic force for different distance between the tip and the sample at DC bias voltage 0.5 V and the tip diameter 10 nm.

For the STM system the forces described above are the attractive forces which attract the MEMS devices toward the tip of the STM. Besides these forces, there are some short range repulsive forces which repulse the MEMS device away from tip and these short range forces are become obvious when STM downmixing technique was used to measure the displacement of MEMS devices. The distribution of total forces for STM system is shown in Figure 4.12. From Figure 4.12, we can see that the forces between the tip and the surface of MEMS device change with the change of distance between the tip of STM and the surface of MEMS device and there are two regimes: repulsive regime and attractive regime. An equilibrium distance exists and depends on the situation of the surface of sample (usually about 3 \AA). For the STM downmixing technique, the main force

effects come from the repulsive regime and this agrees with the experimental observation of force acting during scanning tunneling microscopy [12].

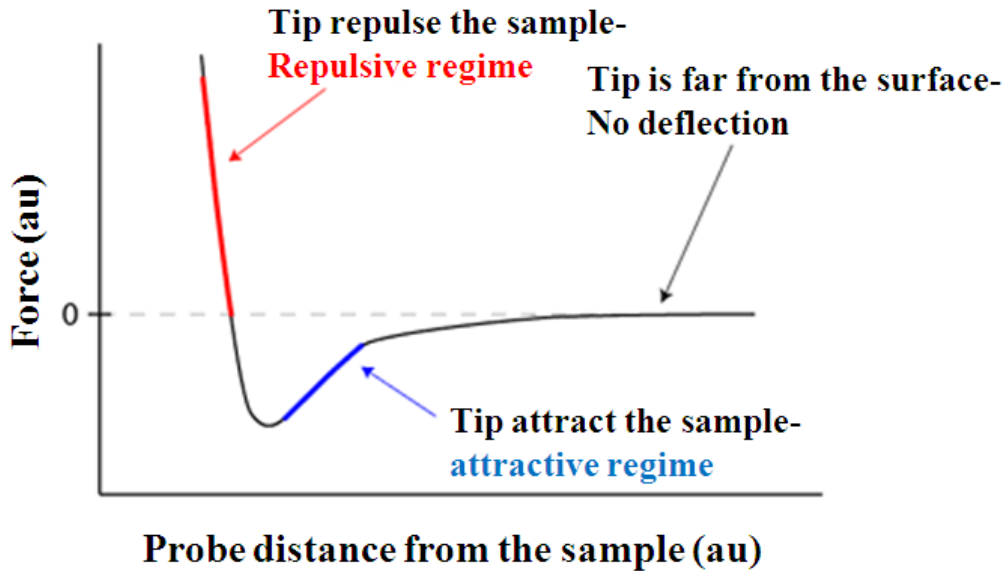


Figure 4.12 The scheme shows force distribution of scanning tunneling microscope with the distance from the tip to the surface of the sample. For a scanning tunneling microscope system, there are two force regimes- repulsive regime and attractive regime- which have different effect on the motion of MEMS devices

4.4.2 The Effect of Changing DC Tunneling Current

DC tunneling current is used to set the distance between the tip and the sample and impact the sensitivity of measurement. In this section we will focus on the DC tunneling current impact on the downmixed tunneling current and resonance frequencies.

The initial experimental condition is set as: the piezo disk actuating power -11 dBm (22 dBm attenuator is connected between the power splitter and piezo disk), DC bias voltage on the tunneling junction of $0.5 V_{\text{rms}}$ which directly comes from RHK control system and AC bias voltage on the tunneling junction of $0.1 V_{\text{rms}}$

which is provided by the single-side band mixer. Following this original experimental condition, we scan the MEMS beam excitation frequency to find the resonance frequencies and downmixed tunneling current peak amplitude as a function of different DC tunneling currents and the results are shown in Figure 4.13. From Equation (4.2), we can see that the downmixed tunneling current is linear to $e^{-2\kappa d}$. Also the DC tunneling current is linear to $e^{-2\kappa d}$. Thus the correlation between the DC tunneling current and downmixed tunneling current is linear relationship. When the DC tunneling current is increased, the downmixed tunneling current should increase and keep this linear relationship. In Figure 4.13(b), we show that the downmixed tunneling current peaks are increasing with increasing DC tunneling current and this agrees with the deduction and the prediction. This result means that at the same conditions we can increase the sensitivity by increasing the DC tunneling current to make the tip close to the sample. Now let us discuss how the DC tunneling current impact the resonance frequency.

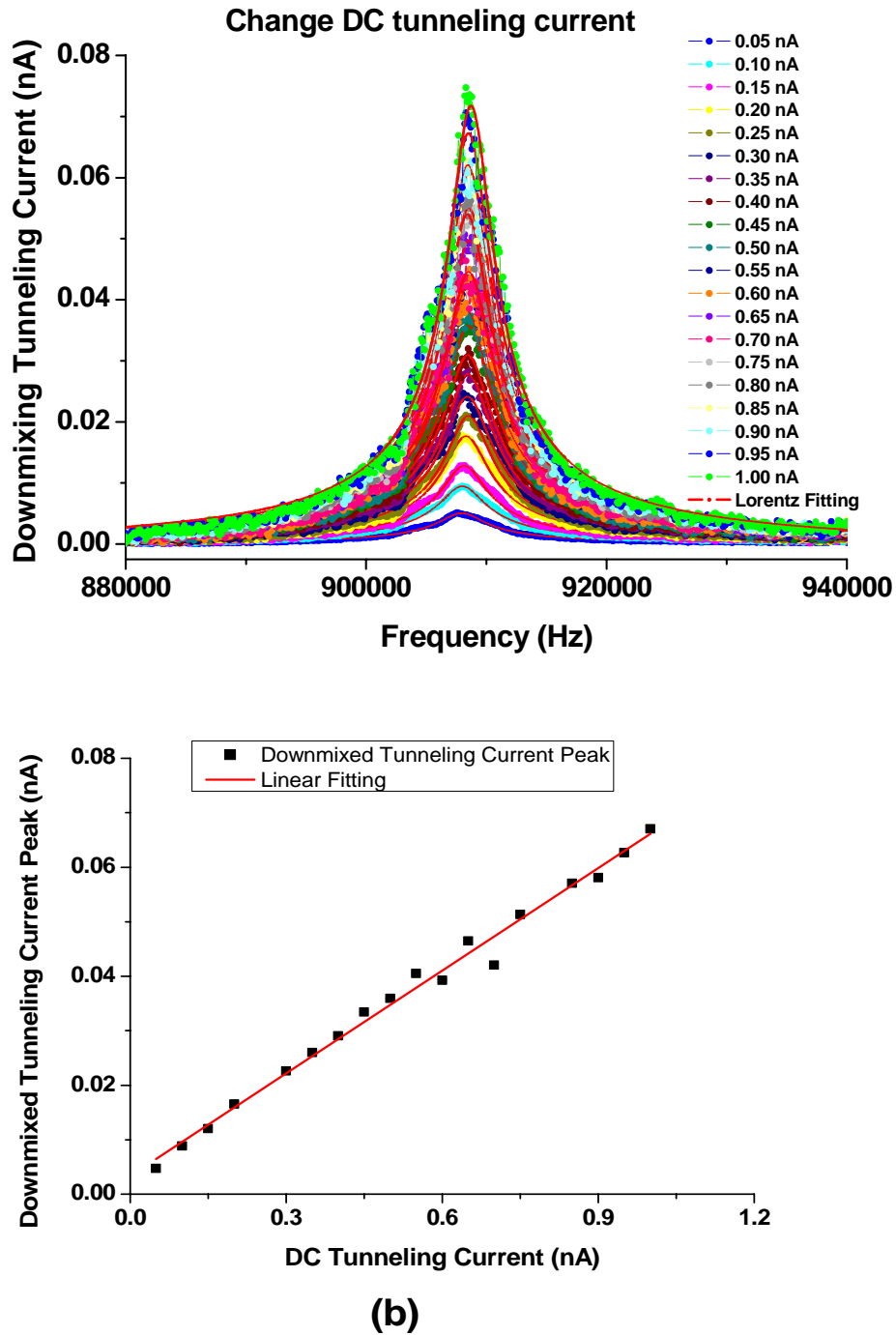
When the vibration amplitudes of the MEMS beams are sufficiently small, the tip-MEMS beam-spring system can be reduced to a harmonic oscillator with a resonance frequency f_r which is determined by the resonance frequency of the unperturbed MEMS beam and the interaction force gradient [12].

$$f_r = f_0 \sqrt{1 + \frac{K_i}{K}} \quad (4.9)$$

where f_0 and K are the resonance frequency and the spring constant of the free MEMS beam of, K_i is the interaction force gradient $K_i \equiv dF/dz \equiv d^2U/dz^2$ (where U is the interfacial interaction potential).

When we increase DC tunneling current, the distance between the tip and the surface of MEMS beam becomes smaller. From the discussion of section above, we know that the forces – repulsive regime - increase with the decrease of the distance between the tip and the surface of MEMS beam. The increase of the forces and the decrease of distance between the tip and the surface of MEMS

beam cause the increasing of the force gradient of the tip-MEMS beam-spring system. Thus according to Equation (4.9), we can know the resonance frequency of the MEMS device increase with the increasing of DC tunneling current and this qualitatively agrees with the measurement results shown in Figure 4.13 (c).



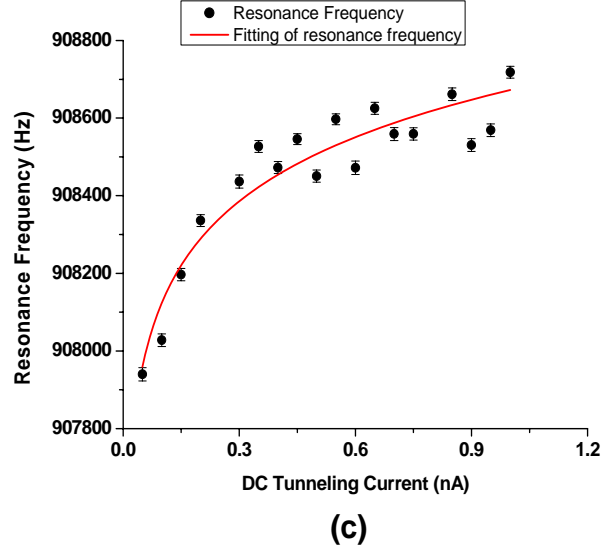


Figure 4.13 The influence of DC tunneling current. The results are measured at the four-tenths of the doubly-clamped beam position for the fourth flexural vibration mode and the measurement conditions are: DC bias voltage 0.5V, AC bias voltage $0.1V_{\text{rms}}$ and piezo disk actuating power -11dBm. (a) The results and fitting of downmixed tunneling current for different DC tunneling current (b) The effect on downmixed tunneling current peak by DC tunneling current (c) The effect on resonance frequencies by DC tunneling current.

The above measurements are done for the fourth flexural modal of doubly clamped beam. In order to understand the results which follow the Equation (4.9), we calculate the spring constant of the fourth modal. The fourth modal spring constant is defined as [18]:

$$K_4 = \frac{EI}{l^2} \int_0^l (\phi_4''(x))^2 dx \quad (4.10)$$

Using Equation (1.6), we can get*:

$$\phi_4''(x) = K_4^2 C_{14} (-\cos(K_4 x) - \cosh(K_4 x)) + K_4^2 C_{24} (-\sin(K_4 x) - \sinh(K_4 x)) \quad (4.11)$$

*Note: K_4 in Equation (4.11) which is different from the spring constant K_4 in Equation (4.10) is the eigenvector of the MEMS device motion function and is defined in Equation (1.5).

From Table 1.1, we can get $C_{14} = -l$ and $C_{24} = l$ for the fourth modal. Then Equation (4.11) is substituted into Equation (4.10) and we can get:

$$K_4 = \frac{37119EI}{l^3} \quad (4.12)$$

For a 500 μm long, 100 μm wide and 5 μm thick silicon doubly-clamped beam, the spring constant of the fourth modal is about 23000 N/m.

For a STM system, the force gradient usually changes from 0.5 N/m to 200 N/m for the repulsive regime [17]. Thus using Equation (4.9), we can predict that the resonance frequency shift is about 0.43% for the fourth modal of our MEMS device. From the measurement results of Figure 4.13 (c), the shift of resonance frequency of our measurement is about 0.11% and it agrees with the prediction of Equation (4.9).

4.4.3 The Effect of Change DC Bias Voltage

As an important parameter of STM system, DC bias voltage impacts the downmixed tunneling current peak and resonance frequencies of the MEMS device with the STM downmixed method. The value of DC bias voltage determines the relation between the tunneling current and the DC bias voltage [13] and impacts the sensitivity of the STM downmixing method.

During this experiment, the piezo disk actuating power, DC tunneling current and AC bias voltage are constant and the DC bias voltage is changed to measure the vibration motion information of MEMS devices. Here, the actuating power of piezo disk is -11dBm, DC tunneling current is 0.2nA and the AC bias voltage is 0.1V_{rms}. Based on these conditions, the influence of DC bias voltage to downmixed tunneling current peak and the resonance frequencies of the MEMS device are measured and the results are shown in Figure 4.14.

In Simmons' classic paper [13], he presented about the relation between the tunneling current density and the bias voltage for a planar tunnel junction. For the

case that the bias voltage is far less than the barrier height, the tunneling current density is a linear function of DC bias voltage. When the voltage is increased to intermediate range, the tunneling current density J through the tunneling junction (usually a metal-insulator-metal junction) obeys the general relation:

$$J = \beta (V + \gamma V^3) + O(V^4) \quad (4.13)$$

where β and γ depend on the average barrier height and the tip-sample distance. Since the AC part of bias voltage is constant, when we increase the DC bias voltage, the ratio of the AC bias voltage to the DC bias voltage becomes smaller. This directly causes a smaller ratio of the dynamic distance to the static distance and the downmixed tunneling current on resonance becomes smaller compared that measured at the lower DC bias voltage. The downmixed tunneling current should meet the following correlation:

$$I_{downmixed} \propto \frac{V_{rms}}{V_{DC}} I_{DCtunnelingcurrent} \quad (4.14)$$

In other words, the downmixed signal is inversely proportional to the DC bias voltage. From the measured result between the downmixed tunneling current and DC bias voltage in Figure 4.14(b), the curve is basically similar to the discussion in the relation of tunneling current density and bias voltage.

In order to investigate the impact of the various DC bias voltages on frequency, we introduce two forces into the equilibrium system of MEMS device: the electrostatic force, attracting the beam toward to the STM tip, and the elastic restoring force, trying to pull the beam back to its undeformed state. The equation of motion for the beam can be written as:

$$EIu_{xxxx} - [T_0 + T(u_x)]u_{xx} + \rho A u_{tt} = \frac{1}{2} C_z [z(x, t)] V^2 \quad (4.15)$$

Here A is the beam's cross-sectional area, E is Young's modulus, ρ is the beam density, and I is the moment of inertia about the longitudinal axis of the beam.

The total tension term in brackets, $[T_0 + T(u_x)]$, is a sum of residual tension T_0 and bending-induced tension: $T(u_x) = (ES/2l) \int_0^l u_x^2 dx$, where l is the beam length. $C_2[z(x,t)]$ is the capacitance between the STM tip and the MEMS device and is calculated based on the sphere model [10].

The beam's total displacement $u(x, t)$ can be written as the sum of a static displacement $z_s(x)$ and a time-varying ac displacement $z(x, t)$: $u(x, t) = z_s(x) + z(x, t)$. To find the frequency in the equation for the time-varying displacement, we approximate the beam shape as $z(x, t) = z_1(t) \sqrt{2/3} [1 - \cos(2\pi x/l)]$ [14] [15]. A similar expansion of static deflection, $z_s(x, t) = A_{dc} \sqrt{2/3} [1 - \cos(2\pi x/l)]$, is used in the static equilibrium equation to solve for the static deflection amplitude A_{dc} . The equation of motion can be written as [15]:

$$\ddot{z}_1(t) + \omega_r^2 z_1(t) + \alpha_2 z_1^2(t) + \alpha_3 z_1^3(t) = 0 \quad (4.16)$$

For the linear situation, the cubic and quadratic nonlinear coefficients, α_3 and α_2 , is equal to zero.

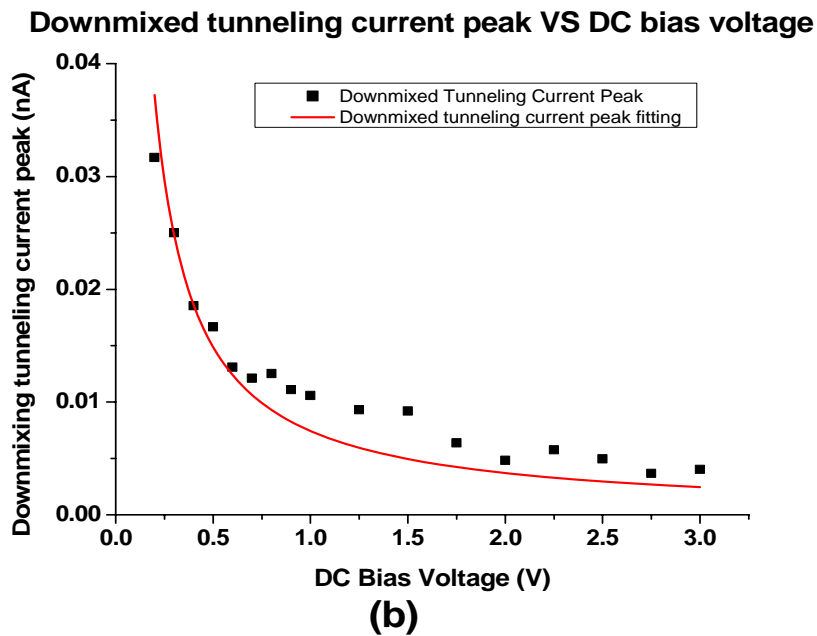
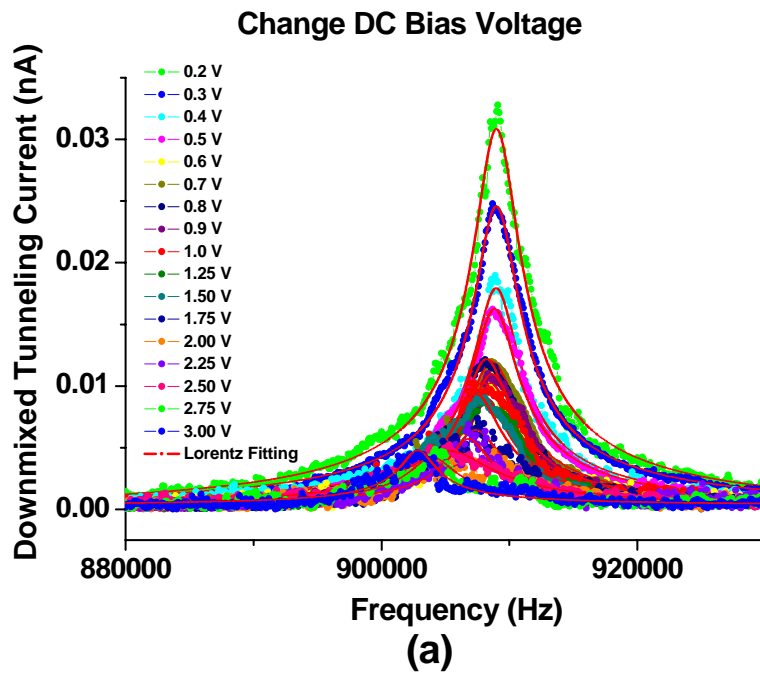
$$\omega_r^2 = \left[\frac{EI}{3\rho A} + \frac{EA_{dc}^2}{6\rho} \right] \left(\frac{2\pi}{l} \right)^4 + \frac{T_0}{3\rho A} \left(\frac{2\pi}{l} \right)^2 - \frac{K_c V^2}{\rho A} \quad (4.17)$$

Here K_c is capacitance expansion coefficient and is given by the geometry. For a doubly-clamped beam, the residual tension T_0 and the static deflection amplitude A_{dc} are very small and can be omitted. Thus Equation (4.17) can be rewritten as:

$$\omega_r = \sqrt{\frac{EI}{3\rho A} \left(\frac{2\pi}{l} \right)^4 - \frac{K_c V^2}{\rho A}} \quad (4.18)$$

The Equation (4.18) also can be written as the format of the Equation (4.9). Thus, because the interaction potential between the Pt-Ir tip and the gold surface of MEMS devices bring an electrostatic force to make force gradient change when we change the DC bias voltage and this electrostatic force belong to attractive

force, the resonance frequencies will decrease with the increase of the DC bias voltage. This trends agree with the measurement of STM downmixing method, as shown in Figure 4.14 (c). The similar results about the impact of DC bias voltage to the resonance can be found at Kozinsky's paper [2].



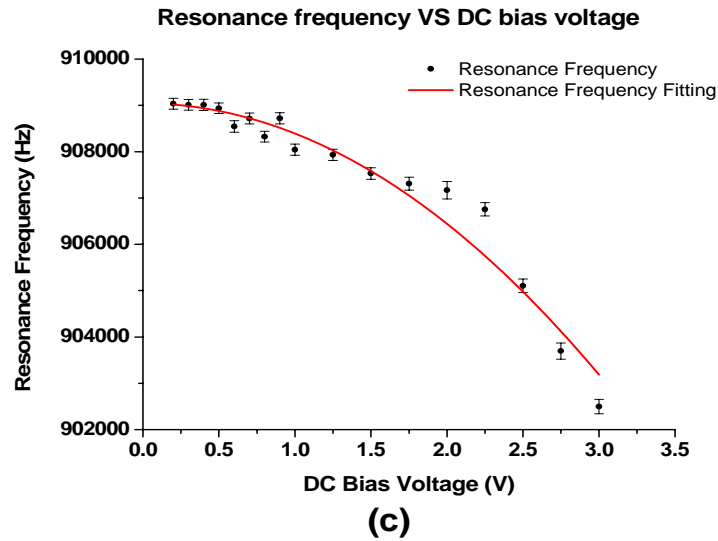


Figure 4.14 The effect of DC Bias Voltage in STM Downmixing Technique. The results are measured at the four-tenths of the doubly-clamped beam and the measurement conditions are: DC tunneling current 0.2 nA, AC bias voltage $0.1V_{\text{rms}}$ and piezo disk actuating power -11dBm. (a) The results and fitting of downmixed tunneling current for different DC bias voltage (b) The effect on downmixed tunneling peaks change by DC bias voltage (c) The effect on resonance frequencies by DC bias voltage.

4.4.4 The Effect of Change Piezo Disk Actuating Power

The change of actuating power causes the change of force which is used to drive the MEMS motion. In the linear region of piezo disk, the driving force is proportional to applied voltage and will increase with increasing driving force. Figure 4.14 shows the frequency response, measured by reflection, of the piezo disk which is used for actuating our MEMS devices. The inset graphs of Figure 4.14 just magnify the interesting sections of Figure 4.14.

The piezo response, though not entirely flat over the range of interest for exciting the MEMS device, changes relatively slowly with frequency; we will assume the driving force constant over the frequency scan range and linear with driving voltage.

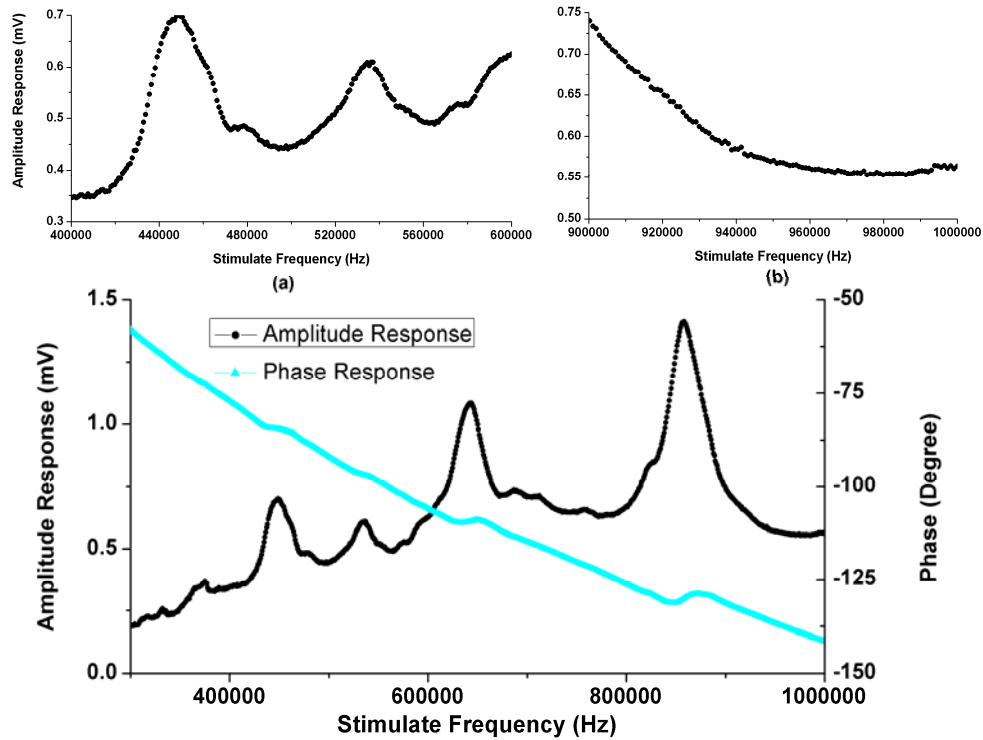


Figure 4.15 The piezo disk frequency response with MEMS device at the top. Inset graph (a) shows the piezo disk frequency response from 400 kHz to 600 kHz and (b) shows the piezo disk frequency response from 900 kHz to 1 MHz

The bigger force makes the vibration amplitude of the MEMS devices larger. Thus the gap between the tip and the sample is modified by the actuating power and the downmixed current should change as well. In order to measure the effect of actuating power, we set the DC bias voltage to 0.5 V and the DC tunneling current 0.25nA as the initial state of the STM and apply our down-mixing readout for variable attenuation. Attenuators are used to change the actuating power of the piezo disk. The downmixed tunneling current and the resonance frequencies are modified by the actuating power, as shown in Figure 4.15.

From Equation (3.1) that gives the relationship between the tunneling current and the distance from the tip to sample, we can get the following equation:

$$\begin{aligned}\partial I &= (-2\kappa)\rho_s(E_F)Ve^{-2\kappa x}\partial d \\ \Rightarrow \frac{\partial I}{\partial d} &= (-2\kappa)I\end{aligned}\quad (4.15)$$

From Equation (3.5) the relationship between the actuating force and the applied voltage, we can get the following relationship:

$$\partial F = D\partial V \quad (4.16)$$

Then we use the Equation (3.7) which gives the relationship between the actuating force and vibration amplitude to get:

$$\partial d = \left(\frac{1}{\rho Al^3} \frac{1}{\omega_m^2 - \omega_c^2 - i\omega_m/Q} \int_0^l u_m(x) dx \right) \partial F \quad (4.17)$$

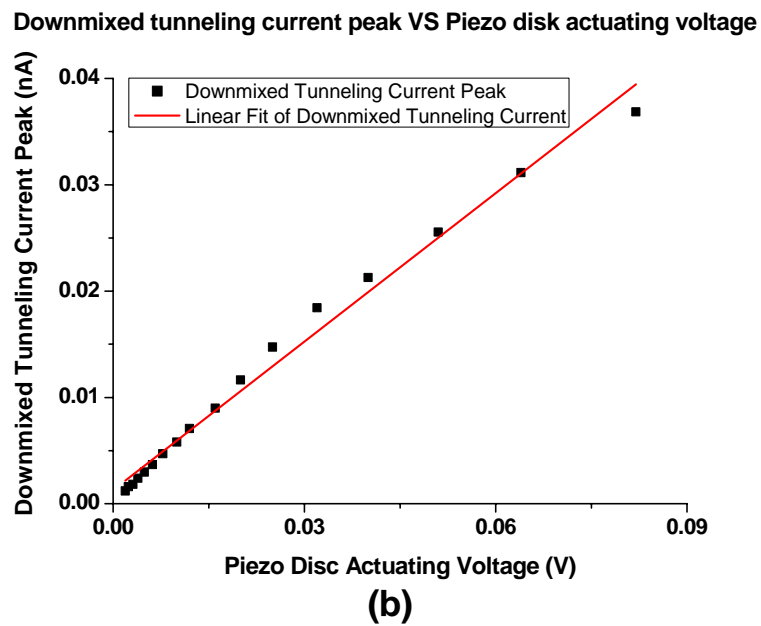
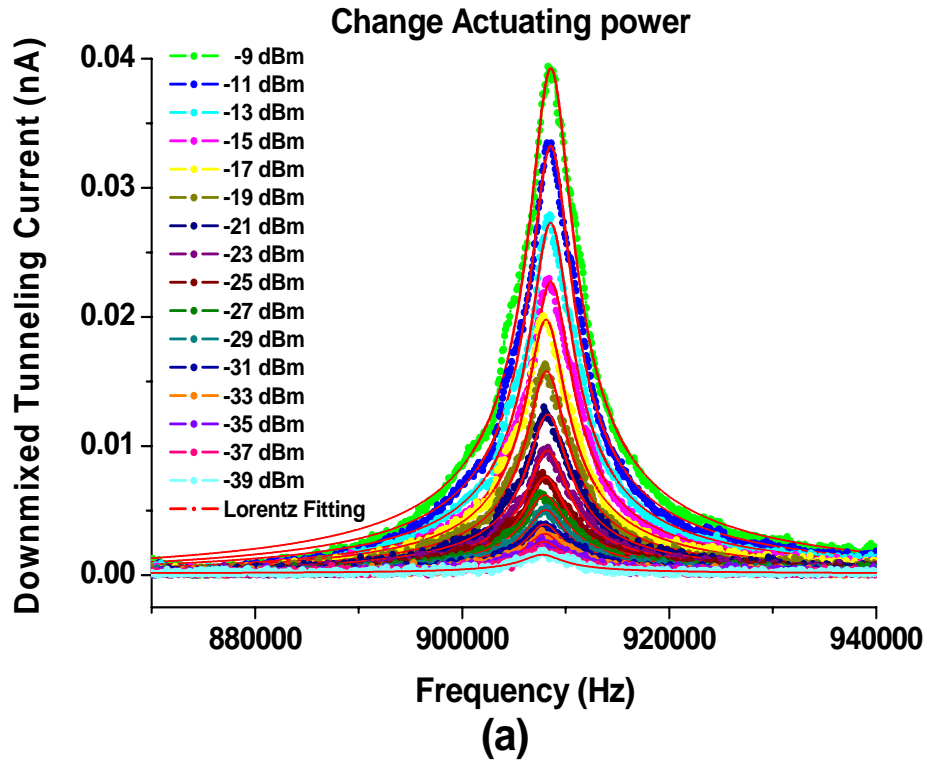
Using the equation (4.15), (4.16) and (4.17), we can get:

$$\frac{\partial I}{\partial V} = \frac{\partial I}{\partial d} \frac{\partial d}{\partial V} = -\frac{2\kappa I}{\rho Al^3} \frac{D}{\omega_m^2 - \omega_c^2 - i\omega_m/Q} \int_0^l u_m(x) dx = \text{constant} \quad (4.18)$$

For the given STM initial state, the right side of Equation 4.21 is a constant quantity at given drive frequency which depends on the MEMS material and vibration mode. We thus expect the MEMS down-mixed current signal to respond linearly with applied actuating voltage, consistent with the measurement result which is shown in Figure 4.15 (b).

The resonance frequencies are also modified by the actuating power, as shown in Figure 4.15 (c). It is possible since the varying actuating power does change the driving forces. Any non-linearity in the MEMS system response to driving force (such as a Duffing or cubic term in the restoring elastic force) can result in frequency shifting at higher powers. That is, the varying driven force seems to result in a spring constant change of the elastic beam [3] [4] that causes the resonance frequency fluctuation shifting. It is possible instead that the tip

interaction itself provides an amplitude dependent spring constant that is causing the frequency shifting. For example, reference [16] derives amplitude dependent frequency shifts for large amplitude tip sample interactions.



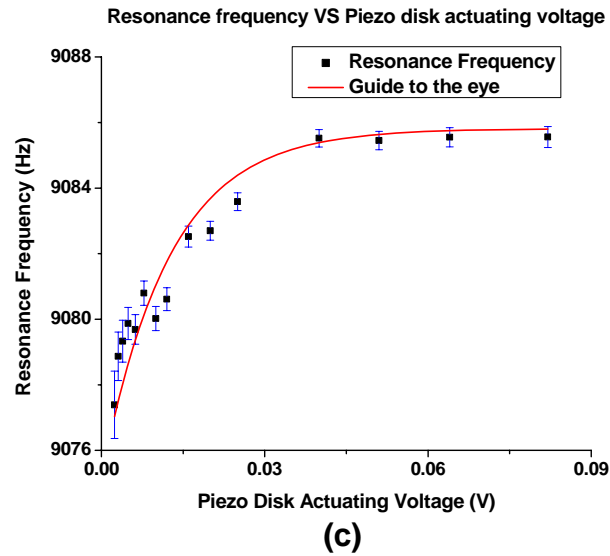


Figure 4.16 The impact of actuating power for STM downmixing technique. These results are measured at the four-tenths of the doubly-clamped beam and the measurement conditions are: DC tunneling current 0.2 nA, DC bias voltage 0.5 V and AC bias voltage $0.1V_{\text{rms}}$. (a) The results and fitting of downmixed tunneling current for different actuating power (b) The effect on downmixed tunneling current peak change by piezo disk actuating voltage (c) The effect on the resonance frequencies by the piezo disk actuating voltage.

To try to shed some light on this frequency dependence, we measure a nominally identical MEMS device under varying drive power using the optical interferometry method. The result is shown in Figure 4.16. In this case, the frequency actually shifts slightly downward with increasing drive voltage, the opposite direction to the STM measured case. In both case, the actual frequency shifts are relatively small. For example, the shift for the STM case (about 600Hz) is about 1/8th of the mechanical resonance linewidth and for interferometry (about 300 Hz) is 1/16th of the mechanical resonance linewidth. For the optical interferometry measurement, the forces should come from the driving force of the piezo disk. But for the

STM downmixing case, forces which come from the tip due to the distance change between the tip and the sample and the driving force of the piezo disk together causes the frequency shifts. The direction of total force is changed and this causes the trend of resonance frequency change different.

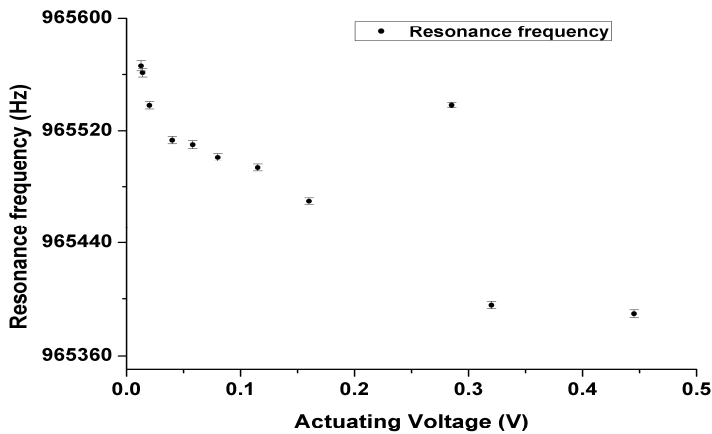
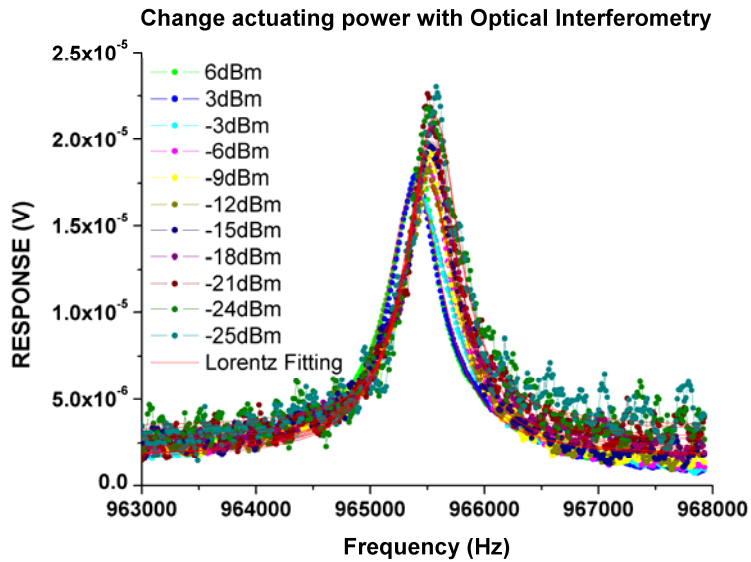


Figure 4.17 The effect of actuating power with optical interferometry method. (a) The results and fitting curve of response with frequency (b) Resonance frequency are modified by actuating power.

4.4.5 The Effect of the Measuring Position

When the STM downmixing method is used to detect the motion of MEMS devices, there are intrinsic physical forces between the tip of the STM and the surface of the MEMS device which modify the resonance frequencies of MEMS during the measurement. Since these interaction forces are point forces, the effect of these interaction forces would be sensitive to the applied position on the MEMS device. In order to explore the effect of different measuring points, we measure some positions along the beam length direction and across the width direction. Along the length, we measure the MEMS beam at 10 points where the distance between adjacent points is uniform. For the width direction we only measure three different points due to the smaller of width. These points are measured with the same measurement condition: DC bias voltage of is 0.5V, AC bias voltage is $0.1V_{\text{rms}}$, DC tunneling current is 0.2nA and the piezo disk actuating power is -11dBm. Thus will be propitious to compare and analyze the results.

Based on above initial condition, we measure the fourth flexural mode information of the 10 points along the length direction and the measured results are shown in Figure 4.18 (a). The normalized vibration amplitude of each measured point on the fourth flexural mode is shown in Figure 4.18 (b). For the fourth flexural mode of the MEMS device, there are four half cycles of vibration amplitude along the beam. When the beam is roughly divided into 10 uniform parts, for the fourth flexural mode three kinds of nodes along the length can be gotten. The points 1, 4, 6 and 9 have the similar position for each cycle which is close to the vibration center of each cycle (the modal antinode and shown on red line) than the other two groups. These points have bigger impact on the resonance frequencies and cause the resonance frequencies to shift more than the other two groups. The distances from points 2, 3, 7 and 8 to the center of each cycle are medium, so the impact of these points on the resonance frequencies should be smaller than points 1, 4, 6 and 9 and bigger than points 5 and 10. From Figure 4.16, we can see this result. The impact on resonance frequencies for points 5 and 10 are the smallest and the resonance frequencies of point 5 and 10 are higher

than the other two situations. But for the point 1, 4, 6, and 9, the impact on the resonance frequencies are the biggest one and the resonance frequencies are the smallest among the three groups. From these results, there should be a force between the tip and the sample surface which has a strong or weak effect on frequency dependent on the local modal amplitude. When the MEMS devices vibrate, the force gradient influences the compliance of the combined tip-MEMS beam system and changes the MEMS bending shape for a given mode of excitation. These effects cause a shift of resonance frequency. The resonance frequencies of each measured point on the fourth flexural mode are listed in Figure 4.18 (c) and this follows the above analysis. The detailed results with phase information for these points can be seen in Appendix D. Here we only show the results of the resonance frequencies for these points.

Further, the phase of the responses at different points also seems to bear some relationship, with the exception of position 8, to be modal shape of this resonance. Phase is listed in brackets underneath the points and refers to the phase at the position where the amplitude of beam is max. For example, in the set of positions 1, 4, 6, and 9, the positions 4 and 9 are in the second and fourth quadrants of the mode, while the positions 1 and 6 are in the first and third. These even and odd quadrants should have a phase shift 180 degrees with respect to each other in terms of their response as they should be oscillating out of phase. Indeed, the phase at positions 1 and 6 are roughly same, positions 4 and 9 are roughly the same, and each set is roughly 180 degrees out from the other. This can clearly be seen in Figure 4.19 which shows downmixed tunneling current in complex plane. The values of X and Y axis represent the product of downmixed tunneling current and the cos and sin of phase of NEM, separately. Position 8, however, does not sit correctly in this pattern with its cohort of position 2, 3, and 7. Thus, there is more going on with the phase than we yet fully understand.

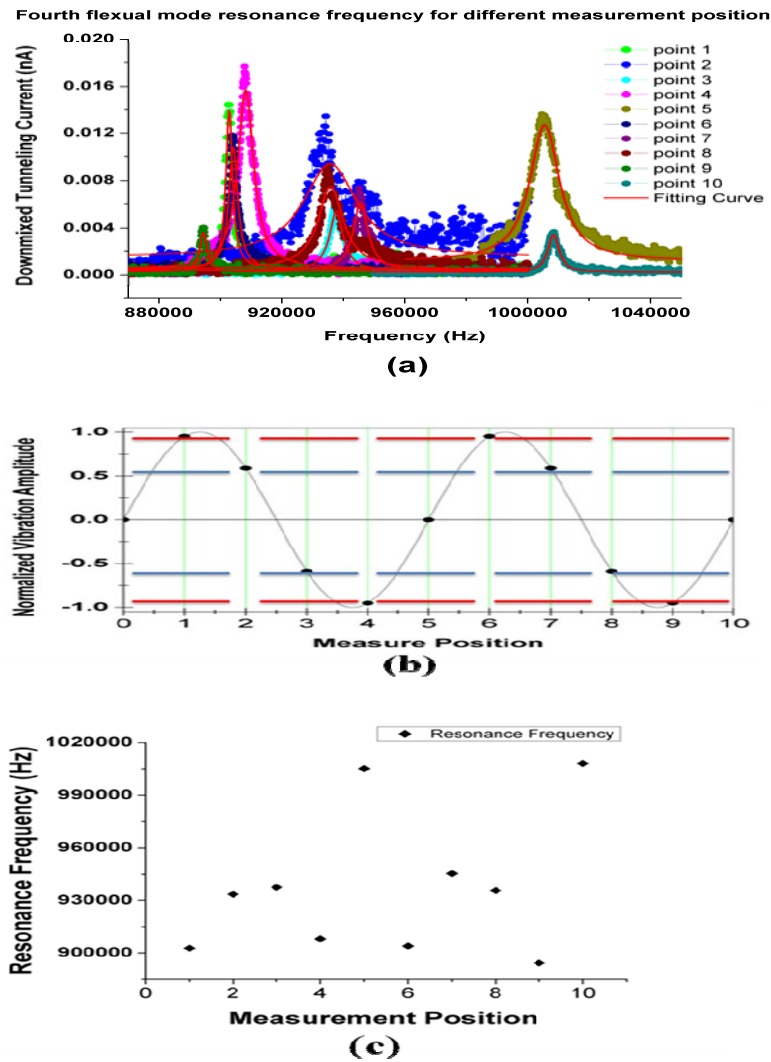


Figure 4.18 Effects of the measured point along MEMS beam length direction. The measurement conditions are: DC tunneling current 0.2 nA, DC bias voltage 0.5 V, AC bias voltage 0.1 V_{rms} and piezo disk actuating power -11dBm. (a) The results and fitting curves of different measuring positions (b) The vibration amplitude of each point. The points on the red line have similar vibration amplitude and the points on the blue line also have similar vibration amplitude. (c) Resonance frequencies of each points which response the change of the vibration amplitude of each point. The points on the red line have similar resonance frequencies and the points on the blue line have similar resonance frequencies.

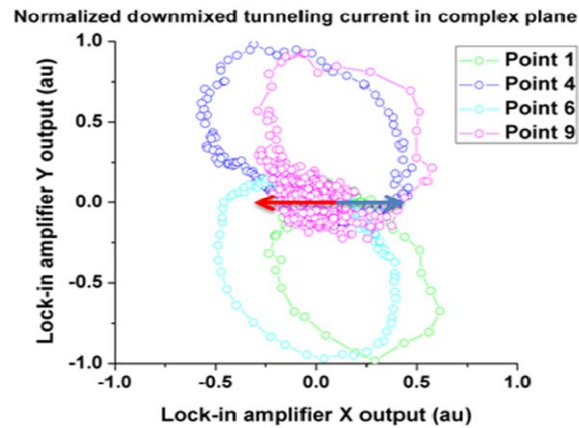


Figure 4.19 **The information of the position 1, 4, 6, 9 in complex plane.** X is the real part of downmixed tunneling current and Y is the image part of downmixed tunneling current. The red arrow shows the phase change direction of point 1 and 9 and the blue arrow shows the phase change direction of point 4 and 6.

Otherwise, we also find that some resonance frequencies are little affected by the measuring position. In Figure 4.20, the resonance frequencies of 10 points along the length direction are almost similar and have no big shift. The reasons that cause these differing results are not understood at present. The constant frequencies maybe come from the vibration of the tip or the similar impact on the MEMS device for one special mode at the 10 points. In order to fully understand the STM downmixing method, we need to further explore the effect of the measuring position on the resonance frequencies and the phase shift information for the different points.

In order to elucidate the causes of resonance frequency shift, we also measure the change of resonance frequencies across the width direction for some positions for the first torsional mode resonance. We find that the resonance frequencies change with the measuring position of MEMS beam. The graph (as shown in Figure 4.21) displays the measurement position, vibration and phase information at point 1415 along the length (of 1700 total length) as well as at the center. The results show that the resonance frequency increases when the measured point moves to the

edge of MEMS beam. This, again, tells something about how effective the local tip-sample interaction potential is, having more effect at larger amplitude (lower effective bare stiffness) regions.

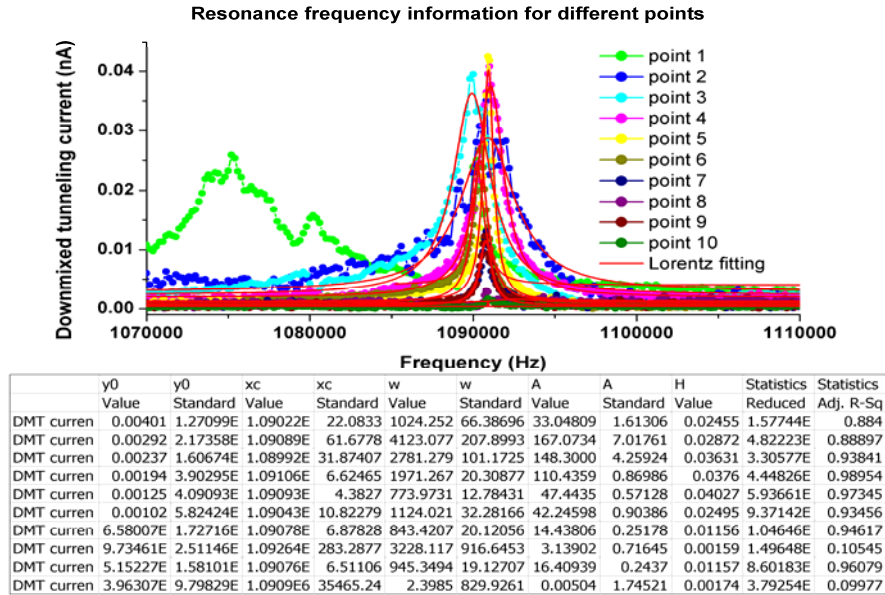


Figure 4.20 Effect of resonance frequency for different measured point along the length direction of the MEMS beam (small resonance frequency shift). The measurement conditions are: DC tunneling current 0.2 nA, DC bias voltage 0.5 V, AC bias voltage 0.1 V_{rms} and piezo disk actuating power -11 dBm.

For the reasons what cause the different phase, we cannot clearly explain that until now. We can clearly find this phase information is related to the initial condition and the measuring point. If we measure the same point with the same initial condition, we get the same results for the phase change. One speculation is that the centerline measurements (position B and E) are slightly toward the negative side of centerline. They thus share their individual phase with their negative side neighbors (position C and F) as the torsional mode is pushing that entire side at the same direction. The position A and D, on the positive side of centerline, are opposite in phase to their counterparts as that whole side is pushed

in the opposite direction during torsion. However, this motion does not explain why the set A, B, C and the set D, E, F have opposite phase. More work needs to be done to understand the phase information we measured.

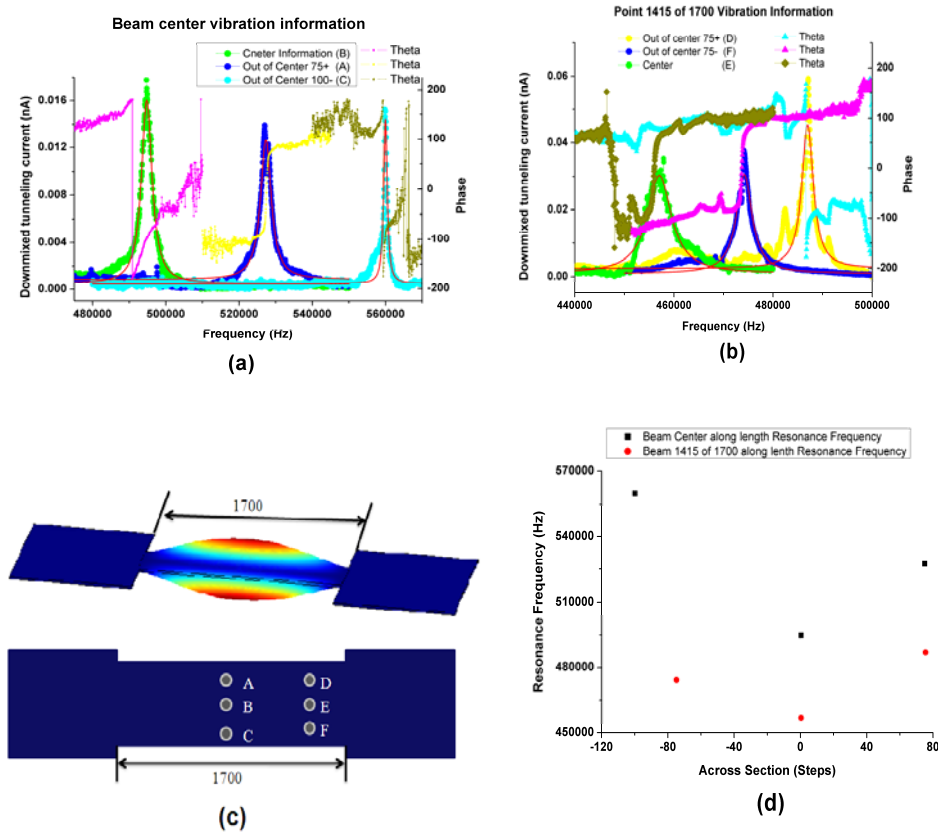


Figure 4.21 Effects of the measured point along MEMS along the width direction of the MEMS beam. The measurement conditions are: DC tunneling current 0.2 nA and DC bias voltage 0.5 V, AC bias voltage 0.1 V_{rms} and the piezo disk actuating power -11 dBm. (a) The information at the center of the beam and the letters in brackets responding the position shown in graph (c). (b) The information at 1415 of 1700 of beam and the letters in the bracket responding the position shown in graph (c). (c) The scheme of the first torsion mode and measurement points across wide direction. (d) Show the resonance frequency across the wide direction for two positions along the long direction.

4.5. The displacement sensitivity of the STM downmixing readout method

The displacement measurement sensitivity of the STM downmixing is limited by the current noises present in the measurement system. Given a small change in the distance separation, there will be a corresponding shift in the tunneling current, also downmixed tunneling current. If the change of downmixed tunneling current is below the current noise floor, then it is impossible to distinguish the response from the noise.

For our experiment, we can use the spectrum analyzer software of the RHK control system to measure the current noise. The measured results are shown in Figure 4.22, when the piezo disk actuating power is set to zero. From the graphs we can see the current noise at 4.5 KHz is about 10^{-13} A/Hz^{1/2} which include current noise of the amplifier, the shot noise, the current noise which is caused by backaction forces and some electrical and mechanical noise coming from our STM system at the tunneling range. When the tunneling current is 0.25 nA and κ is 1.15 \AA^{-1} , the displacement measurement sensitivity of STM downmixing system is $17.4 \text{ fm/Hz}^{1/2}$. The achieved displacement sensitivity will be worse than this value, because in the calculation κ is based on the clean surface and in the real condition it should be lower. The κ value can be measured based on the method in Appendix E, when the electrical charge density displacement either Z piezo of STM or piezo disk with the sample is known.

In general, this displacement sensitivity is far lower than the calculated prediction in Chapter 3. This is because that the estimation of displacement sensitivity in Chapter 3 is in ideal condition and clean surface. At the real STM system, some backaction force noise, mechanical and electrical noises exist really and cause the higher noise floor during the measurement. In order to increase the displacement measurement sensitivity of the STM downmixing method, some works are required to optimize the STM system and decrease the mechanical and electrical noise in the system. Otherwise we also can increase the tunneling current to increase the displacement sensitivity of the STM downmixing method. But from

the effect of the STM downmixing method, we know that some forces increase with the increasing of tunneling current and these forces will impact the displacement measurement sensitivity. This means we cannot increase the displacement sensitivity by indefinitely increasing the tunneling current of the STM downmixing system.

When STM downmixing method is used to detect the displacement of the MEMS device, the results of downmixed tunneling current are better for smaller amplitude. This is because, for the large vibration amplitude of the MEMS device, tip crashes happen during the measurement due to the slow response of STM and fast vibration of the MEMS device. This causes that some information is lost and there are multiple peaks in the results of downmixed tunneling current. So in our measurement, we find that the higher vibrational modes of the MEMS device give us better results, due to smaller vibration amplitude. For modes with large vibration amplitude, we can try to change the measuring position and get better results. For example, in order to measure the first mode, we move the tip to close the edge of the beam and get better results. This is because of two reasons: one is that the vibration amplitude is smaller at the edge of the beam and this avoids the crash; another is that the influence of the forces between the STM tip and the sample on the beam is smaller than other places.

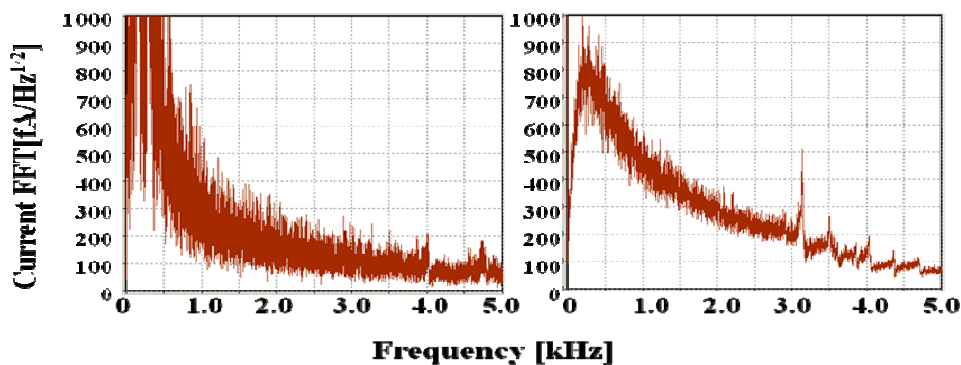


Figure 4.22 The Current noise of STM downmixing method for two different points when the actuating power for piezo disk is zero. Here the spikes of the graph are some mechanical or electrical noise.

4.6. Conclusion

Until now, we have investigated the STM downmixing method and explore some parameters of STM system which impact the measurement of MEMS motion. Also the effect of measuring position along the beam is measured. This will help us to use the STM downmixing method to measure small displacement in the future work. Thus we have demonstrated the use of an electron tunneling transducer with STM downmixing technique to measure the high frequency information of MEMS device and overcome the limit of frequency due to the stray capacitance between the amplifier and tunneling junction.

We demonstrate the results of STM downmixing method which are compared with the COMSOL simulation results and optical interferometry measurement results and investigate the effect of experimental variables on the downmixed tunneling current. With the current conditions, the displacement measurement sensitivity is $17.3\text{fm/Hz}^{1/2}$ which is bigger than the theory prediction, but until now this displacement sensitivity is better than one measured with other methods, such as optical method, the displacement sensitivity based on recent report is higher than $20\text{ fm/Hz}^{1/2}$. Also for the STM downmixing method we still have room to improve the displacement sensitivity. Future work will focus on the improvement of sensitivity and applications in NEMS displacement measurement.

REFERENCE

1. Carr, D. W., Sekaric, L., and Craighead, H.G., Measurement of nanomechanical resonant structures in single-crystal Silicon, *J. Vac. Sci. Technol. B*, 16, 3821, (1998)
2. Kozinsky, I., Postma, H. W. Ch., Bargatin, I., and Roukes, M. L., Tuning nonlinearity, dynamic range, and frequency of nanomechanical resonators, *Appl. Phys. Lett.*, 88, 253101, (2006)
3. Flowers-Jacob, N. E., Schmidt, D. R., and Lehnert, K. W., Intrinsic Noise Properties of Atomic Point contact Displacement Detectors, *Phys. Rev. Lett.*, 98, 096804, (2007)
4. Israelachvili, J. N., Intermolecular and Surface Forces, Academic, London, (1992)
5. Casimir, H. B. G., On the attraction between two perfectly conducting plates, *Proc. K. Ned. Akad. Wet.*, 51, 793 (1948)
6. Chan, H. B., Aksyuk, V. A., Kleiman, R. N., Bishop, D. J. and Capasso, Federico, Quantum mechanical actuation of Microelectromechanical system by the Casimir force, *Science*, 291, 1941, (2001)
7. Buks, E., and Roukes, M. L., Stiction, adhesion energy, and the Casimir effect in micromechanical systems, *Phys. Rev. B*, 63, 033402, (2001)
8. Derjaguin, B. V., Abrikosova, I. I., Lifshitz, Direct measurement of molecular attraction between solids separated by a narrow gap, *Q. Rev. Chem. Soc.*, 10, 295, (1956)
9. Blocki, J., Randrup, J., Swiatecki, W. J., and Tsang, C. F., Proximity forces, *Ann. Phys.*, 105, 427, (1977)

10. Durand, E., *Electrostatique, Tome II Problemes generaux, Conductrues*, p 207, (Masson Paris, 1966)
11. Zalalutdinov, M., Ilic, B., Czaplewski, D., Craighead, H. G., and Parpia, J. M., Frequency-tunable micromechanical oscillator, *Appl. Phys. Lett.*, 77, 3287, (2000)
12. Durig, U., Zuger, O., and Stalder, A., Interaction force detection in scanning probe microscopy: Methods and applications, *J. Appl. Phys.*, 72, 1778, (1992)
13. Simmons, J. H., Generalize Formula for the Electric Tunnel Effect between Similar Electrodes Separated by a Thin Insulating Film, *J. Appl. Phys.*, 34, 238, (1963)
14. Postma, H. W. C., Kozinsky, I., Husain, A., and Roukes, M. L., Dynamic range of nanotube- and nanowire-based electromechanical system, *Appl. Phys. Lett.*, 86, 223105, (2005)
15. Easley, J. G., Nonlinear Vibration of beams and rectangular plates, *J. Appl. Math Phys.*, 15, 167, (1964)
16. Giessibl, F. J., Forces and frequency shifts in atomic-resolution dynamic-force microscopy, *Phys. Rev B*, 56, 16010, (1997)
17. Hofer, W. A., Fisher, A. J., and Wolkow, R. A., and Grutter, P., Surface relaxations, current enhancements, and absolute distances in high resolution scanning tunneling microscopy *Phys. Rev. Lett.*, 87, 236104, (2001).
18. Salapaka, M. V., Bergh, H. S., Lai, J., Majumdar, A., and McFarland, E., Multi-mode noise analysis of cantilevers for scanning probe microscopy, *J. Appl. Phys.* 81, 2480, (1997).

Chapter 5 Future Direction

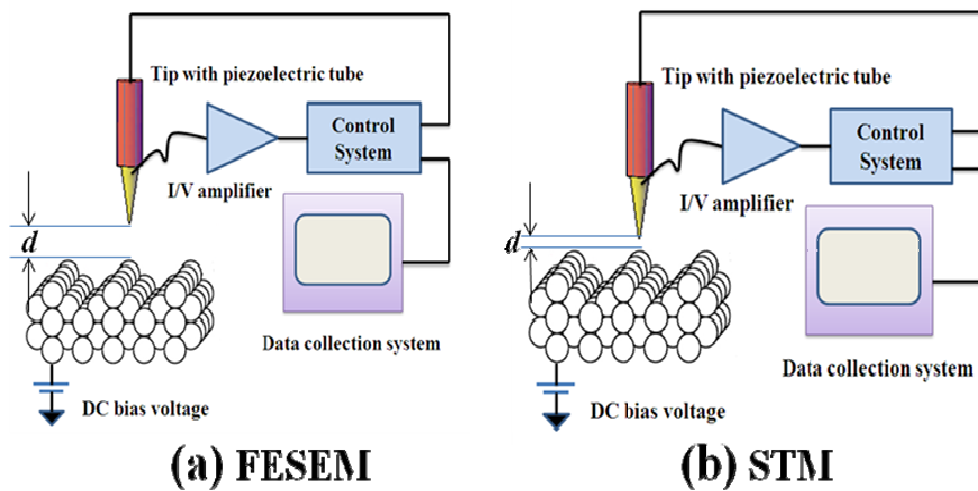
That electron tunneling transduction can be used to measure the high frequency motion of MEMS devices has been demonstrated by STM downmixing readout of nanomechanical motion. But there are some problems which are left for further exploitation. We will present some ideas for future direction in this chapter and hope they will be helpful for the future work.

5.1. How to measure the nanoscale device

MEMS sized devices were chosen in our project due to the difficulty in aligning the tunneling tip on top of individual device structures with the optical telescope. In order to solve this problem and align the tip on the top of nanoscale devices, one of the methods in mind is field emission (FE) scanning electron microscopy. The basic difference between scanning tunneling microscopy (STM) and field emission scanning electron microscopy (FESEM) is the distance between the tip and sample due to the different applied voltages which make them work with different theories. For a FESEM, a FE current between a sharp metallic tip and sample is employed to resolve surface features and an applied voltage much larger than work function of the emitting material was used [1]. With field emission, a bigger gap can be kept between the tip and the sample. Thus we can scan large areas to get the image of the nanoscale device and do not worry that the tip can crash the nanoscale device and cause sample or tip damage based on our now STM system. Figure 5.1 shows our STM system and the FESEM based on our STM system.

In order to make FESEM work, three problem need to be solved. The first one is the control of scanning. The inherent STM system scan range is too small to meet the requirement of FESEM scanning area. Though we have attocubes which can scan $9\mu\text{m}$ by $9\mu\text{m}$ area, the initially purchased controller only provides abrupt stepping motions and is not effective at X-Y scanning due to the difference between the forward scanning step and backward scanning step. New attocube

control boxes have been purchased, which should allow better X-Y scanning, but still need to be implemented. The second problem is the diameter of the STM tip. The diameter will impact the resolution of image topography [2]. For the same topography, the sharper tip, the smaller applied voltage is need for FESEM. Also the sharper tip is better for STM downmixing readout and reduces the electrostatic interaction force and the impact of topography. Both are reasons why developing sharper STM tips is a good way forward for this project application. Otherwise, stability of the field emission current also is a challenge in order to get good image to align the STM tip on the surface of NEMS device.

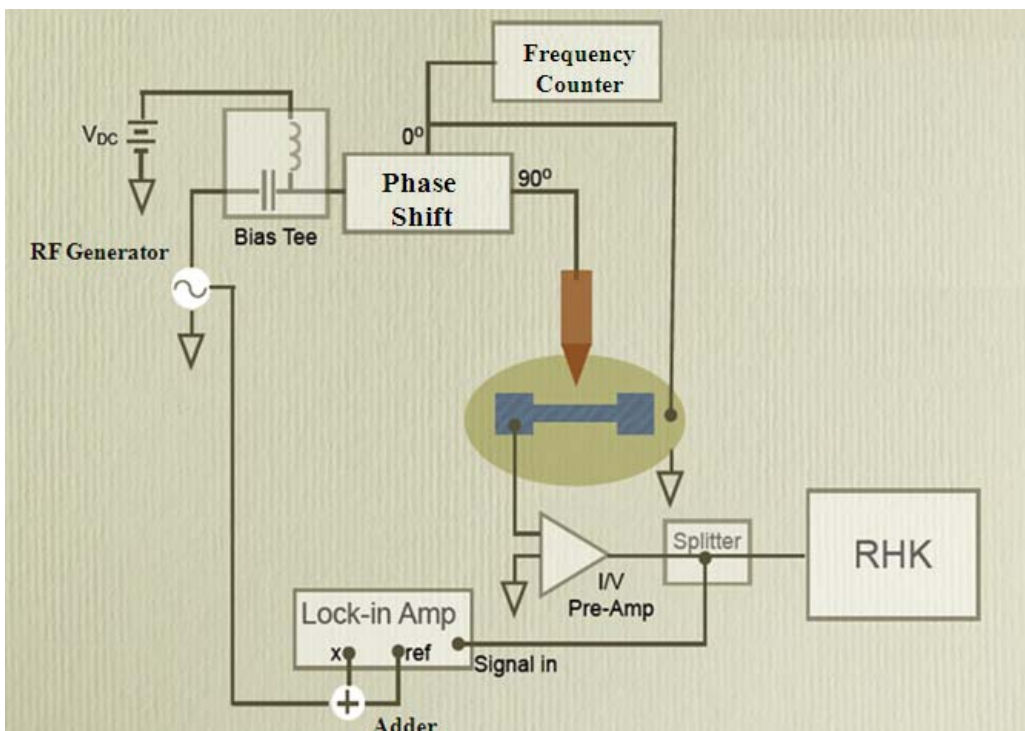


5.1. The Scheme of FESEM and STM. For the FESEM, the distance between the tip and the surface of sample is more than 1 nm and the DC bias voltage is higher than the work function of the sample material. But for the STM system, the distance from the tip to the surface of the sample usually is less than 1 nm (around several angstroms) and the DC bias voltage is lower than the work function of the sample material.

5.2. Phase Locked Loop (PLL) with STM downmixing readout

In the past decade, nanomechanical system (NEMS) resonators have shown their strong potential as high resolution sensors for ultralow mass detection application. The additional mass of an adsorbed species on the top of the NEMS or MEMS

induces a shift in its resonant frequency. To measure this frequency variation, the NEMS is embedded in a phase-locked loop configuration [3]. Since the phase information is retained in STM downmixing, we can integrate our method for PLL configuration and eventual mass sensing or other application. One possible PLL setup is shown in Figure 5.1. Here, the RF generator should have frequency modulation function when it is used in PLL, the phase shift has an ability to split the input signal into two output signals with 90 degree phase difference and the adder can amplify the two input signals and does not cause the phase shift.



5.2. The Scheme of Phase-locked Loop with STM Downmixing Method. Here RF generator is a signal generator with frequency modulation function, phase shift can shift two signals with 90 degree phase difference and adder can amplifier the two input signals and does not cause the phase shift.

This STM downmixing PLL has one problem which is in relation to how the background phase changes relatively quickly in the STM downmixing method. From Figure 4.7, the X output of downmixed tunneling current has two shapes due to the different phase starting point. The reasons that the phase start point

shifts are not known at this time and cannot be controlled for. A variable phase shifter will be needed on the excitation pathway in order to set the phase in a desirable way such that either the X channel or the Y channel provides the null feedback control necessary in a PLL. However, since the background phase quickly changes at different frequencies, as well as for different applied force positions (as in Figure 4.13), setting the phase shifter properly could prove to be different. One solution for this problem may be using the X or Y output of the downmixed tunneling current to replace the R output of the downmixed tunneling current. Some improvements are needed for the current PLL scheme in order to implement the STM downmixing PLL.

5.3. All-electrical-mechanical-on-chip transduction

Currently, serious and detrimental noise sources exist in the instrument which is set up to do STM downmixing readout. These noises include mechanical and electrical noises which come from the ambient of our instrument and impact the sensitivity of the measurement. It is exciting to think about integrating the STM tip, MEMS device, and electrical parts on one chip. This will decrease the noise coming from ambient and decrease the parasitic capacitance due to wiring. It will be helpful for on-chip detection of small motions with applications ranging from accelerometers in ICT to arrayed mass sensors for biosensing in Health and Medical Technologies.

In the literature, a vertical tip and the electrode were fabricated on individual chips which were subsequently bonded together. The electrode was moved by electrostatic actuators to approach it to the tip. This sensor was made by Kenny et al [4] and was applied in an infrared detector [5]. Also a lateral tunneling sensor was developed by Sadewasser et al [6] and integrated into a nanoelectromechanical system. A significant difficulty in the manufacture of all mechanical-electrical-on-chip is the fabrication of a small gap between the sensor and the NEMS, which should be on the order of 1 nm. Current nanotechnological fabrication techniques reach a lower limit of ~ 10 nm. The concept of the present

tunneling sensor is based on an adjustable gap between the sensor and the NEMS. For this purpose the sensor is comprised of a tip which is movable and can be translated with respect to the motion of NEMS.

In future, we are look for a method to fabricate out-of-plane tunneling contact and integrate this tunneling contact to STM downmixing method. This will be a desirable and useful for NEMS applications.

REFERENCE

1. R. D. Young, J. Ward, and F. Scire, The Topografiner: An Instrument for Measuring Surface Microtopography, *Rev. Sci. Instrum.*, 43, 999, (1972)
2. M. A. McCord and R. F. W. Pease, High resolution, low-voltage probes from a field emission source close to the target plane, *J. Vac. Sci. Technol. B* 3, 198 (1985)
3. K. L. Ekinci, Y. T. Yang, and M. L. Roukes, Ultimate limits to inertial mass sensing based upon nanoelectromechanical systems, *J. Appl. Phys.*, 95, 2682, (2004)
4. Kenny, T. W., Waltman, S. B., Reynolds, J. K., and Kaiser, W. J., Micromachined silicon tunneling sensor for motion detection, *Appl. Phys. Lett.*, 58, 100, (1991)
5. Kenny, T. W., Kaiser, W. J., Waltman, S. B., and Reynolds, J. K., Novel infrared detector based on a tunneling displacement transducer, *Appl. Phys. Lett.*, 59, 1820, (1991)
6. Sadewasser, S., Abadal, G., Boisen, A., Dohn, S., et al, Integrated tunneling sensor for nanoelectromechanical system, *Appl. Phys. Lett.*, 89, 173101, (2006)

APPENDIX A: Labview Program Operation

A Labview program is used to control the input signal of the STM downmixing readout circuit and readout the output of the measurement. The control panel includes three parts and is shown in Figure A.1. The first part is the set-up of instruments. Here the instruments which are used in the experiment will be chosen and activated. The second part is used to set up the parameters which control input signal and some values are required to be input, such as sweep frequency range, sweep steps, signal power and the delay between two steps. The input information is decided in this part. The third part is a monitoring part. Some output information about the STM downmixing readout, such as X output of Lock-in amplifier, phase information, the real delay between two measurement data and frequency change are shown with graphs. This is convenient for monitoring the information of STM downmixed tunneling current. Also there is a control button “STOP” which can terminate the program at anytime during the measurement. The detail Labview program is shown in Figure A.2.

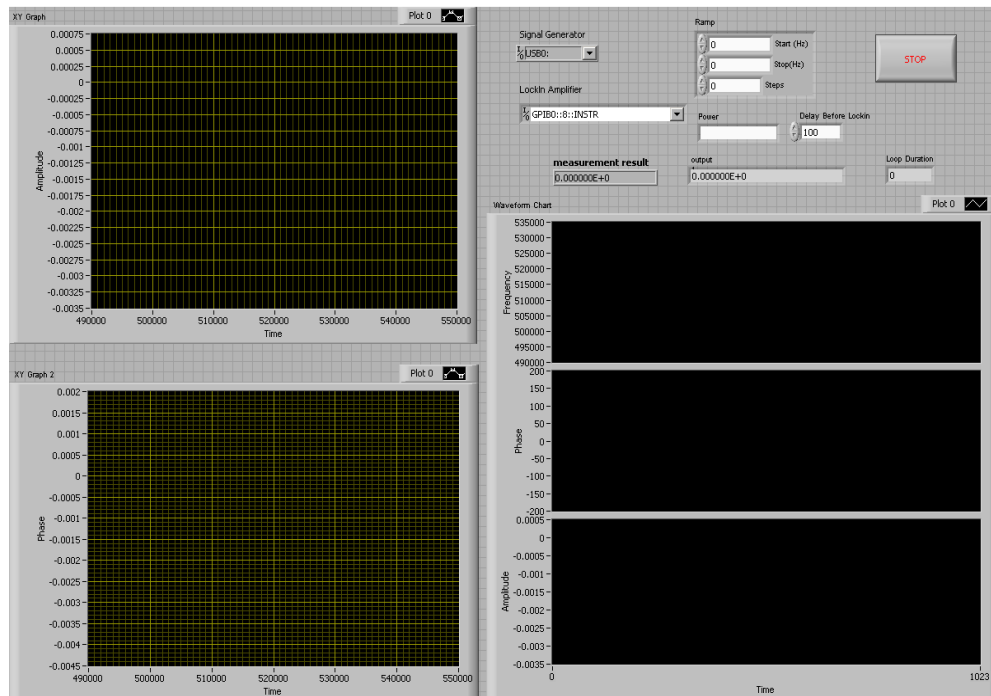


Figure A.1 STM downmixing readout circuit control panel (Thanks to Dave Fortin for the Labview programming)

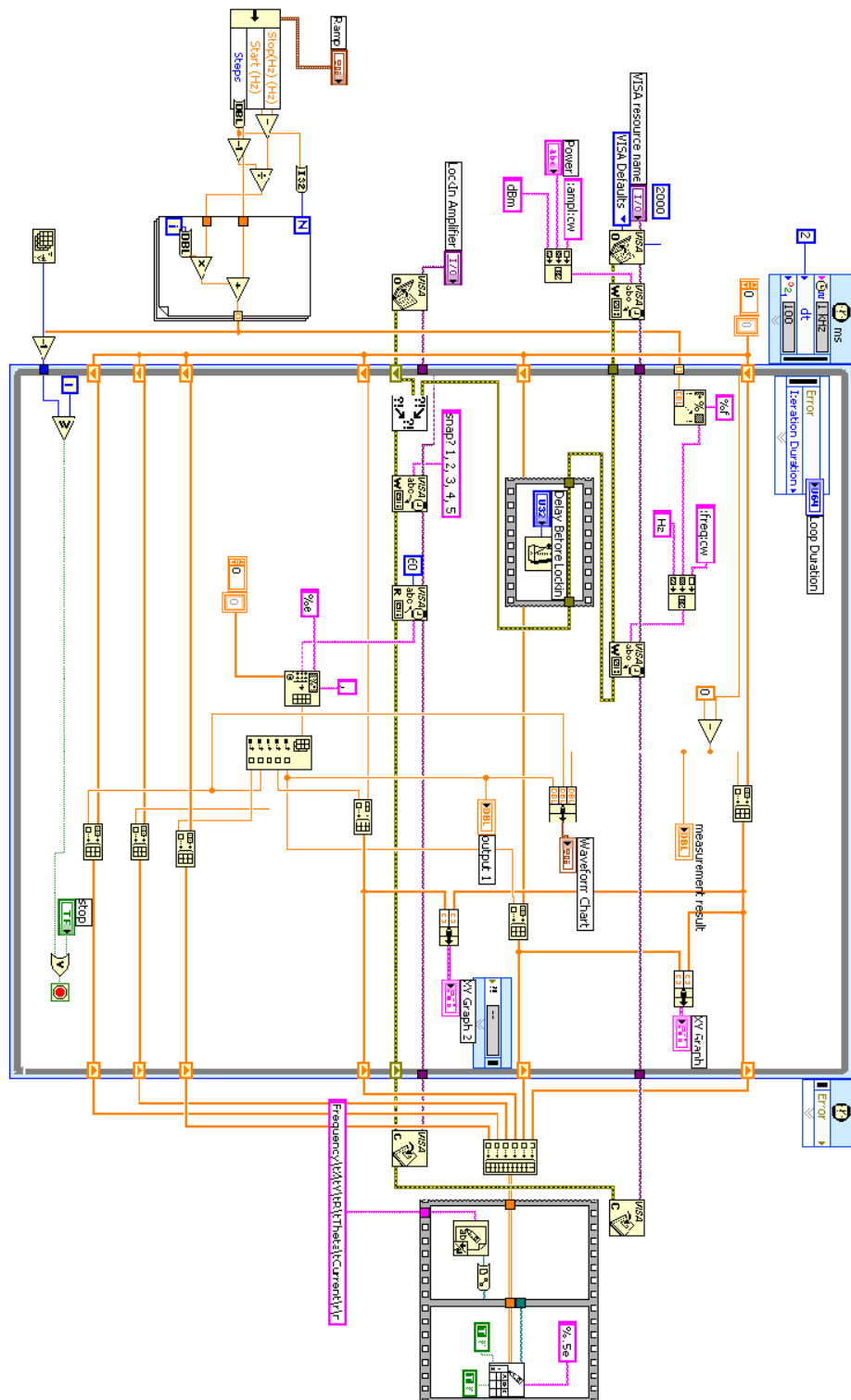


Figure A.2 STM downmixing readout Labview Program, Bloch Diagram (Thanks to Dave Fortin for the Labview programming)

APPENDIX B: STM Downmixing Analysis with Normal Mixer

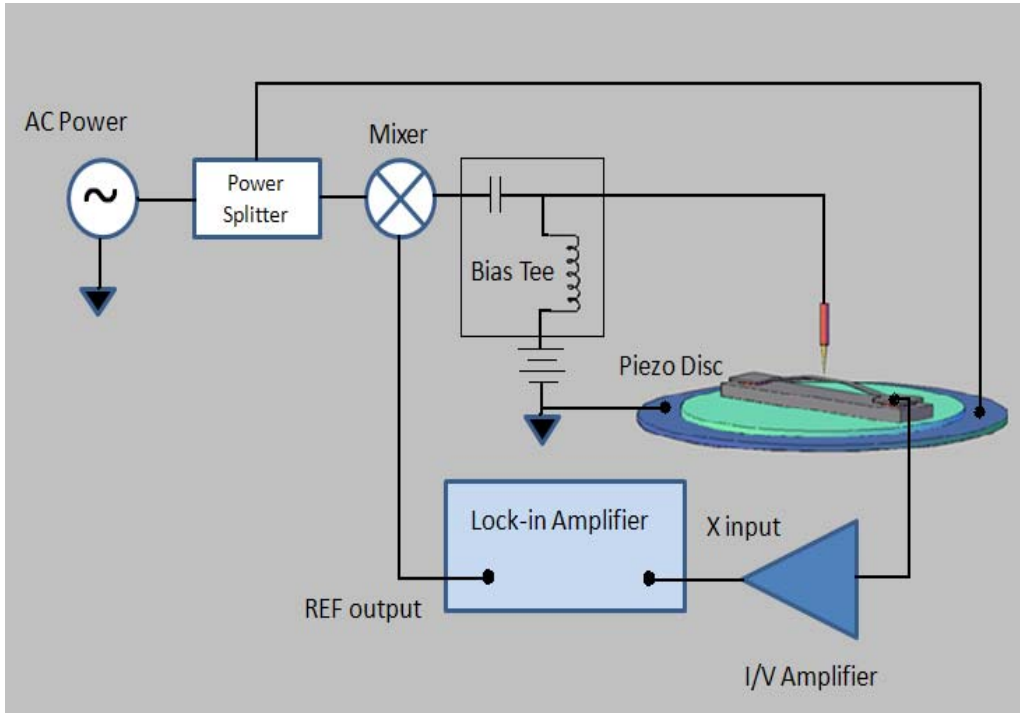


Figure B.1 **Schematic of STM downmixing with normal mixer**

The scheme of STM downmixing with a normal mixer is similar to the scheme of STM downmixing with the single-side band mixer. The main difference of the two circuits is the detectability of the phase information. The phase information can be monitored by the circuit with single-side band mixer, but for the circuit with normal mixer the phase information can't be monitored. That is, the normal mixer circuit is only able to read one quadrature of the mechanically related signal. The reason for this can be explained by the following derivation.

Assume the signal from the signal generator is:

$$V = V_s \sin(\omega_s t) \quad (\text{B.1})$$

The signal from the Lock-in amplifier is:

$$V_{\text{downmixing}} = V_r \sin(\omega_r t) \quad (\text{B.2})$$

If the phase difference is based on the phase of the Lock-in amplifier signal, the phase difference between the generator signal and the lock-in amplifier signal is set θ_1 . Then the output of the mixer can be expressed as:

$$V_{output} = V_s \sin(\omega_s t + \theta_1) * V_r \sin(\omega_r t) \quad (B.3)$$

When the piezo disc actuates the MEMS, the response of MEMS has a response time. The response time cause the phase difference and we can set this phase difference θ_2 . Thus the vibration of MEMS can be written as:

$$d_{MEMS} = a_m \sin(\omega_s t + \theta_1 + \theta_2) \quad (B.4)$$

For STM, when the bias voltage far less than Fermi energy of the metal, the tunneling current can be written as:

$$I \propto (V_{bias} + V(\omega)) e^{-2k(d-d_{MEMS})} \quad (B.5)$$

$$\Rightarrow I \propto (V_{bias} + V_s \sin(\omega_s t + \theta_1) * V_{ref} \sin(\omega_r t)) e^{-2k(d-d_{MEMS})}$$

Use Taylor series and triangle formulas:

$$e^x = 1 + x + \frac{1}{2!} x^2 + \frac{1}{3!} x^3 + \dots$$

$$\sin \alpha \cos \beta = \frac{1}{2} [\sin(\alpha + \beta) + \sin(\alpha - \beta)]$$

$$\sin \alpha \sin \beta = -\frac{1}{2} [\cos(\alpha + \beta) - \cos(\alpha - \beta)]$$

The tunneling current can be rewritten as:

$$I \propto (V_{bias} - \frac{1}{2} V_s V_R \{ \cos[(\omega_s + \omega_r)t + \theta_1] - \cos[(\omega_s - \omega_r)t + \theta_1] \}) e^{-2kd} [1 + 2ka_m \sin(\omega_s t + \theta_1 + \theta_2) + \dots] \quad (B.6)$$

The high frequency parts in equation (A.6) will be blocked due to the limit of bandwidth in STM. When we omit high frequencies items and just keep reference frequency items, we can get:

$$I \propto V_{bias} e^{-2kd} - \frac{1}{2} V_s V_r e^{-2kd} k a_m [\sin(\omega_r t - \theta_2) + \sin(\omega_r t + \theta_2)] \quad (\text{B.7})$$

Finally, using triangle identity $\sin \alpha + \sin \beta = 2 \sin \frac{\alpha + \beta}{2} \cos \frac{\alpha - \beta}{2}$,

the downmixed current is:

$$I \propto V_s V_r e^{-2\kappa d} k a_m \sin(\omega_r t) * \cos(\theta_2) \quad (\text{B.8})$$

The lock-in amplifier picks the ω_r signal. However, when θ_2 is 90 degree, the signal is lost completely (that is, essentially only information about the X quadrature is available using a normal mixer).

APPENDIX C: The Beam Higher Mode Information

In Section 4.3, we use STM downmixing method to measure the first six modes of the MEMS beam. Here we display the measured results for higher mode of the MEMS beam with STM downmixing methods. Due to the complex of STM downmixing method, we cannot pinot out the detail modes which these results belong to. Here we just show these results in Figure C.1. These results are measured at the center point of the beam and at the measuring condition: DC tunneling current is 0.25nA, DC bias voltage is 0.5 V, AC bias voltage is 0.1 V_{rms}, and the actuating power is -11dBm. With these initial conditions, we can measure the resonance frequencies lower than 5 MHz vibration mode. For the higher frequency information, we do not get the better results due to the limit of the sensitivity of our measurement system for this measuring condition. In Figure C.1 (e) and (h), we can show the situation that the two resonance frequencies are close each other and this causes the superposition of the vibration amplitude and phase shift.

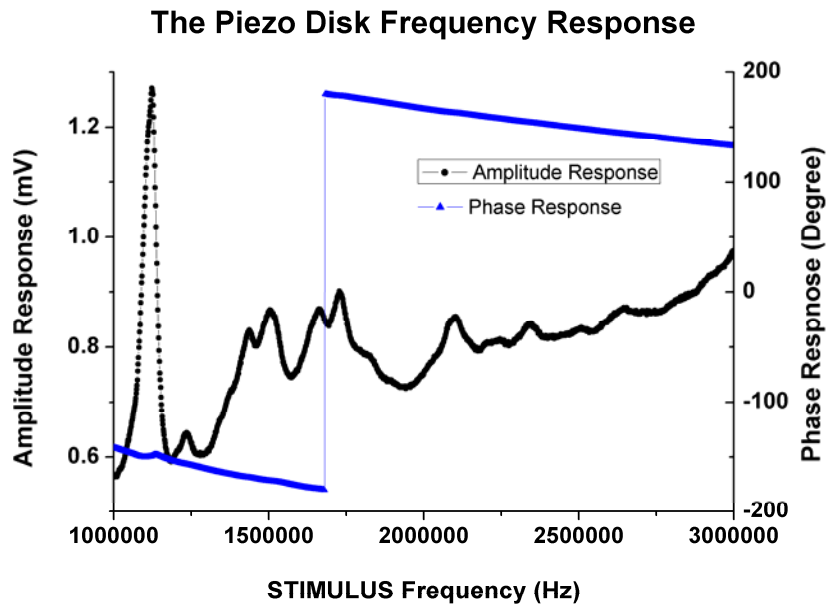
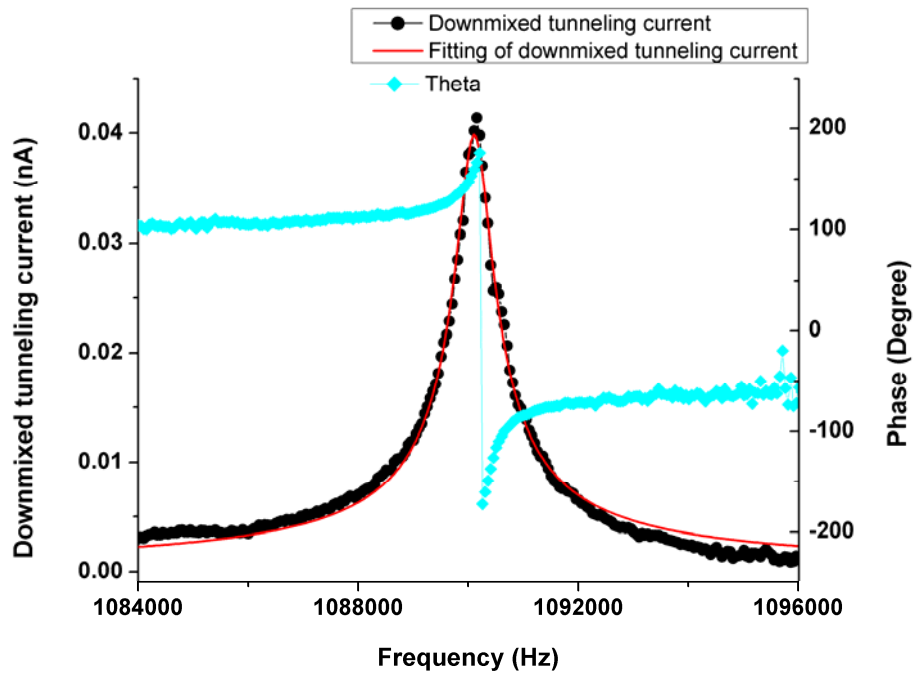
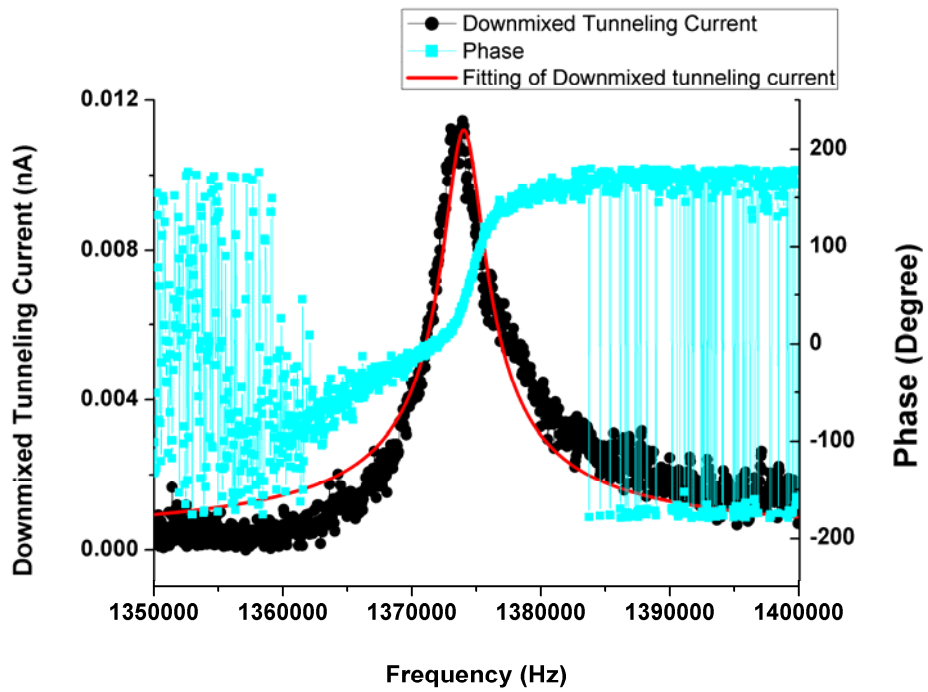


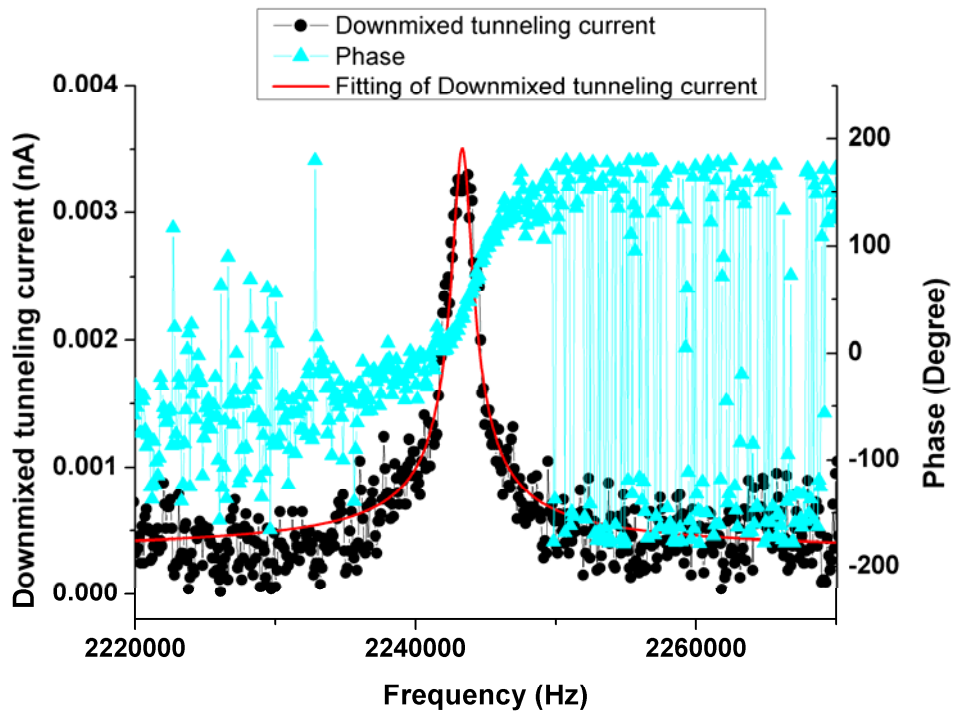
Figure C.1. The piezo disk frequency response with MEMS device on the top



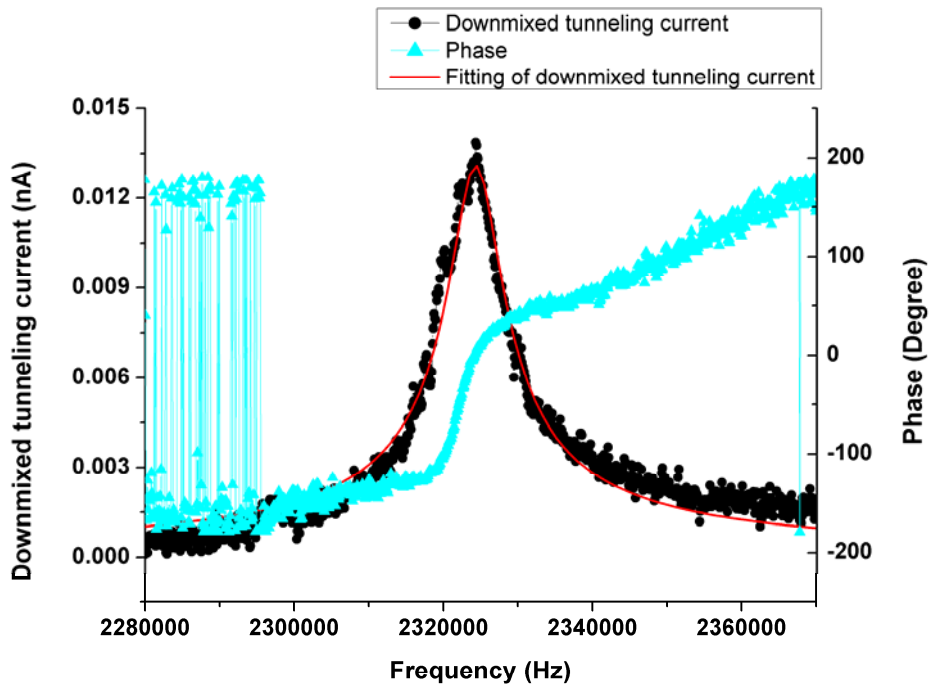
(a)



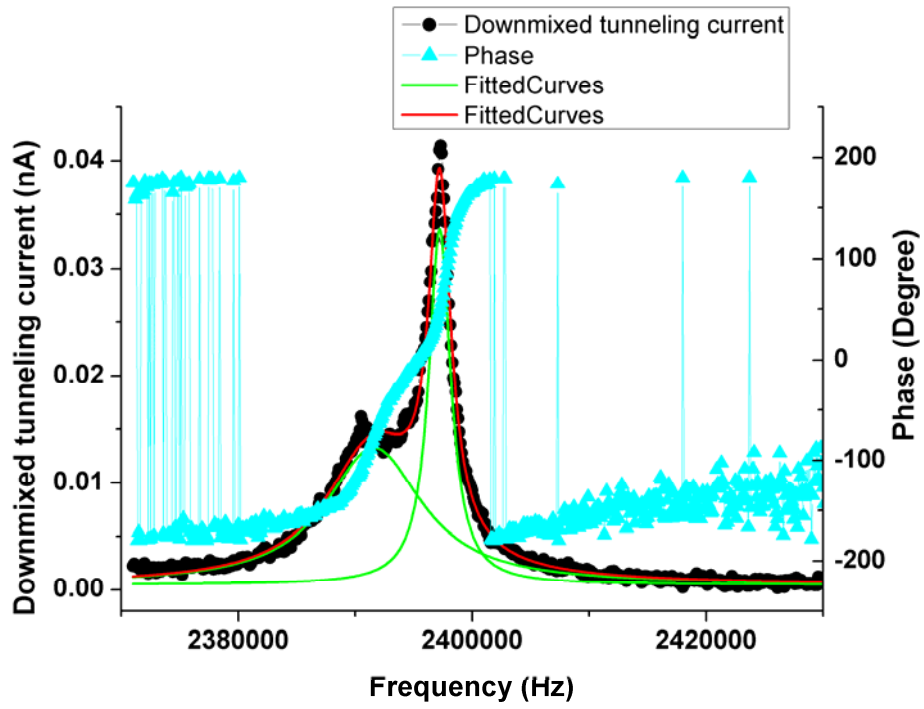
(b)



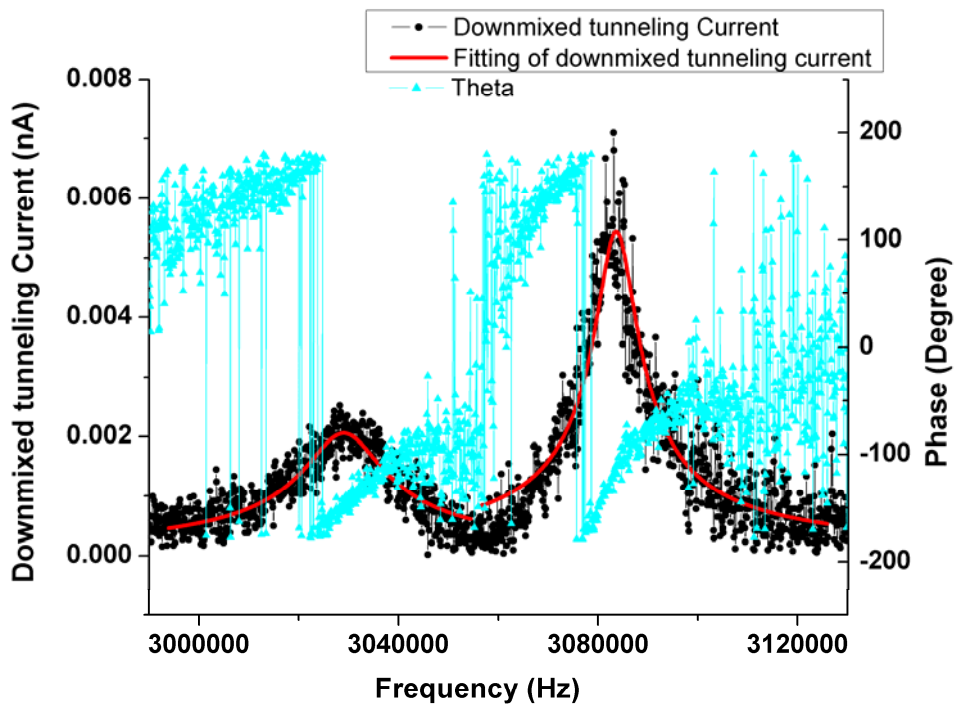
(c)



(d)



(e)



(f)

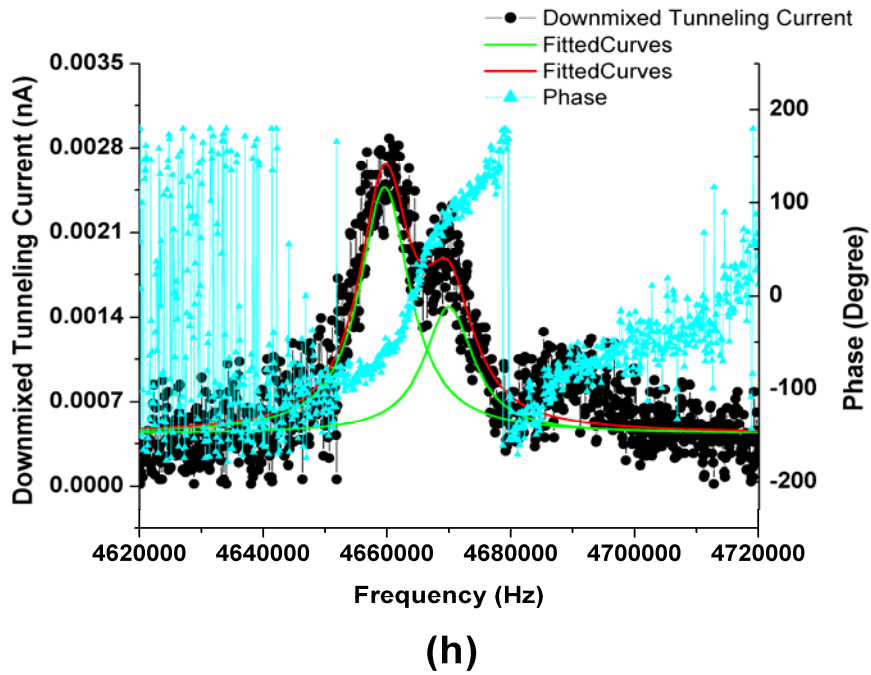
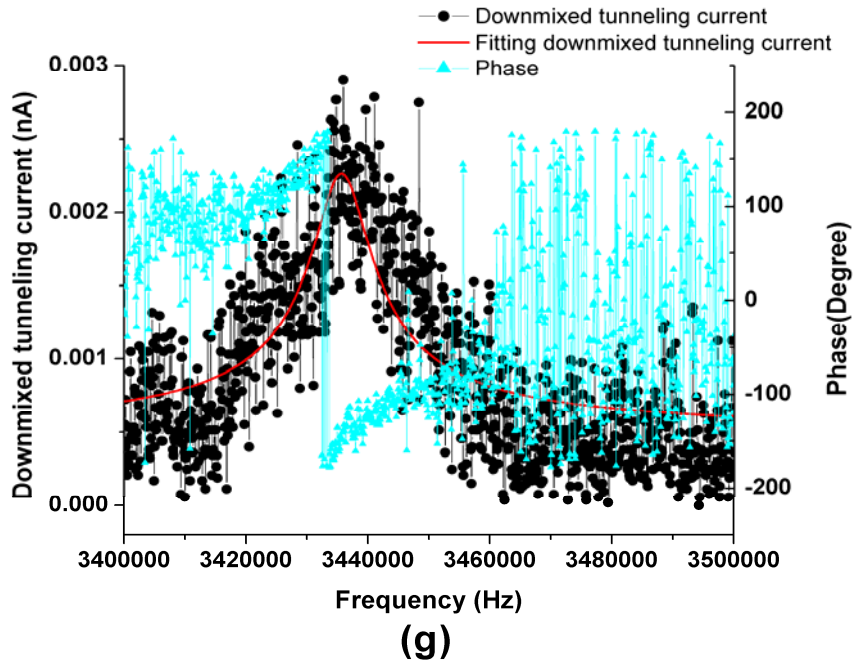


Figure C.2. The resonance frequencies and phase information for higher mode of a long 500 μm , wide 100 μm and thick 5 μm silicon doubly-clamped beam with Au and Cr metal layer at DC tunneling current 0.2 nA, DC bias voltage 0.5 V, AC bias voltage 0.1 V_{rms} and the piezo disk actuating power -11 dBm

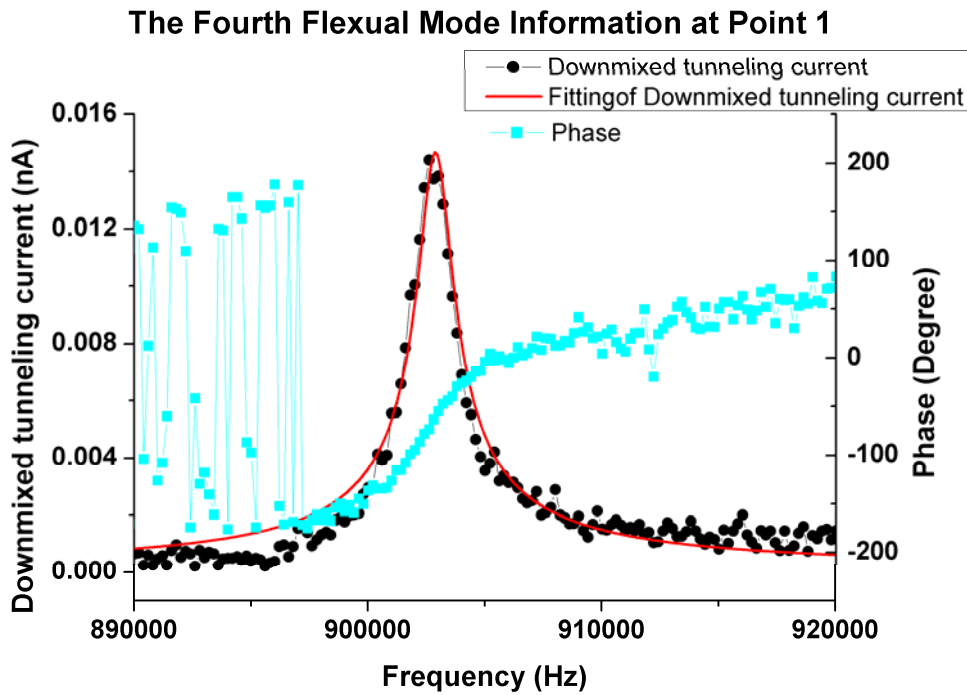
Table C.1 The higher vibration mode information for a long 500 μm , wide 100 μm and thick 5 μm Silicon Doubly-clamped Beam with Au and Cr Metal Layers

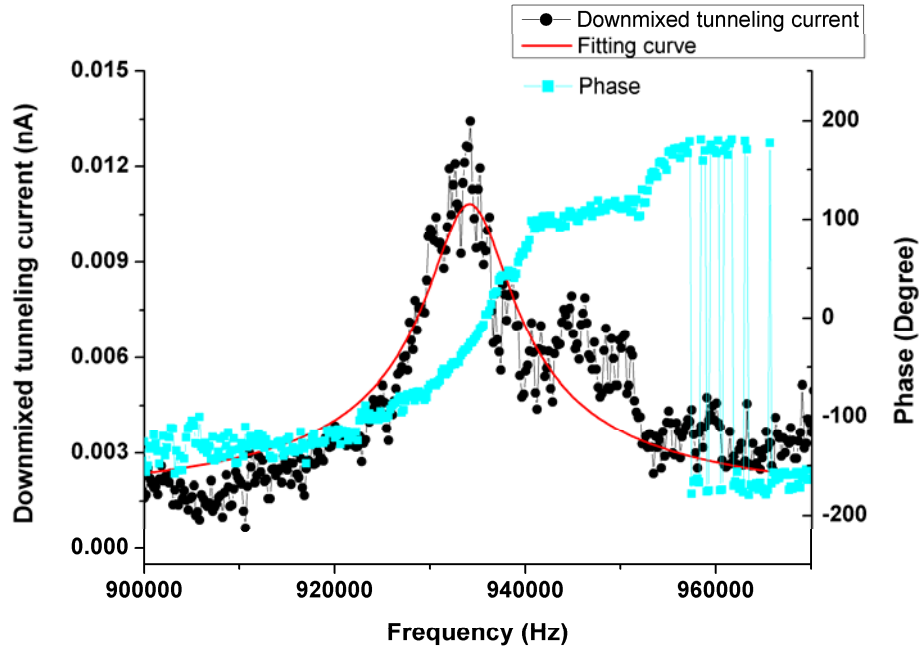
Figure Results	a	b	c	d	e	f	g	h
Resonance Frequency (MHz)	1.09	1.37356	2.24329	2.32427	2.3916 2.39722	3.02897 3.08352	3.4356	4.65954 4.6699
Q-factor	1607	386	795	334	237 1052	291 380	363	472 479
Downmixed tunneling current (nA)	0.040	0.012	0.0032	0.013	0.016 0.042	0.00206 0.00543	0.0023	0.0026 0.0013

These results further prove the work of the STM downmixing method. With this technique we can measure the vibration information about 5 MHz at current measuring condition which is well over the RC-bandwidth limitation of the STM system. We also can increase the displacement measurement sensitivity of our system by simply increasing DC tunneling current and decreasing the DC bias voltage which are discussed in Chapter 4.

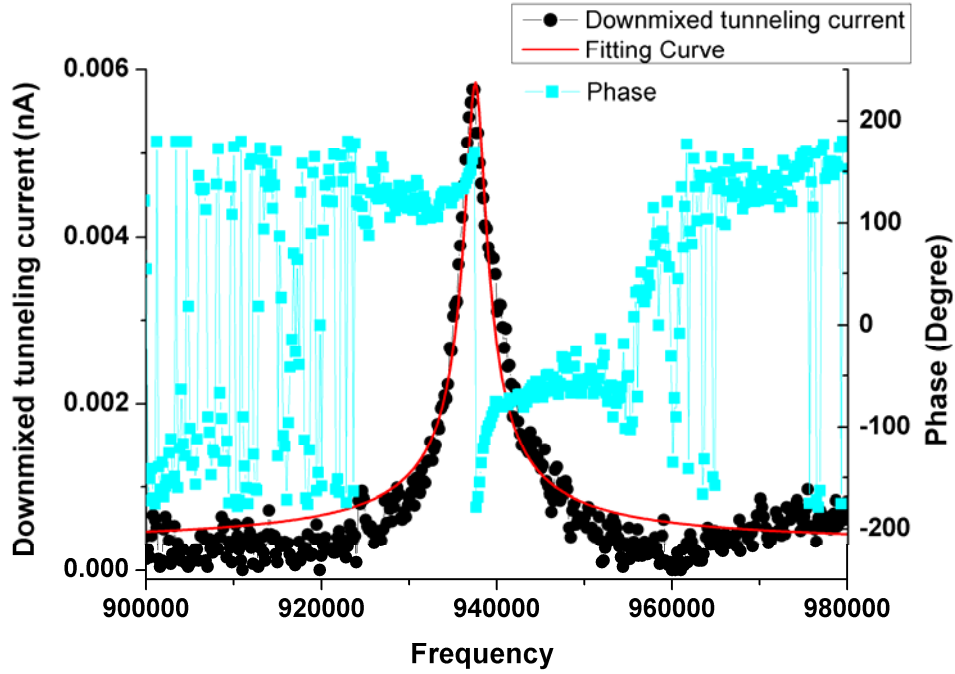
APPENDIX D: Detail Information about the Different Point

When we use the STM downmixing method to measure the resonance frequencies for higher vibration mode of the MEMS device, a confused thing is that the resonance frequencies of the MEMS beam sometimes change with the different measuring points on the beam. There are two different results changing measuring points: one is that the resonance frequencies have a big change with the measuring points which is more than 10 percents; another one is that the resonance frequencies have a small change with the different measuring point. This is discussed in Chapter 4. Here we display the detail information for each point of Figure 4.16 in Figure D.1, in order to see the STM downmixing method and the impact of changing measuring points. The information includes the detail resonance frequencies and phase information of each point in Figure 4.16.

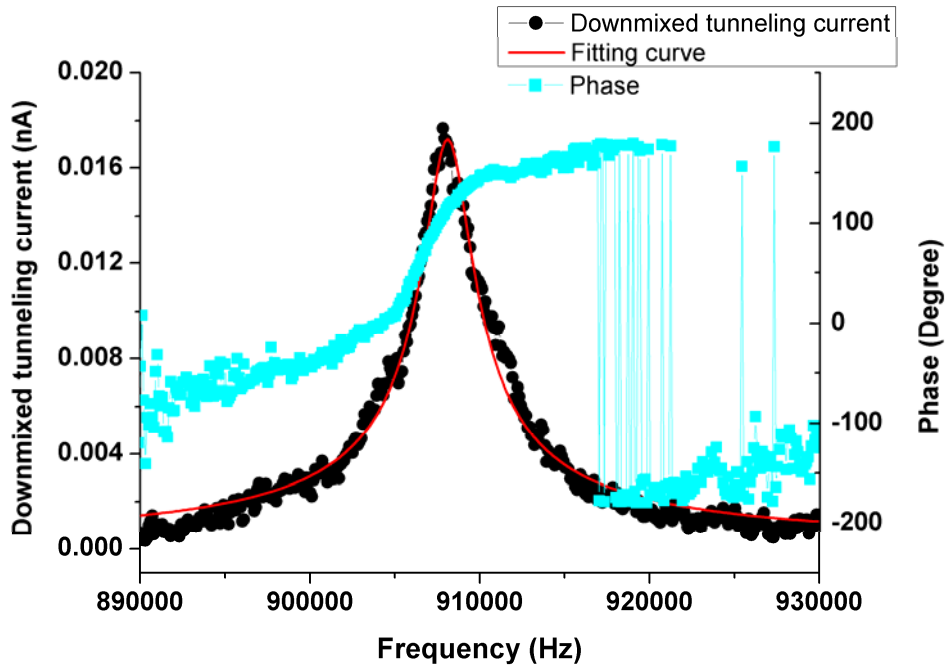


The Fourth Flexural Mode Information at Point 2

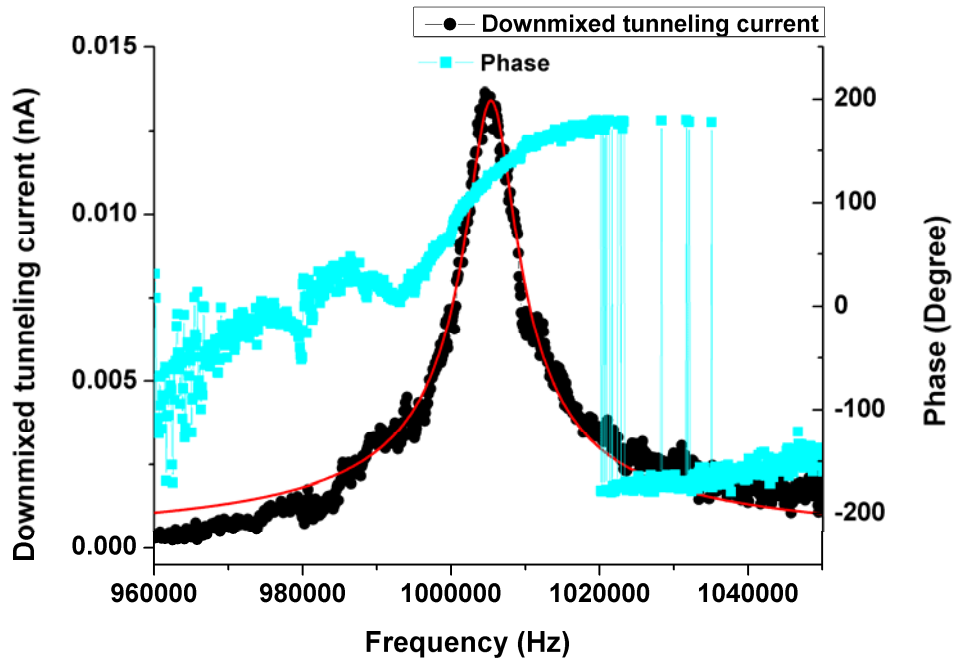
(b)

The Fourth Flexural Mode Information at Point 3

(c)

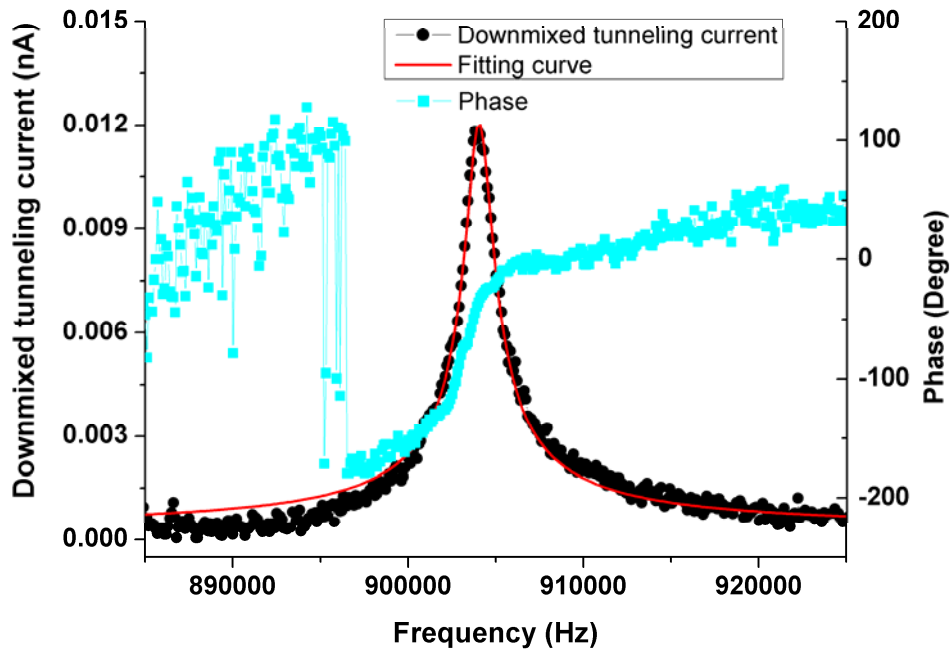
The Fourth Flexural Mode Information at Point 4

(d)

The Fourth Flexural Mode Information at Point 5

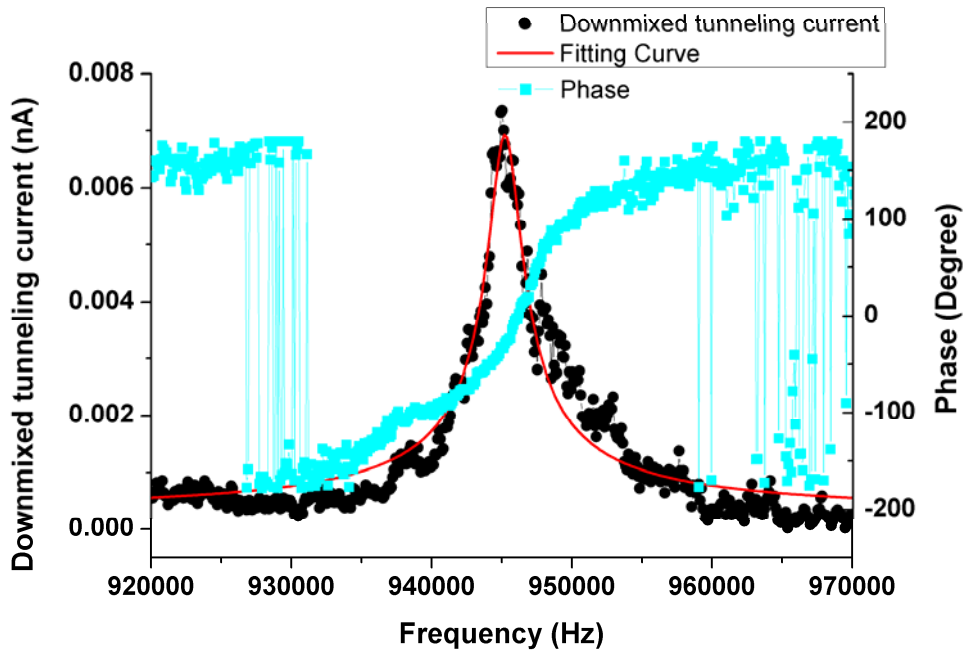
(e)

The Fourth Flexural Mode Information at Point 6



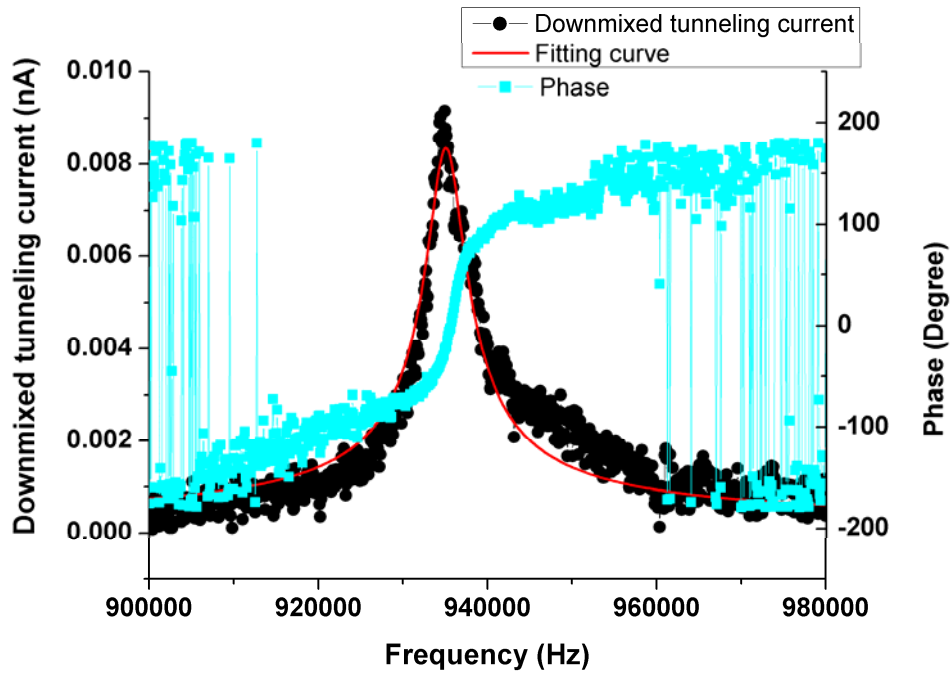
(f)

The Fourth Flexural Mode Information at Point 7



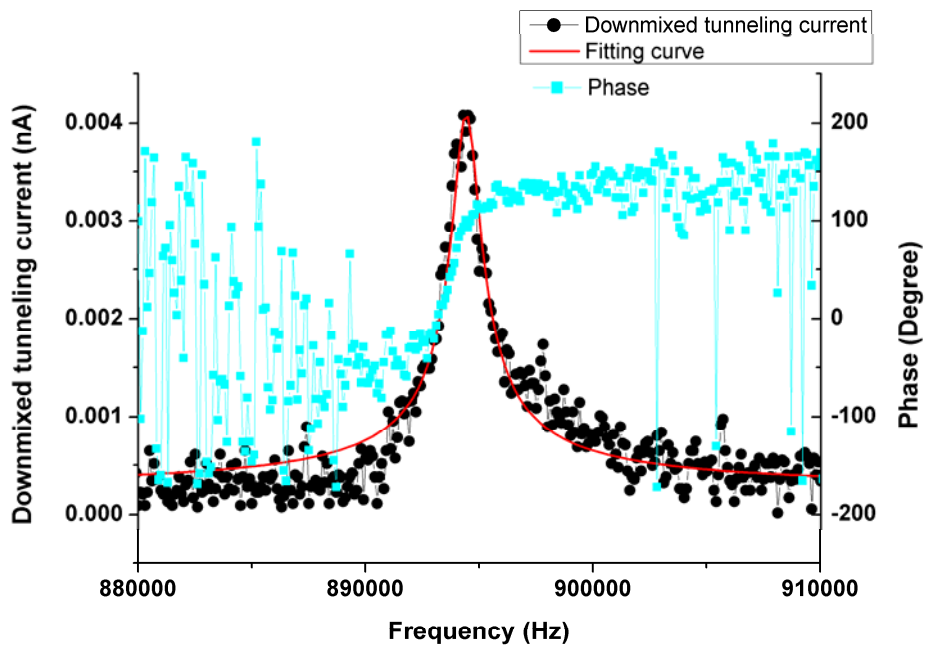
(g)

The Fourth Flexural Mode Information at Point 8

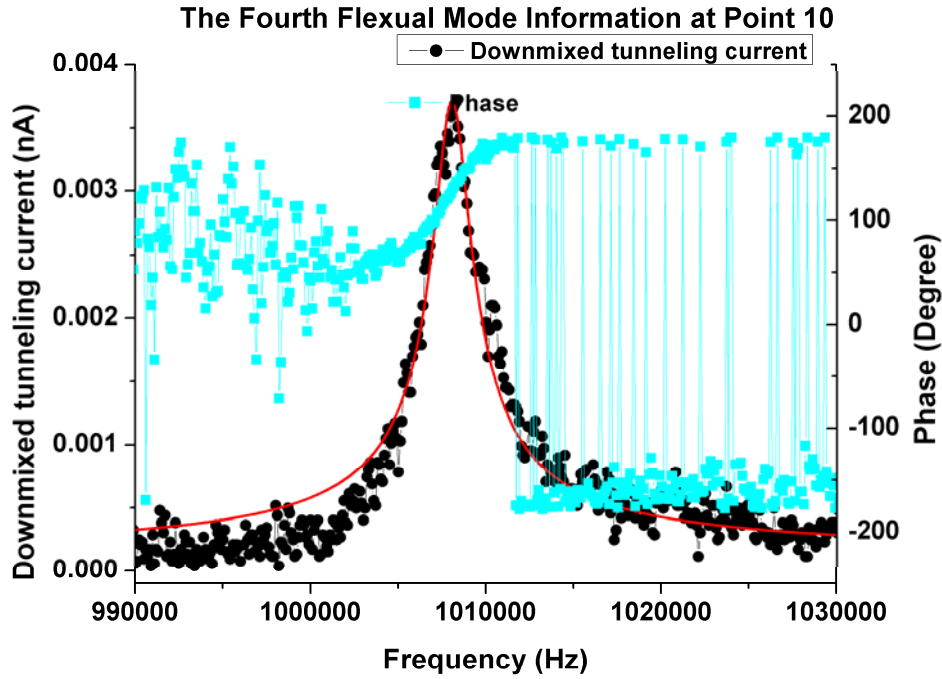


(h)

The Fourth Flexural Mode Information at Point 9



(i)



(j)

Figure D.1. The detail resonance frequency and phase shift information for different measuring position along length at DC tunneling current 0.2 nA, DC bias voltage 0.5 V, AC bias voltage 0.1 V_{rms} and piezo disk actuating power -11 dBm

Table D.1 The resonance frequencies and phase information for the different position along the length of a long 500 μm , wide 100 μm and thick 5 μm Silicon Doubly-clamped Beam with Au and Cr Metal Layers

Point Parameter	1	2	3	4	5	6	7	8	9	10
Resonance Frequency (KHz)	902.87	934.461	937.477	908.13	1052.30	904.157	945.363	935.562	894.445	1008.26
Error (Hz)	60	257	86	29	53	36	60	46	88	70

APPENDIX E: MEASUREMENT OF BARRIER HEIGHT

Barrier height (or work function) of the material is a important parameter for the STM tunneling current. In the thesis, we use this theory value from textbook (Introduction to Scanning Tunneling Microscopy, C. Julian Chen) and this value is for clean surface. For the real value, we can measure following below instructions..

From the basic tunneling theory, the current is an exponential function with the distance between the tip and the sample surface.

$$I \propto e^{-2\kappa d} \quad (\text{E.1})$$

where κ is constant that includes the barrier height and d is the tunneling distance. If we know the electrical charge density displacement either Z piezo of STM or piezo disk with sample, we can modulate the distance by a small amount δd using a sinusoidal function. Then the distance between the tip and the sample surface will have the form:

$$d = d_0 + \delta d \cos(\omega t) \quad (\text{E.2})$$

then the tunneling current can be written as:

$$I \propto e^{-2\kappa d_0} e^{-2\kappa \delta d \cos(\omega t)} \quad (\text{E.3})$$

If the modulation frequency is well above the bandwidth of the feedback loop, the first part of the expression is simply the normal feedback tunneling current I_0 . If the modulation amplitude is small, we can use Taylor's series to rewrite the tunneling current as:

$$I \propto I_0 (1 - 2\kappa \delta d \cos(\omega t)) \quad (\text{E.4})$$

Then we use lock-in amplifier to readout the information of modulation part. Due to the rms readout of lock-in amplifier, the output signal will related to the modulated current detected by the lock-in amplifier,

$$-I_0 * 2\kappa\delta d \frac{1}{\sqrt{2}} \quad (\text{E.5})$$

Solve for κ and get the expression:

$$\kappa = \frac{-I_{lockin}}{I_0 * \delta d / \sqrt{2}} \quad (\text{E.6})$$

From a quantum mechanical derivation of tunneling, κ is related to the electron and the barrier height Φ and can be expressed as:

$$2\kappa = 1.025\sqrt{\Phi} \quad (\text{E.7})$$

Thus we substitute Equation (E.6) into the above expression and the barrier height can be gotten as:

$$\Phi = \left(\frac{I_{lockin} \sqrt{2}}{1.025 I_0 \delta d} \right)^2 \quad (\text{E.8})$$

With the RHK system, we can easily implement this measurement when we know the displacement of either Z piezo of STM or driving piezo disk.